

AD-A089 743

AERODYNE RESEARCH INC BEDFORD MA CENTER FOR CHEMICAL--ETC F/G 7/4  
QUANTITATIVE INFRARED SPECTROSCOPIC MEASUREMENTS OF BORON FLUOR--ETC(U)  
AUG 80 M E GERSH, C E KOLB, M S ZAHNISR F49620-77-C-0075

UNCLASSIFIED

ARI-RR-225

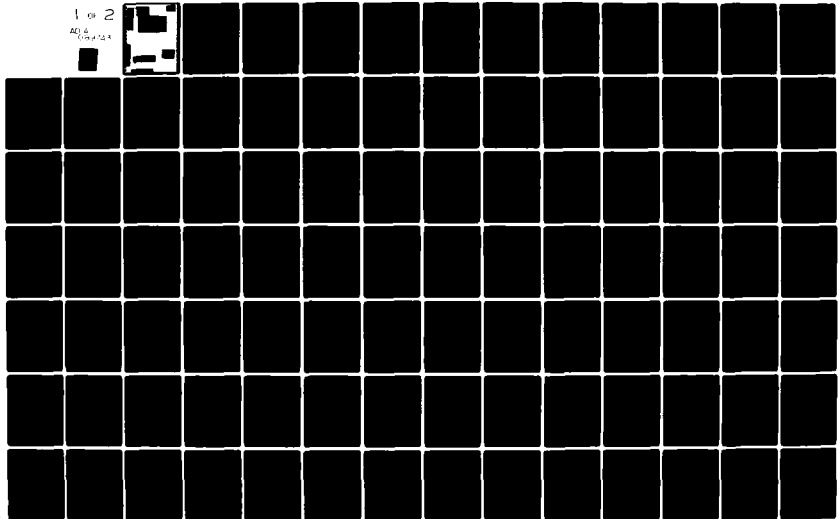
AFOSR-TR-80-0942

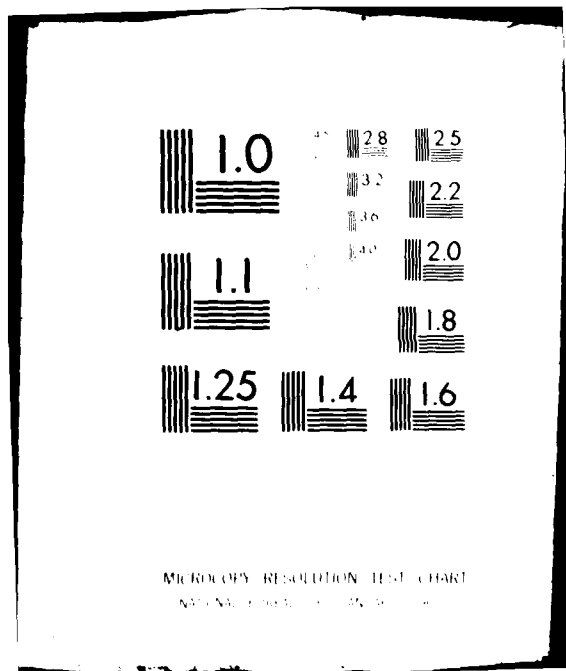
NL

1 of 2

20.6

10.4

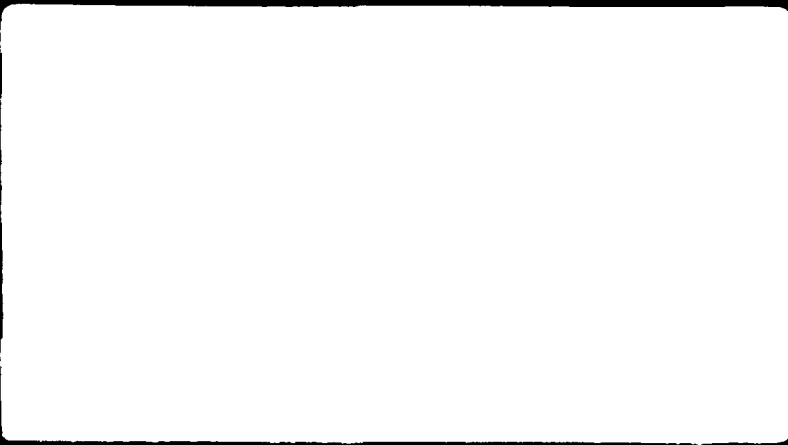




MICROCOPY RESOLUTION TEST CHART  
NATIONAL BUREAU OF STANDARDS-1963-A

12

LEVEL



AD A089743

DDC FILE COPY

Without the permission of the copyright owner, no part of this publication may be reproduced, stored in a retrieval system, or transmitted in any form or by any means, electronic, mechanical, photocopying, recording, or by any information storage and retrieval system, without the prior written permission of the copyright owner.

COLLECTED

80 9 25 062

UNCLASSIFIED

SECURITY CLASSIFICATION OF THIS PAGE (When Data Entered)

REPORT DOCUMENTATION PAGE		READ INSTRUCTIONS BEFORE COMPLETING FORM
1. REPORT NUMBER <b>AFOSR-TR-80-0942</b>	2. GOVT ACCESSION NO. <b>AD-A089743</b>	3. RECIPIENT'S CATALOG NUMBER
4. TITLE (and Subtitle) Quantitative Infrared Spectroscopic Measurements of Boron Fluorides		5. TYPE OF REPORT & PERIOD COVERED Final Report 4/1/77-3/30/80
		6. PERFORMING ORG. REPORT NUMBER ARI-RR-225
7. AUTHOR(s) M.E. Gersh, C.E. Kolb, M.S. Zahniser, L.S. Bernstein, J.A. Silver, R.G. Brown, C.M. Gozewski, S. Kallelis, J.C. Wormhoudt, L.M. Peterson*		8. CONTRACT OR GRANT NUMBER(s) F49620-77-C-0075 ✓
9. PERFORMING ORGANIZATION NAME AND ADDRESS Aerodyne Research, Inc. Crosby Drive, Bedford, MA 01730		10. PROGRAM ELEMENT, PROJECT, TASK AREA & WORK UNIT NUMBERS 61102F 2303/B1
11. CONTROLLING OFFICE NAME AND ADDRESS Air Force Office of Scientific Research /NC Bolling AFB, DC 20332		12. REPORT DATE August 1980
		13. NUMBER OF PAGES 143
14. MONITORING AGENCY NAME & ADDRESS (if different from Controlling Office)		15. SECURITY CLASS. (of this report) UNCLASSIFIED
		15a. DECLASSIFICATION/DOWNGRADING SCHEDULE
16. DISTRIBUTION STATEMENT (of this Report)  Approved for public release; distribution unlimited.		
17. DISTRIBUTION STATEMENT (of the abstract entered in Block 20, if different from Report)		
18. SUPPLEMENTARY NOTES		
19. KEY WORDS (Continue on reverse side if necessary and identify by block number) Boron Fluoride                      Band Model Boron Trifluoride                  Flow Reactor Infrared Spectroscopy              High Temperature		
20. ABSTRACT (Continue on reverse side if necessary and identify by block number) The objective of this research is the performance of quantitative infrared spectroscopic measurements of boron fluorides and oxides in the gas phase. The measurement program is designed to determine infrared absorption coefficients and absorption line spacings in order to facilitate the construction of infrared radiation band models.  In order to carry out these measurements an apparatus which permits the performance of quantitative spectroscopic measurements of transient species		

DD FORM 1473  
1 JAN 73EDITION OF 1 NOV 65 IS OBSOLETE  
S/N 0102-LF-014-6601

UNCLASSIFIED

SECURITY CLASSIFICATION OF THIS PAGE (When Data Entered)

UNCLASSIFIED

SECURITY CLASSIFICATION OF THIS PAGE(When Data Entered)

over the temperature range of 300 to 1500 K was constructed. The capability of this apparatus to perform these measurements over its designed range of operating parameters was demonstrated.

The infrared absorption coefficients of the  $\nu_3$  band of  $\text{BF}_3$  were measured over the range of 300 to 1500 K. These measurements were combined with flame measurements at 2400 K to develop and verify a radiation band model for  $\text{BF}_3$ . The formalism developed for this band model is more comprehensive than previous treatments and is generally applicable to perpendicular bands of symmetric top molecules.

The infrared band strength of BF was measured. The band strength was determined by measuring the absorption cross section of a single vibration-rotation line using a tunable diode laser as the light source. The BF number density was measured in-situ using ultraviolet absorption spectroscopy.

UNCLASSIFIED

SECURITY CLASSIFICATION OF THIS PAGE(When Data Entered)

18 AFOSR-TR-80-0942

3 SEP 1980

12

14 ARI-RR-225

AFOSR-TR-80-0942

QUANTITATIVE INFRARED SPECTROSCOPIC MEASUREMENTS OF BORON FLUORIDES

9/11/80, 1 April - 30 Mar 84

DTIC ELECT SEP 30 1980

by

10

Michael E. Gersh, Charles E. Kolb, Mark S. Zahniser, Lawrence S. Bernstein, Joel A. Silver, Robert G. Brown, Conrad M. Gozewski, Spiros Kallelis, Joda C. Wormhoudt and Lauren M. Peterson\*

Center for Chemical and Environmental Physics, Aerodyne Research, Inc., Bedford, MA 01730

Prepared for

Air Force Office of Scientific Research (AFSC), Directorate of Chemical Sciences, Bolling Air Force Base, DC 20332

Prepared under

Contract No. F49620-77-C-0075

11 August 1980

\*Environmental Research Institute of Michigan, Ann Arbor, MI 48107

Approved for public release; distribution unlimited.

41

## TABLE OF CONTENTS

<u>SECTION</u>	<u>PAGE</u>
ABSTRACT .....	ix
1. INTRODUCTION .....	1-1
2. A VERSATILE HIGH TEMPERATURE FLOW REACTOR FOR KINETIC AND SPECTROSCOPIC STUDIES .....	2-1
INTRODUCTION .....	2-2
I. DESCRIPTION OF THE APPARATUS .....	2-4
A. General .....	2-4
B. Vacuum Jacket and Flow Reactor .....	2-5
B.1 Overall Description .....	2-5
B.2 Flow Simulation Experiment .....	2-8
B.3 Flow Tube Diagnostics .....	2-12
C. Measurement Capabilities .....	2-17
C.1 Mass Spectrometer .....	2-17
C.2 Infrared Absorption .....	2-18
C.3 Laser-Induced Fluorescence .....	2-21
C.4 Resonance Fluorescence .....	2-22
C.5 Ultraviolet Absorption .....	2-23
C.6 Chemiluminescence .....	2-24
II. OPERATION .....	2-25
ACKNOWLEDGEMENTS .....	2-27
REFERENCES .....	2-28
FIGURE CAPTIONS .....	2-30
3. MEASURED AND PREDICTED BAND MODEL PARAMETERS OF $\text{BF}_3(\nu_3)$ AT HIGH TEMPERATURES .....	3-1
I. INTRODUCTION .....	3-2

## TABLE OF CONTENTS (CONT.)

<u>SECTION</u>	<u>PAGE</u>
II. GLOSSARY OF NOTATION .....	3-4
III. EXPERIMENTAL .....	3-9
A. High Temperature Flow Reactor .....	3-9
B. Flame Emission-Absorption Apparatus .....	3-15
IV. THEORETICAL PREDICTIONS OF BAND MODEL PARAMETERS .....	3-21
A. Average Line Spacing .....	3-21
B. Average Integrated Line Strength .....	3-26
C. Average Spectral Absorption Coefficient And Line Density .....	3-27
D. Effects of Nuclear Spin Statistics on Calculated Band Model Parameters .....	3-29
E. Computational Considerations .....	3-31
V. RESULTS AND DISCUSSION .....	3-36
ACKNOWLEDGEMENTS .....	3-42
REFERENCES .....	3-43
FIGURE CAPTIONS .....	3-46
4. MEASUREMENT OF THE VIBRATIONAL BAND STRENGTH OF <sup>11</sup> BF USING A TUNABLE DIODE LASER .....	4-1
I. INTRODUCTION .....	4-2
II. EXPERIMENTAL .....	4-3
A. UV Absorption Measurements .....	4-4
B. IR Absorption Measurements .....	4-8
C. Optical Path Length Determinations .....	4-10

**AIR FORCE OFFICE OF SCIENTIFIC RESEARCH (AFSC)**  
**NOTICE OF TRANSMITTAL TO DBC**  
 This technical report has been reviewed and is  
 approved for public release IAW AFR 190-18 (7b).  
 Distribution is unlimited.  
**A. D. BLOSE**  
 Technical Information Officer

# TABLE OF CONTENTS (CONT.)

<u>SECTION</u>	<u>PAGE</u>
III. RESULTS AND DISCUSSION .....	4-13
ACKNOWLEDGEMENTS .....	4-20
REFERENCES .....	4-21
FIGURE CAPTIONS .....	4-24
5. PUBLICATIONS AND PRESENTATIONS .....	5-1

Accession For	
NTIS	<input checked="" type="checkbox"/>
GRA&I	<input type="checkbox"/>
DDC TAB	<input type="checkbox"/>
Unannounced	
Justification	
By _____	
Distribution/	
Availability Codes	
Dist	Avail and/or special
A	

## LIST OF ILLUSTRATIONS

<u>FIGURE</u>		<u>PAGE</u>
	<u>SECTION 2</u>	
1.	Block Diagram of Major Apparatus Components .....	2-31
2.	Cross Sectional View of High Temperature Flow Reactor .....	2-32
3.	Cross Sectional View of Analysis Region .....	2-33
4.	Measured Velocity Profile in Flow Tube .....	2-34
5.	Difference Between Nominal Readings and Measured Gas Temperatures .....	2-35
6.	Cross Sectional View of Molecular Beam Mass Spectrometer .....	2-36
7.	Cross Sectional View of Analysis Region with Infrared Absorption and Ultraviolet Absorption Diagnostics ....	2-37
8.	View of Low Spectral Resolution Infrared Optics .....	2-38
9.	View of High Spectral Resolution Infrared Optics .....	2-39
10.	Cross Section View of Analysis Region with Laser-Induced Fluorescence Diagnostics .....	2-40
	<u>SECTION 3</u>	
1.	Cross-Sectional View of the Aerodyne Research, Inc. Heated Flow Reactor .....	3-48
2.	Cross-Sectional View of Flow Reactor Analysis Region .	3-49
3.	External Optics of Flow Reactor .....	3-50
4.	Optical Schematic of Environmental Research Institute of Michigan Double Beam Emission-Absorption Spectrometer .....	3-51
5.	Equilibrium Calculations of Boron Species Combustion Products for $\text{BF}_3$ Flame Measurements at 2400 K .....	3-52
6.	Comparison of Theoretical and Experimental (Flow Tube) Determinations of the $\text{BF}_3 \nu_3$ Band Absorption Coefficients at 298K .....	3-53

## LIST OF ILLUSTRATIONS (CONT.)

<u>FIGURE</u>		<u>PAGE</u>
7.	Comparison of Theoretical and Experimental (Flow Tube) Determinations of the $\text{BF}_3 \nu_3$ Band Absorption Coefficients at 585K .....	3-54
8.	Comparison of Theoretical and Experimental (Flow Tube) Determinations of the $\text{BF}_3 \nu_3$ Band Absorption Coefficients at 870K .....	3-55
9.	Comparison of Theoretical and Experimental (Flow Tube) Determinations of the $\text{BF}_3 \nu_3$ Band Absorption Coefficients at 1150K .....	3-56
10.	Comparison of Theoretical and Experimental (Flow Tube) Determinations of the $\text{BF}_3 \nu_3$ Band Absorption Coefficients at 1440K .....	3-57
11.	Comparison of Theoretical and Experimental (Flame) Determinations of The $\text{BF}_3 \nu_3$ Band Absorption Coefficients at 2400K .....	3-58
12.	Theoretical Prediction of the $\text{BF}_3 \nu_3$ Band Absorption Coefficients at 300 and 600K .....	3-59
13.	Theoretical Prediction of the $\text{BF}_3 \nu_3$ Band Absorption Coefficients at 900, 1200, and 1500K .....	3-60
14.	Theoretical Prediction of the $\text{BF}_3 \nu_3$ Band Absorption Coefficients at 2000, 2500, and 3000K .....	3-61
15.	Theoretical Prediction of the $\text{BF}_3 \nu_3$ Band Line Density Parameter, $1/d$ , at 300 and 600K .....	3-62
16.	Theoretical Prediction of the $\text{BF}_3 \nu_3$ Band Line Density Parameter, $1/d$ , at 900, 1200, and 1500K .....	3-63
17.	Theoretical Prediction of the $\text{BF}_3 \nu_3$ Band Line Density Parameter, $1/d$ , at 2000, 2500, and 3000K .....	3-64
 <u>SECTION 4</u>		
1.	Top View of Flow Tube with Detail of Analysis Region Showing Confinement of Optically Active Gases by the Shield Flow .....	4-25
2.	Cross Sectional View of Analysis Region with Infrared Absorption and Ultraviolet Absorption Diagnostics ....	4-26
3.	Diode Laser Scan Through P(11) Line of $^{11}\text{BF}$ With $\text{CH}_4$ Reference Lines .....	4-27

(This Page Intentionally Left Blank)

## ABSTRACT

The objective of this research is the performance of quantitative infrared spectroscopic measurements of boron fluorides and oxides in the gas phase. The measurement program is designed to determine infrared absorption coefficients and absorption line spacings in order to facilitate the construction of infrared radiation band models.

In order to carry out these measurements an apparatus which permits the performance of quantitative spectroscopic measurements of transient species over the temperature range of 300 to 1500 K was constructed. The capability of this apparatus to perform these measurements over its designed range of operating parameters was demonstrated.

The infrared absorption coefficients of the  $\nu_3$  band of  $\text{BF}_3$  were measured over the range of 300 to 1500 K. These measurements were combined with flame measurements at 2400 K to develop and verify a radiation band model for  $\text{BF}_3$ . The formalism developed for this band model is more comprehensive than previous treatments and is generally applicable to perpendicular bands of symmetric top molecules.

The infrared band strength of BF was measured. The band strength was determined by measuring the absorption cross section of a single vibration-rotation line using a tunable diode laser as the light source. The BF number density was measured in-situ using ultraviolet absorption spectroscopy.

## 1. INTRODUCTION

The objective of this research program is the performance of quantitative infrared spectroscopic measurements on a number of boron oxides, fluorides, and oxy-fluorides. The measurement program is designed to produce results which are suitable for use in infrared radiation band models, and, therefore, the infrared absorption measurements may be performed at high spectral resolution, as well as at low spectral resolution. This permits the determination of the two band model parameters, the average absorption coefficient and the fine structure parameter. The measurements are performed within the temperature range of 300 to 1500 K. The candidate molecules for the study are  $\text{BF}_3$ ,  $\text{BF}$ ,  $\text{BO}_2$ ,  $\text{OBF}$ , and  $\text{HBO}_2$ . With the exception of  $\text{BF}_3$  which is a commercially available gas, these are transient species which must be produced in high temperature reactions.

This research has produced several significant accomplishments. These are:

- (1) The development of a versatile apparatus for the study of the spectroscopy and kinetics of transient species between 300 and 1500 K,
- (2) The measurement of the infrared spectral absorption coefficients of the  $\text{BF}_3$   $\nu_3$  band between 300 and 1500 K and the development of a radiation band model for this band, and
- (3) The measurement of the fundamental infrared band strength of  $\text{BF}$ .

The apparatus that was developed under this contract is basically a high temperature flow reactor which is suitable for the performance of quantitative spectral measurements of transient species over the temperature range of 300 to 1500 K. In addition to quantitative infrared spectroscopy at low or high spectral resolution, the apparatus is capable of studying transient species by ultraviolet absorption spectroscopy, laser-induced fluorescence, microwave discharge lamp

induced fluorescence, and molecular beam mass spectrometry. Finally, it should be noted that the apparatus can also be used to study the reaction kinetics of transient species. This apparatus is described in Section 2 which is a preprint of an article that will be submitted for publication in the Review of Scientific Instruments.

The spectral absorption coefficients of the  $\text{BF}_3 \nu_3$  band were measured over the temperature range of 300 to 1500 K. An advanced infrared radiation band model, which is generally applicable to perpendicular bands of symmetric top molecules, was formulated for  $\text{BF}_3$ . The spectral absorption coefficients measured in this study, along with those measured in a flame at 2400 K, were used to refine and verify the validity of the band model. These results are presented in Section 3 which is a preprint of an article that will be submitted for publication in the Journal of Chemical Physics. A preliminary version of this work appeared previously. (M.E. Gersh and C.E. Kolb, "Infrared Spectral Measurements of Species in a High Temperature Flow Tube," in Proc. 10th Materials Research Symp. on Characterization of High Temperature Vapors and Gases, J.W. Hastie, ed., NBS Special Publication 561 (1979), p. 679.)

The fundamental infrared band strength of BF was measured using a tunable diode laser as the radiation source. The BF was created in a 2450 MHz microwave discharge of a mixture of  $\text{BF}_3$  and He external to the flow reactor. The band strength was determined from a measurement of absorption cross section of the P(11) line of BF at 300 K. The BF number density was measured in-situ by ultraviolet absorption spectroscopy in the  $\text{BF } A^1\pi \leftarrow X^1\Sigma$  band head at 196 nm. These results are presented in Section 4 which is a preprint of an article that will be submitted for publication in the Journal of Chemical Physics.

## 2. A VERSATILE HIGH TEMPERATURE FLOW REACTOR FOR KINETIC AND SPECTROSCOPIC STUDIES

by

Michael E. Gersh, Joel A. Silver, Mark S. Zahniser,  
Charles E. Kolb, Robert G. Brown, Conrad M. Gozewski,  
Spiros Kallelis, and Joda C. Wormhoudt

### ABSTRACT

A high temperature flow reactor has been constructed to perform kinetic and spectroscopic studies on species at temperatures between 300 and 1500 K. The species in the flow reactor may be detected or studied using: laser induced fluorescence, resonance fluorescence, infrared absorption, ultraviolet absorption, chemiluminescence, or molecular beam mass spectrometry. The features of the apparatus are described in detail, and the initial spectroscopic and kinetic studies are discussed.

## INTRODUCTION

Flow tubes have been used routinely to perform kinetic measurements at temperatures between 200 and 600 K, and flame and shock tube techniques are commonly employed for temperatures above 1000 K. However, relatively few data are available in the 500 to 1500 K regime, which bridges the gap between low and high temperature measurements.<sup>1-4</sup>

On the other hand, flow tubes have not generally been employed in the performance of quantitative infrared measurements. These have most often been performed in static cells, shock tubes, and burners.<sup>5,6</sup> Static cells are not convenient for the study of transient species and are limited to approximately 1200 K. Shock tubes and burners are not generally useful below 1000 K, and they usually require equilibrium calculations of species number densities.

This paper describes a high temperature flow reactor which was developed to address both of these problems. It is designed to perform kinetic and spectroscopic studies over the temperature range of 300 to 1500 K. The kinetic measurements are facilitated by the capability to measure reactant and/or product number densities using a wide range of diagnostic techniques: laser induced fluorescence, discharge lamp resonance fluorescence, infrared absorption, ultraviolet absorption, chemiluminescence, and molecular beam mass spectrometry. In addition, the apparatus was designed to perform quantitative infrared absorption measurements, with the application of one or more of the other diagnostic capabilities to independently measure the number density of the absorb-

ing species. As a corollary, the multiplicity of diagnostic capabilities also permits the performance of visible/ultraviolet spectroscopic measurements of transient species.

## I. DESCRIPTION OF THE APPARATUS

### A. General

The high temperature flow reactor has been designed with the capability to perform both kinetic and spectroscopic studies of species at temperatures between 300 K and 1500 K. As a result the apparatus design is considerably more complicated than would be required if only kinetic studies were to be performed.<sup>4,7,8</sup> This is due to the fact that only relative species concentrations need be measured to determine (pseudo-first order) rate constants,<sup>1</sup> but absolute species concentrations and well-defined path lengths are required for the performance of quantitative spectroscopic measurements. In addition, the apparatus has been designed to accommodate a great variety of measurement techniques, thereby providing the flexibility to study a wide range of species.

A block diagram of the major apparatus components is shown in Fig. 1. A gas handling system external to the flow reactor is used to prepare the several gas flows that are introduced into the reactor. One (or more) of these flows may be passed through microwave discharges to produce radical species. In the flow reactor, gases may be mixed to produce the reactions whose rates are to be measured, or reactions may be carried out in order to produce transient species for spectroscopic studies. The flowing gases then pass into an analysis region where a variety of diagnostic techniques may be employed to characterize the species present. The following measurements may be performed: infrared absorption using either resonance or arc lamps, ultraviolet/visible discharge lamp induced resonance fluorescence, ultraviolet/visible laser induced fluorescence, and molecular beam mass spectroscopy. This versatility permits the study of almost any species.

## B. Vacuum Jacket and Flow Reactor

### B.1. Overall description

The detailed design of the variable temperature flow reactor is shown in Fig. 2. The outer vacuum jacket is constructed of steel and is water cooled, as are the aluminum end plate assemblies. The water cooling protects temperature-sensitive components and insures dimensional stability for optical components (such as the White cell mirrors) mounted on the vacuum jacket flanges. The upstream end plate holds the alumina flow tube, as well as power, gas, and thermocouple feedthroughs. The downstream flange is used for experiments for which mass spectrometer sampling is not required. When the mass spectrometer is employed, the flow reactor is mated directly to the outer vacuum wall of the mass spectrometer. In the analysis region, eight 10 cm inside diameter flanges are spaced equally around the circumference of the vacuum jacket. Four of these ports are connected by alumina tubes to the main flow tube and provide for optical analysis of the hot flowing gas. One of the remaining four ports is presently connected to a Kinney KMBD 1602 mechanical pump and Roots blower with an effective pumping speed of approximately 1000 cfm (450 l/sec).

The main elements of the thermal design include the heating elements and the surrounding layer of refractory insulation. The insulation is composed of a self-supporting "spool" of rigid alumina fiber insulation (Zircar Products, Inc.), upon which is wound several layers of Zircar alumina fiber blanket insulation, followed by additional layers of alumina-silica blanket insulation (Carborundum Corp.). The insulation assembly has an inside diameter of 15 cm and is designed to withstand continuous operating temperatures of 1800 K. The

commercially available Kanthal A-1 heating elements (Thermcraft, Inc., type RH) have a design temperature rating of 1500 K and are operated at 120 VAC. The heating elements are arranged in a three zone configuration to minimize temperature gradients due to end effects. The heated length is 78 cm, with a total power capability of approximately 8 kW. The heaters are supplied with power by solid-state proportional temperature controllers and power supply units (Love Controls, Corp.). The fully assembled flow reactor achieves a temperature of 1500 K with a power consumption of approximately 3 kW. The thermal stresses developed in the alumina flow tube components are small enough that the apparatus is routinely heated from room temperature to 1500 K in approximately 4-6 hrs, and no damage to the alumina components has occurred during the 1½ years that the heated flow reactor has been in use.

The design of the gas flow system within the variable temperature flow reactor is relatively complicated due to the constraints required to provide the capability of performing quantitative spectroscopic measurements in the analysis region. The main flow in the 7.3 cm inside diameter 99.8% alumina flow tube is usually composed of He or Ar carrier gas. This gas is heated as it passes through two heat exchangers which are 2.5 cm thick mullite "honeycomb" hole arrays with 1.6 mm round holes and a 67% frontal open area (General Refractories Co.). These heat exchangers are required to heat the carrier gas at high flow rates (large Reynolds numbers), and they also serve to laminarize the carrier gas flow. Downstream of the heat exchangers, two concentric 99.8% alumina injectors permit the introduction of reactive species into the flow.

The gas in the inner injector (9.5 mm i.d., 12.7 mm o.d.) may be passed through a commercial 2450 MHz microwave discharge cavity (Ophthos Instrument Co.) before being introduced approximately 1-2 cm upstream of the end of the outer injector (14.3 mm i.d., 19.1 mm o.d.). The microwave discharge is used to generate atoms and free radicals which can be injected directly into the main carrier gas flow or can be mixed with a reactant gas in the outer coaxial tube before being injected into the main flow. This arrangement permits a great deal of flexibility in the preparation of reactant species for study. The heated gas then passes through an isothermal region of the flow tube with constant cross section. In this region a second reactant species may be introduced into the flow via a movable injector for the measurement of rate constants.<sup>1</sup> The present movable injector is constructed of 6.3 mm o.d. quartz tubing (with a temperature limit of approximately 1250 K). The gas is injected into the main flow from a 5 cm o.d. loop of tubing having 16 0.4-0.5 mm diameter holes to promote rapid and uniform mixing.

The main flow with its mixture of reactive species then passes through a subsonic nozzle (area ratio 3.3:1, 4.0 cm i.d.) to enter the analysis region, as shown in Fig. 3. A second, external flow (shield flow) of pure carrier gas is heated to the temperature of the main flow as it passes between the heating elements and the outside of the flow tube. Then, after the shield flow passes through a subsonic nozzle which is concentric with the main flow nozzle, the flows merge. The area ratio of the main flow nozzle to the shield flow nozzle is 1:1, and the corresponding flow rates should ideally also be equal so that the velocities of the two flows will be the same when they meet downstream of the nozzles (in order to minimize mixing due to shear forces). This results

in a fluid dynamic confinement of the reactive species in the main flow as they pass through the analysis region. In addition, small flows of carrier gas are added to each of four optics tubes as a purge gas in order to keep the optics clean. The flow of purge gas into the optics tubes is generally set at approximately 10 percent of the main flow (equally divided between the four optics tubes), although this ratio is not critical. The six flows of gas meet in the analysis region volume which is defined by a six-arm cross piece that is made from machinable alumina ceramic (Cotronics Corp. type 960). The cross piece supports the four optics tubes and the flow tube. (The front of the flow tube rests on two sapphire balls, thereby permitting the flow tube to expand without generating any stress on the cross piece.) However, the main purpose of the cross piece is to provide an environment in which the main flow from the flow tube will be well behaved as it traverses the optical analysis region, impinges on the mass spectrometer sampling orifice, and is exhausted by the mechanical pump. Thus, the design of this element of the flow system is particularly important to the success of the experimental program, and separate experimental studies, described below, were undertaken in order to insure that the design would adequately control the gas flow in the analysis region.

#### B.2. Flow simulation experiment

A crucial element of the apparatus design is the configuration of the flow system in the spectroscopic analysis region. In order for one to be able to perform quantitative spectroscopic measurements on the species

in the main flow, three criteria must be satisfied: (1) geometry of the gas flow must be well defined as it traverses the analysis region, (2) the flow in this region must be stable, and (3) the temperature of the gas flow must be well defined (preferably isothermal). These criteria may be satisfied by maintaining a stable cylindrical flow, without recirculation of absorbing species in the optics tubes. For high temperature gas flows and/or multi-pass absorption cells, this necessitates the use of a wall-less confinement of the absorbing gas species as they pass through the analysis region. This can only be accomplished by fluid mechanical confinement of the flowing gas.

Since this portion of the apparatus represented a novel design, it was felt that its design should be tested in a flow simulation experiment before the fabrication of the six-arm cross piece out of machinable alumina ceramic. This obviated the need for a major system redesign if the initial design proved to be inadequate and would establish the approximate range of operating flow conditions over which the fluid mechanical confinement of the absorbing species would be effective.

The flow simulation experiment was set up in the following manner: a half scale model of the flow system was fabricated out of plastic (polymethyl methacrylate) with flowmeters monitoring the main flow, the shield flow, and the four purge flows. The gas flow was simulated by using a water flow with the same Reynold's number, which is a standard technique in fluid mechanics and is valid for subsonic, incompressible flows.<sup>9</sup> The flow pattern is determined by injecting Fluorescein dye into any one of the water flows and observing the bright fluorescence induced by illumination with a tungsten/halogen lamp.

The water flow velocity required for the simulation is obtained from the flow velocity of (for example) Ar that is to be simulated by equating the Reynolds numbers of the flows:

$$Re = \frac{\rho u d}{\eta} = \frac{\rho' u' d'}{\eta'} \quad (1)$$

where  $\rho$  is the density,  $u$  is the flow velocity,  $d$  is the tube diameter,  $\eta$  is the viscosity, and the prime refers to the conditions for water. Then, we let  $d' = d/2$  and  $\rho = \rho_0 P$ , where  $\rho_0 = 2.35 \times 10^{-6} \text{ g/cm}^3/\text{Torr}$  and  $P$  is the Ar pressure in Torr. Also,  $\rho' = 1.0 \text{ g/cm}^3$ ,  $\eta = 2.2 \times 10^{-4} \text{ poise}$ , and  $\eta' = 1.0 \times 10^{-2} \text{ poise}$  (at 293 K). This leads to the expression for the water flow velocity  $u'$  required for the simulation:

$$u' = 2.1 \times 10^{-4} P u \quad (2)$$

To simulate Ar flows at other temperatures, one would have to substitute the appropriate values of  $\rho_0$  and  $\eta$ .

The flow simulation experiment was actually performed for a slightly different apparatus configuration from that shown in Fig. 3. In particular, the nozzle for the main flow had an area ratio of 2.1 (ratio of main flow to shield flow = 2:1),<sup>10</sup> as opposed to the area ratio of 3.3 currently used in the high temperature flow reactor. The flow reactor was initially constructed with the smaller area ratio nozzle, but this design proved to be marginal for

reasons to be discussed below. The current configuration is more "conservative" with regard to the confinement of the main flow gas, and the general conclusions of the flow simulation experiment would therefore still be valid for the present design.

When the flow simulation experiments were performed, a number of interesting results were observed. The major result is that with a main flow Reynolds number greater than approximately 100 (for main:shield:purge flow rate ratios of 10:5:1) the main flow appears to be stable and cylindrical in form as it passes through the analysis region. Under these stable flow conditions, no recirculation pattern of the main flow water was observed in the "optics tubes". At lower Reynolds numbers the flow became unstable and main flow water entered the optics tubes. In addition, when dye was added to the water of the shield flow, a strong recirculation pattern of shield flow water was observed in the optics tubes, and this phenomenon persisted even at the highest main flow Reynolds number (560) used in the experiments. Thus, it may be concluded that a simpler flow configuration without a shield flow would not satisfy the analysis region design criteria since there would be recirculation of absorbing gas in the optics tubes. The more sophisticated design is successful because only the non-absorbing shield gas recirculates in the optics tubes, while the main flow of absorbing gas is confined by the shield flow to a cylindrical region in the center of the analysis region. In addition, since the shield gas will nominally be at the same temperature as the main flow, the column of absorbing gas should be essentially isothermal.

Although a flow simulation experiment of this type can successfully predict the bulk fluid dynamic properties of an apparatus, it has a shortcoming in that it can not simulate the effect of diffusion in the gas phase. This is important because species in the main flow which diffuse into the shield flow could recirculate in the optics tubes. This was observed to occur during a series of experiments to measure the temperature dependence of the spectral absorption coefficients of the  $\nu_3$  band of  $\text{BF}_3$ ,<sup>11</sup> at which time the apparatus was operated in its original configuration with a main flow nozzle area ratio of 2.1. Subsequently, this area ratio was increased to 3.3 (the present design). In this configuration the main flow was determined to be well confined during measurements of the infrared band strength of  $\text{BF}_3$ .<sup>12</sup> In addition, it was possible to verify visually the confinement of the main flow by observing in the analysis region the afterglow of an air discharge under the flow conditions used in the  $\text{BF}_3$  experiments. This flow visualization experiment confirms that the apparatus is capable of successfully confining the species in the main flow as they pass through the analysis region. However, when different flow conditions are employed, it would be advisable to repeat the flow visualization experiment for those conditions in order to verify the confinement of the species in the main flow.

### B.3. Flow tube diagnostics

In the course of performing kinetic and spectroscopic studies, a number of key parameters which characterize the gases must be accurately known. Calibration measurements to determine the temperature, pressure, flow rates, and flow development of the gases in the flow reactor are described in this section.

### Radial Velocity Distribution of the Flow

Laminar flow exists in the main flow as long as the Reynolds number is below 2000. This is true for all present applications of the apparatus. When the carrier gas is introduced through the mullite arrays, the flow has a uniform radial velocity distribution (plug flow). As the gas flows down the tube, its velocity profile eventually becomes parabolic (Poiseuille flow). In analyzing kinetic data, the corrections for diffusion depend on the extent to which the flow has developed. Since the most accurate solutions to the flow equations which account for both radial and axial diffusion, as well as wall removal<sup>13-15</sup> assume completely developed Poiseuille flow, it is desirable to operate in this regime. The inlet length required to fully develop parabolic flow is<sup>16-18</sup>

$$Z \approx R_e d / 16 \quad (3)$$

where  $R_e$  is the Reynolds number and  $d$  the tube diameter. In the present apparatus the distance from the laminar discs to the position where reactants are injected for kinetic measurements is ~25 cm. Thus, fully developed flow will present if  $R_e \leq 55$ . Typically,  $R_e \leq 10$  in our kinetics experiments so that the requirements should be satisfied.

To verify this, we constructed a Pitot tube,<sup>17</sup> which measures the dynamic pressure of the gas as a function of radial position. For a compressible fluid, this pressure can be related to the flow velocity by<sup>19</sup>

$$v = 2.22 \times 10^5 \left\{ \left( \frac{\gamma}{\gamma-1} \right) \frac{1}{M} \left[ \left( \frac{P}{P_0} \right)^{\frac{\gamma-1}{\gamma}} - 1 \right] \right\}^{1/2} \text{ cm/s} \quad (4)$$

where  $P_0$  is the static pressure,  $P$  is the dynamic pressure,  $\gamma$  the heat capacity ratio, and  $M$  the gram molecular weight. For He at 294 K, a Reynolds number of 30, and at a distance of ~25-30 cm from the mullite arrays, the data shown in Fig. 4 were obtained. The circles are the measured velocities and the solid line is a parabola normalized to the center velocity. Poiseuille flow has been clearly established.

#### Gas Temperature Measurements

In any spectral or kinetic measurement, the gas temperature must be known. The problems encountered in measuring the gas temperature in a variable temperature flow reactor are twofold. First, the gas must be heated to the desired operating temperature before it reaches the reaction and measurement region of the tube and second, an ordinary thermocouple receives more energy via radiation from the walls than from the gas, leading to an erroneously high reading. The latter problem has been overcome by using a dual shielded thermocouple arrangement<sup>3,20</sup> which was used to calibrate the temperature controller readings as a function of gas Reynolds number. As mentioned earlier, gas heating is accomplished with two mullite multihole arrays.

Moffat<sup>20</sup> has shown that under laminar flow conditions and with a properly designed thermocouple, the major source of error in the reading arises from radiative heat transfer between the TC junction and the reactor walls. This error is reduced by heat shields at least as much as a factor of  $(n+1)$ , where  $n$  is the number of concentric shields around the thermocouple. By comparing the readings from a doubly shielded and unshielded thermocouple, this error term can be calculated and the true gas temperature measured.

Such a device was constructed, using W-5%Re/W-26%Re thermocouples (.010" dia.), referenced to 0°C, and alumina tubular shields. The inner shield is 12 mm OD and the outer one 57 mm OD. Both are 0.5 mm thick and 7.5 cm long. Support is provided by very thin alumina tubes used as struts to minimize any conductive heat transfer. The unshielded thermocouple is ~5 cm upstream of the shielded TC.

The probe was inserted into the flow tube at a position midway through the kinetic measurements region. The corrected gas temperature was compared with the reading obtained from the thermocouple on the heater controller as well as with the "nominal" value obtained by reading the scale on its temperature meter. This was done as a function of gas Reynolds number (using Ar and He at various flow settings) for five elevated temperatures. The precision of the TC readings was  $\pm 0.1$  K with an accuracy estimated at  $\pm 2$  K. The controller could be read to  $\pm 5$  K. The difference between the nominal readings and the measured gas temperatures are shown in Fig. 5. For  $R_e < 200$ , the true gas temperature is ca. 6 K lower than the nominal values. This varies by  $\pm 10$  K for various temperatures, but shows no particular trend. Thus for  $R_e < 200$ , the gas temperature is known to  $\pm 10$  K. The difference between the heater TC and measured gas temperatures exhibits the same behavior.

As  $R_e$  approached 500, the difference between the nominal and true values precipitously increased. This most likely occurs because the smaller diffusion and faster flow speeds at these Reynolds numbers allowed insufficient time for the gas to be heated. The addition of a third mullite array would probably extend the range of  $R_e$  where the temperature is well characterized. By providing additional surface area over which the gas must pass, more heat can be transferred.

#### Flow Rates and Gas Pressures

Pressures are measured using an MKS Baratron Model 222AHS100 (1.5% accuracy) or MKS Baratron Models 310-BHS10, 301-BHS100 (.08% accuracy). The injector loop is used to measure the static pressure inside the flow tube. This was compared to other probes in the arms and entrance to the tube and all readings agreed to within 1%. Gas volumetric flow rates are obtained using Matheson rotameters which are periodically calibrated for each gas used.

## C. Measurement Capabilities

### C.1. Mass spectrometer

A molecular beam mass spectrometer may be interfaced to the high temperature flow reactor in order to measure the number density of species in the main gas flow. A cross sectional view of the mass spectrometer in a horizontal plane is shown in Fig. 6. A novel feature of the design is the capability to measure the mass spectra of gases sampled from two independent apparatus located at right angles to each other. Currently, the apparatus which is located in the axial beam position (at the left of the figure) is an atmospheric pressure, pulverized coal burner, for which the mass spectrometer measures the neutral and ionic species in the burner flame.<sup>21</sup> This burner will not be discussed further in the present paper. However, it should be noted that the axial beam skimmer and the two inner chambers may be electrically biased individually in order to facilitate the measurement of ionic species. (For simplicity, the additional ion optics are not shown in the figure.)

The high temperature flow reactor is located in the crossed beam position (at the top of the figure). From either of the two apparatus positions, the instrument operates as a conventional molecular beam mass spectrometer.<sup>22</sup> There are three stages of differential pumping. The first (nozzle-skimmer) chamber is pumped by a 16 in. diffusion pump (Varian type HS16), the middle chamber is pumped by a 4 in. diffusion pump (Varian type VHS-4), and the mass spectrometer chamber is pumped by a 6 in. diffusion pump (Varian type VHS-6). A three position gate valve mounted on the innermost

chamber permits operation of the mass spectrometer in one of three modes: cross beam entrance and exit apertures open and axial beam entrance aperture closed (so that the mass spectrometer can be kept evacuated with the outer two chambers at atmospheric pressure). Choppers (Bulova Corp.) located on the gate valve assembly permit the beams to be modulated before they enter the mass spectrometer chamber, thereby permitting the use of synchronous detection techniques for discrimination against background gases. The mass spectrometer proper is a standard commercial unit (Extranuclear Laboratories, Inc.) except for the ionizer (model 041-2) which has been modified to accept a cross beam, as well as an axial beam.

The present molecular beam mass spectrometer is a recent addition to the apparatus, and, therefore, its ultimate capabilities have yet to be realized. At the present time, when it is operated with completely resolved mass peaks ( $\Delta m \approx \frac{1}{2}$  amu), it is capable of detecting (signal-to-noise ratio = 1, 1 sec time constant on lock-in amplifier) species at approximately 4 ppm for the cross beam at a source pressure of 2 Torr and approximately 1 ppm for the axial beam at a source pressure of one atmosphere.

## C.2. Infrared absorption

The high temperature flow reactor has been designed with the capability to perform quantitative measurements of infrared spectral absorption coefficients. These measurements may be performed either at low spectral resolution using a

broadband radiation source and monochromator or at very high spectral resolution using a tunable diode laser as the radiation source. The infrared optical system is divided into two major subassemblies: one inside the flow reactor vacuum jacket and one external to the vacuum jacket.

The internal infrared optical system is shown in Fig. 7, which is a cross sectional view of the flow reactor in the analysis region. The internal optics are composed of three spherical mirrors (43.0 cm radius of curvature) which form a multi-pass absorption cell (White cell).<sup>23</sup> The White cell is capable of producing approximately 100 passes through the absorbing gas in the main flow, but it is typically operated in the range of 28-52 passes, which is a compromise between increased path length (optical depth) and increased reflectance losses as the number of passes is increased. The height of the "envelope" of infrared beams passing through the main flow is typically on the order of 2 cm, as compared with the main flow diameter of approximately 4 cm.

The design of the low spectral resolution, double beam external optical system is shown in Fig. 8. The infrared radiation source is a Perkin-Elmer Corp. "Opperman Source" which is used in their current infrared spectrometers. The radiation impinges on a mirror-bladed, 50 percent duty cycle chopping wheel (Valtec Corp.) which alternately allows it to pass into the White cell or reflects it, thereby bypassing the White cell. In Fig. 8, M2, M3, M4, M7 and M8 are flat mirrors; M1 and M9 are spherical mirrors; and M5 and M6 are off-axis paraboloid mirrors. The beam splitter is made of

uncoated zinc selenide, the monochromator is a Spex Minimate, and the detector is a Santa Barbara Research Corp. HgCdTe photoconductive detector. In front of this is placed an order-sorting (long-wavelength pass) filter to avoid interference from higher order diffraction in the monochromator. Since the optical system consists of reflective optics (except for the zinc selenide beam splitter), it is achromatic, and it can be aligned with the use of a helium-neon laser.

The design of the high spectral resolution external optical system is shown in Fig. 9. This system shares many of the components of the low spectral resolution system. The tunable diode laser is mounted in a closed cycle refrigerator (both from Laser Analytics, Inc.). The laser radiation is focused by a KRS5 lens on the monochromator slit, and the monochromator is used to isolate a single laser mode. Before entering the White cell, the laser radiation is chopped so that lock-in detection techniques can discriminate against blackbody radiation from the heated flow reactor which impinges on the HgCdTe detector. With the diode laser, either direct absorption or derivative absorption<sup>24</sup> techniques may be used to measure the absorption cross sections of individual spectral lines. This capability of detecting individual lines, as well as the relatively high laser power, permits an increase in measurement sensitivity compared to low spectral resolution detection techniques. At low spectral resolution, a  $\text{BF}_3$  number density of  $\sim 3 \times 10^{13} \text{ cm}^{-3}$  may be detected using the  $\nu_3$  band (signal-to-noise = 1, time constant = 0.4 sec).<sup>11</sup> On the other hand, at high spectral resolution

a BF number density of  $\sim 10^{11} \text{ cm}^{-3}$  may be detected by direct absorption measurements, and a BF number density of  $\sim 2 \times 10^{10} \text{ cm}^{-3}$  may be detected using derivative absorption techniques (signal-to-noise = 1, time constant = 0.4 sec).<sup>12</sup>

### C.3. Laser-induced fluorescence

The use of laser-induced fluorescence extends the capability and sensitivity of detection to species such as  $\text{NH}_2$ . A nitrogen-pumped dye laser (Molelectron DL14P) is introduced through the bottom arm of the flow tube (Fig. 10). In this configuration, the resonance lamp is removed and Brewster windows added to the arms along the laser path to prevent beam scattering. The visible laser beam is expanded to 12 mm diameter to avoid any possible saturation effects. (In the UV, this is unnecessary because that laser power is lower.) After passing through the flow tube, a portion of the beam is split off into an ITT FW-114A fast vacuum photodiode which is used as a power monitor. The fluorescence is imaged into a photomultiplier which is perpendicular to the path of the laser beam.

For each laser pulse, there are  $10^{13} - 10^{15}$  photons. Even with good baffling, scattered light may create severe background problems. To avoid this, a gated detection system is used, and is controlled by a master electronics console, designed and built at Aerodyne.<sup>25</sup> This unit initiates the laser pulse, and after the desired delay time, gates the PMT on (20 ns risetime).<sup>26,27</sup> The fluorescence is amplified, integrated, and fed to a peak detector, where the signal is held until read into a Prime 400 computer

via an IBM 7406 interface. The unit controls all delay and data integration times in increments of 10 ns. A parallel channel repeats this process for the laser power monitor. The laser is fired on alternate clock periods and the signal (difference between laser-on and laser-off values, normalized to the laser power for each pulse) is computed and displayed in real time on a video terminal. For a typical species such as OH, a concentration of  $\sim 10^9$  molecules  $\text{cm}^{-3}$  can be detected in 10 seconds of counting with signal/background = 1.

#### C.4. Resonance fluorescence

A variety of atomic and molecular species can be detected using resonance fluorescence techniques. A general schematic of this configuration is illustrated in Figs. 2 and 10. The quartz resonance lamp is made by flowing the desired species, entrained in an inert carrier, through a 2450 MHz microwave discharge and focussing the resulting emission into the flow tube.

Fluorescence is imaged from the central 12 mm diameter region of the analysis region of the flow tube onto a photomultiplier configured for photon counting. The PMT is mounted on an arm perpendicular to the resonance lamp. The counts are amplified and discriminated by a Pacific Precision Instruments Model 3262/AD6 amplifier-discriminator and fed to a Monsanto 1505A Counter-Timer. Appropriate interference filters are used to isolate the emission lines from unwanted scattered light, which can be very intense at elevated temperatures.

When detecting oxygen or hydrogen atoms, a solar blind EMI G-26E315 photomultiplier is used, with optics constructed from  $\text{MgF}_2$ . For all other species (BF, NO, OH,  $\text{NO}_2$  etc.), quartz optics and a Hamamatsu R763P phototube (160-850 nm response) are used.

As shown in Figs. 2 and 10, the optical paths are protected from stray light by black anodized aluminum baffles. Opposite the PMT is a blackened light trap, which suppresses scattering light so that the PMT views no direct source of emission other than the fluorescing gases. It is estimated that scattered light is attenuated by  $\sim 10^{12}$ . For a typical species such as NO, a concentration of  $\sim 1.3 \times 10^{10}$  molecules  $\text{cm}^{-3}$  can be detected in 10 seconds of counting with a signal/background = 1.

#### C.5. Ultraviolet absorption

Species which have moderate absorption coefficients in the UV may be detected by direct absorption of continuum radiation from a xenon arc lamp (Varian Model VIX-500 UV). The lamp has a total output of 12 W integrated from 200 to 400 nm. Although the intensity decreases rapidly below 220 nm, there is still a useful continuum from 190 to 200 nm of 1 mW/nm. As shown in Fig. 7, the light is collimated by an internal parabolic reflector, passes through the center of the detection region, and is focused by a quartz lens onto the slit of a 1 m monochromator (McPherson Model 2051). The 1200 line/mm grating is blazed at  $3000 \text{ \AA}$  and gives a resolution in first order of  $0.1 \text{ \AA}$  with  $10 \text{ \mu m}$  slits. A beam splitter deflects a portion of the lamp output onto a reference photomultiplier tube so that intensity fluctuations may be compensated by ratioing the two beams. The optical axis for the UV absorption is perpendicular to the infrared axis permitting simultaneous measurements by the two techniques. For a typical species such as BF, a number density of  $\sim 2 \times 10^{11} \text{ cm}^{-3}$  can be detected with a signal-to-noise = 1 with a time constant of 10 sec. This sensitivity is largely limited by fluctuations in the arc lamp.

#### C.6. Chemiluminescence

Visible and ultraviolet chemiluminescence spectra are taken by imaging emission from the central region of the flow axis onto the entrance slit of the monochromator using the same optical arrangement as in Fig. 7. Spectra are recorded with the IBM 7406 Interface and Prime 400 Computer using either analog or digital data from the phototube while wavelength is scanned by a stepping motor drive.

## II. OPERATION

The high temperature flow reactor has been used for several spectroscopic and kinetic studies. These studies will be summarized briefly in order to illustrate the versatility of the apparatus.

The temperature dependence of the infrared spectral absorption coefficients of the  $\nu_3$  band of  $\text{BF}_3$  was measured over the temperature range of 298 to 1440 K.<sup>11</sup> The  $\text{BF}_3$  was simply mixed with the carrier gas in the main flow, and the infrared absorption coefficients were measured at low spectral resolution. The  $\text{BF}_3$  number density in the flow tube was obtained from the gas flow rates and the pressure in the analysis region.

The infrared band strength of BF was determined to be  $630 \pm 200 \text{ cm}^{-2} \text{ amagat}^{-1}$  by measuring the integrated line strength of a single vibration-rotation line at high spectral resolution.<sup>12</sup> The BF was produced by passing a mixture of  $\text{BF}_3$  and He carrier gas through a microwave discharge. The BF number density in the analysis region was obtained by measuring its absorption of ultraviolet radiation along a path perpendicular to the path of the reaction of the infrared radiation.

The rate constant for the reaction of  $\text{OH} + \text{NH}_3$  was measured over the temperature range of 294 to 1075 K<sup>26</sup> and found to be  $(5.41 \pm 0.86) \times 10^{-12} \exp(-2120 \pm 143 \text{ cal mole}^{-1}/RT) \text{ cm}^3 \text{ molecule}^{-1} \text{ sec}^{-1}$ . The OH was produced by reaction of H (generated in a microwave discharge) with  $\text{NO}_2$ , and the  $\text{NH}_3$  was introduced into flow downstream through the ring injector. The progress of the reaction was monitored in the analysis region by measuring the OH number

density by resonance fluorescence or by measuring the  $\text{NH}_2$  product number density by laser induced fluorescence.

Finally, the rate constant for the reaction of  $\text{NH}_2 + \text{NO}$  was measured over the temperature range of 294 to 1200 K.<sup>29</sup> A least squares fit of the experimental data yielded the expression  $k(T) = (1.95 \times 10^{-4})T^{-2.46} \exp(-938/T)$   $\text{cm}^3 \text{ molecule}^{-1} \text{ sec}^{-1}$ . The  $\text{NH}_2$  was produced by reaction of F (generated in a microwave discharge) with  $\text{NH}_3$ , and the NO was introduced through the ring injector. In the analysis region the  $\text{NH}_2$  reactant number density was measured by laser induced fluorescence, the OH product number density was measured by laser induced fluorescence and resonance fluorescence, and the number densities of all the species in the main flow were measured using the molecular beam mass spectrometer.

ACKNOWLEDGEMENTS

The authors wish to express thanks to M. Camac, F. Bien, A. Stanton, W. Cheng, J. Purpura, A. Epstein, and J. Kerrebrock for many valuable and stimulating discussions. This work was sponsored by the Air Force Office of Scientific Research (AFSC) under Contract No. F49520-77-C-0075 and the Department of Energy Office of Coal Utilization under Contract No. ET-78-C-01-3183.

## REFERENCES

- <sup>1</sup>C.J. Howard, *J. Phys. Chem.* 83, 3 (1979).
- <sup>2</sup>D.L. Baulch and D.C. Montague, *J. Phys. Chem.* 83, 42 (1979).
- <sup>3</sup>A. Fontijn and W. Felder, *J. Phys. Chem.* 83, 24 (1979).
- <sup>4</sup>W. Felder, A. Fontijn, H.N. Volltrauer, and D.R. Voorhees, *Rev. Sci. Instr.* 51, 195 (1980).
- <sup>5</sup>C.B. Ludwig, W. Malkmus, J.E. Reardon, and J.A.L. Thomson, National Aeronautics and Space Administration Report NASA SP-3080 (1973).
- <sup>6</sup>L.A. Pugh and K.N. Rao, in Molecular Spectroscopy: Modern Research Volume II, edited by K.N. Rao (Academic Press, New York, 1976), p. 165, and references contained therein.
- <sup>7</sup>E.E. Ferguson, F.C. Fehsenfeld, and A.L. Schmeltekopf, *Adv. At. Mol. Phys.* 5, 1 (1969).
- <sup>8</sup>A. Fontijn, S.C. Kurzius, J.J. Houghton, and J.A. Emerson, *Rev. Sci. Instr.* 43, 726 (1972).
- <sup>9</sup>J. Kerrebrock, Massachusetts Institute of Technology, private communication.
- <sup>10</sup>M.E. Gersh and C.E. Kolb, in Proc. 10th Materials Research Symp. on Characterization of High Temperature Vapors and Gases, edited by J.W. Hastie, National Bureau of Standards Special Publication 561 (1979), p. 679.
- <sup>11</sup>M.E. Gersh L.S. Bernstein, and L. Peterson, "Measured and Predicted Band Model Parameters of  $\text{BF}_3(\nu_3)$  at High Temperatures," submitted to *J. Chem. Phys.*
- <sup>12</sup>M.S. Zahniser and M.E. Gersh, "Measurement of the Vibrational Band Strength of  $^{11}\text{BF}$  Using a Tunable Diode Laser," submitted to *J. Chem. Phys.*
- <sup>13</sup>R.L. Brown, *J. Res. NBF* 83, 1 (1978).
- <sup>14</sup>R.E. Walker, *Phys. Fluids* 4, 1211 (1961).
- <sup>15</sup>V. Poirier and W. Carr, Jr., *J. Phys. Chem.* 75, 1593 (1971).
- <sup>16</sup>H. Schlichting, Boundary Layer Theory (McGraw Hill, New York, 1968), p. 231.
- <sup>17</sup>H. Shames, Mechanics of Fluids (McGraw Hill, New York, 1962), pp. 293 and 318.
- <sup>18</sup>W.N. Kays, Convective Heat and Mass Transfer (McGraw Hill, New York, 1966), p. 60.
- <sup>19</sup>R. Binder, Advanced Fluid Mechanics Vol. I (Prentice Hall, Englewood Cliffs, New Jersey, 1958), p. 45.
- <sup>20</sup>R.J. Moffat, Temperature, Its Measurement and Control in Science and Industry, Vol. 3, Part 2, edited by A.I. Dahl, (Reinhold, New York, 1962), p. 553.

- 21 J.C. Wormhoudt and C.E. Kolb, Proc. 10th Materials Research Symp. on Characterization of High Temperature Vapors and Gases, edited by J.W. Hastie, National Bureau of Standards Special Publication 561 (1979), p. 457.
- 22 C.A. Stearns, F.J. Kohl, G.C. Fryburg, and R.A. Miller, ibid., p. 303.
- 23 T.H. Edwards, J. Opt. Soc. Am. 51, 98 (1961).
- 24 J. Reid, J. Schewchum, B.K. Garside, and E.A. Ballik, Opt. Eng. 17, 56 (1978).
- 25 C.M. Gozewski and J.A. Silver, Aerodyne Research, Inc. Report ARI-TM-11 (1980).
- 26 J.J. Ramirez and L.W. Kruse, Rev. Sci. Inst. 47, 832 (1978).
- 27 R. Oldenberg and W. Rice, Los Alamos Scientific Lab. (private communication).
- 28 J.A. Silver and C.E. Kolb, "Rate Constant for the Reaction  $\text{NH}_3 + \text{OH} \rightarrow \text{NH}_2 + \text{H}_2\text{O}$  over a Wide Temperature Range," accepted for publication in Chem. Phys. Lett.
- 29 J.A. Silver, C.M. Gozewski, and C.E. Kolb, "Chemical Kinetics of the  $\text{NH}_3/\text{NO}$  Reaction System under Combustion Exhaust Flow Conditions," accepted for presentation at the Fall 1980 Combustion Institute/Western States Symposium.

## FIGURE CAPTIONS

### Figure

1. Block diagram of major apparatus components.
2. Cross sectional view of high temperature flow reactor. A - alumina flow tube, B - water cooled vacuum jacket, C - refractory insulation, D - ring injector, E - six arm cross piece to support flow tubes, F - discharge lamp, G - microwave discharge cavity, H - quartz lens, I - flow of gas to pumps, J - optical tube perpendicular to drawing, K - mass spectrometer sampling orifice, L - optics tube purge gas (1 of 4), M - kanthal heating elements, N - multihole mullite array (heat exchanger), O - shield gas, P - carrier gas, Q - reactant gases.
3. Cross sectional view of analysis region.
4. Measured velocity profile in flow tube. Solid line is parabola normalized to data point on centerline.
5. Difference between nominal readings and measured gas temperatures.
6. Cross sectional view of molecular beam mass spectrometer. A - nozzle-skimmer chamber, B - middle chamber, C - mass spectrometer chamber, D - sampling nozzles, E - skimmers, F - choppers, G - gate valve assembly, H - mass spectrometer, I - nylon flanges permit electrical biasing for detection of ions from coal burner.
7. Cross sectional view of analysis region with infrared absorption and ultraviolet absorption diagnostics. Elements external to vacuum jacket not shown to scale. A - vacuum jacket, B - six arm cross piece, C - white cell mirrors, D - windows, E - arc lamp, F - beam splitter, G - interference filters, H - photomultipliers, I - mirror, J - quartz lens, K - chopper, L - monochromator.
8. View of low spectral resolution infrared optics. A - source, B - chopper, C - beam splitter, D - monochromator, E - detector, M1-M9 - mirrors.
9. View of high spectral resolution infrared optics. A - tunable diode laser, B - lens, C - monochromator, D - chopper, E - detector, M1-M8 - mirrors.
10. Cross section view of analysis region with laser induced fluorescence diagnostics. A - vacuum jacket, B - six arm cross piece, C - pulsed dye laser, D - beam expander, E - mirrors, F - Brewster angle windows, G - baffle assemblies, H - photodiode, I - light trap, J - quartz lens, K - interference filter, L - photomultiplier.

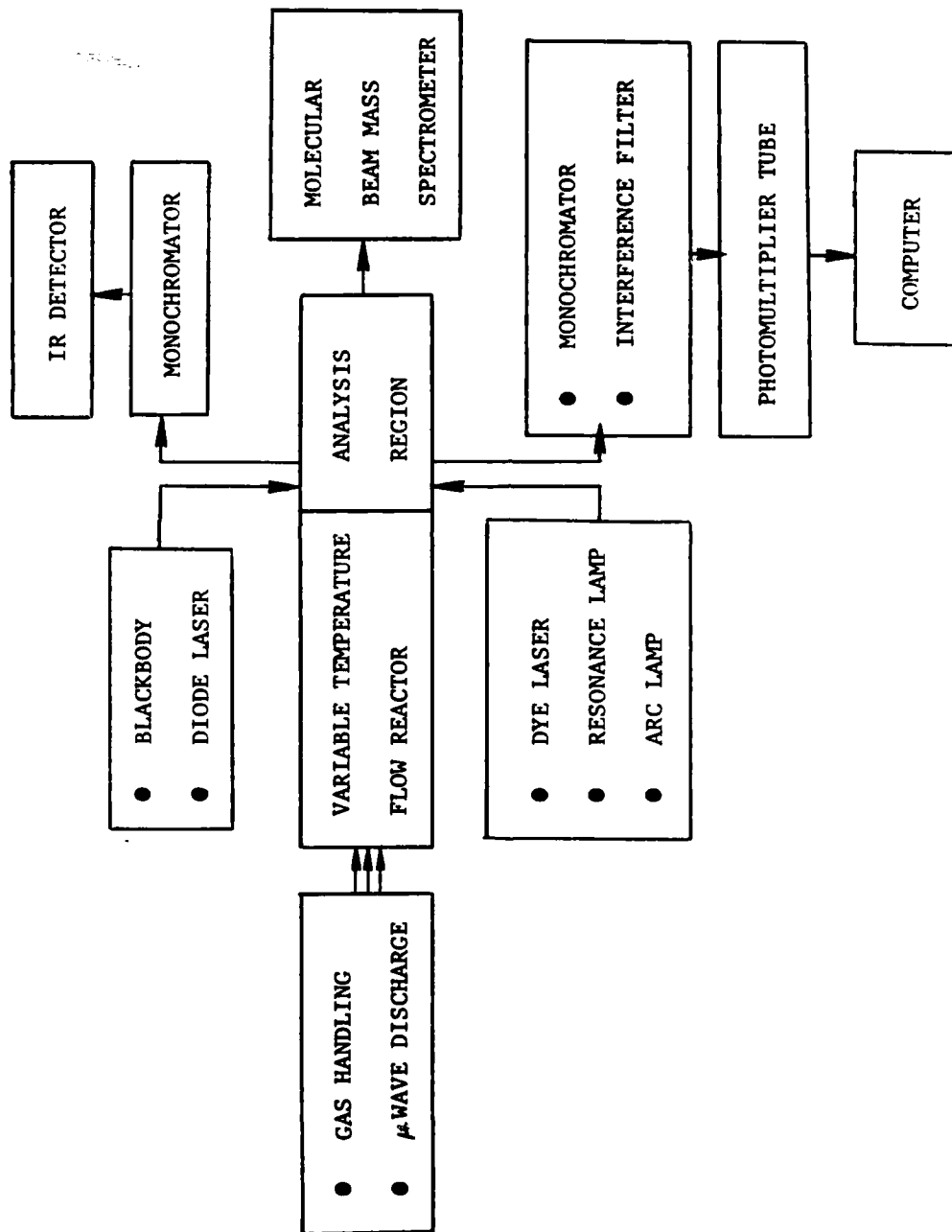


Figure 1

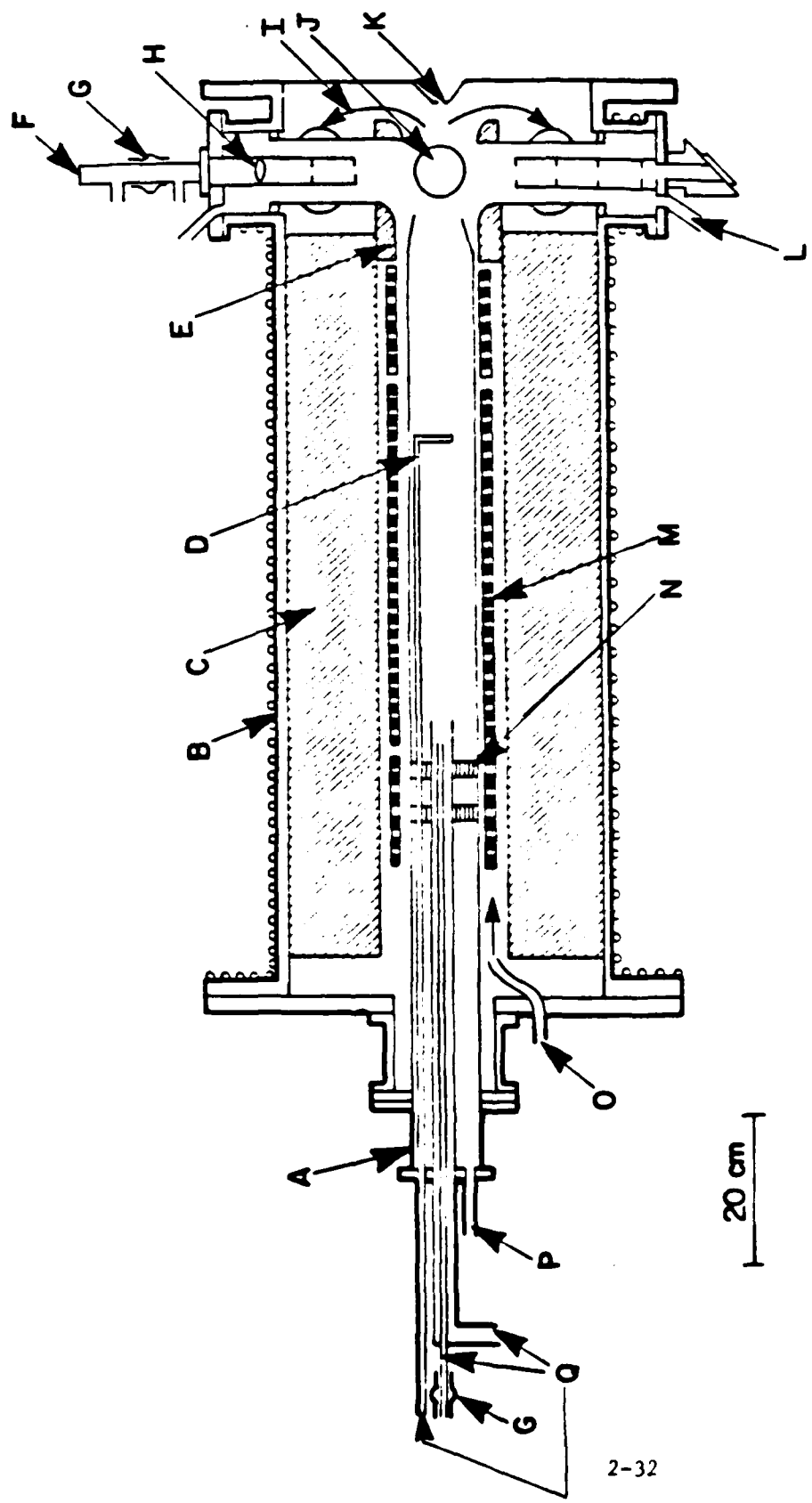


Figure 2

AL 79-449

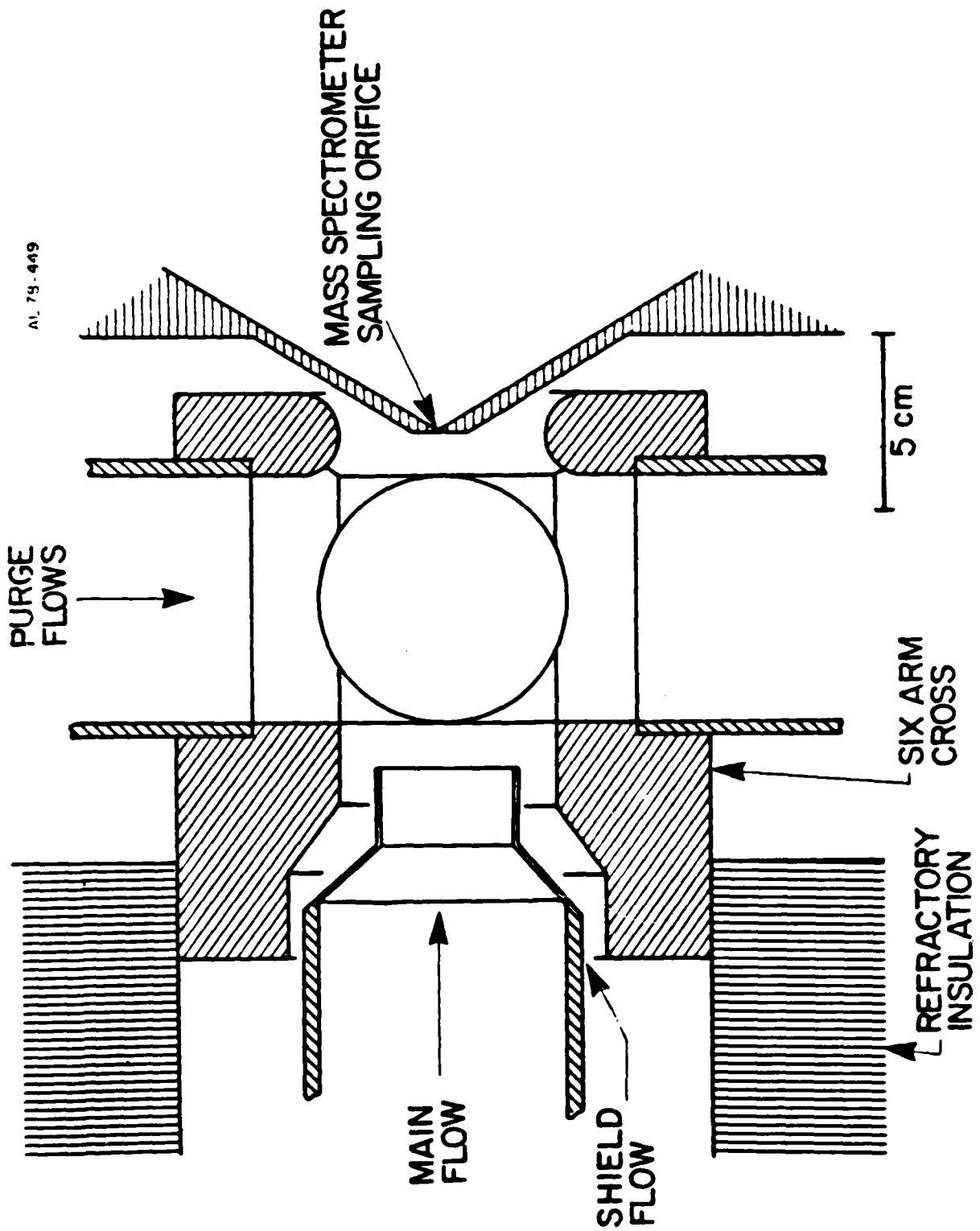


Figure 3

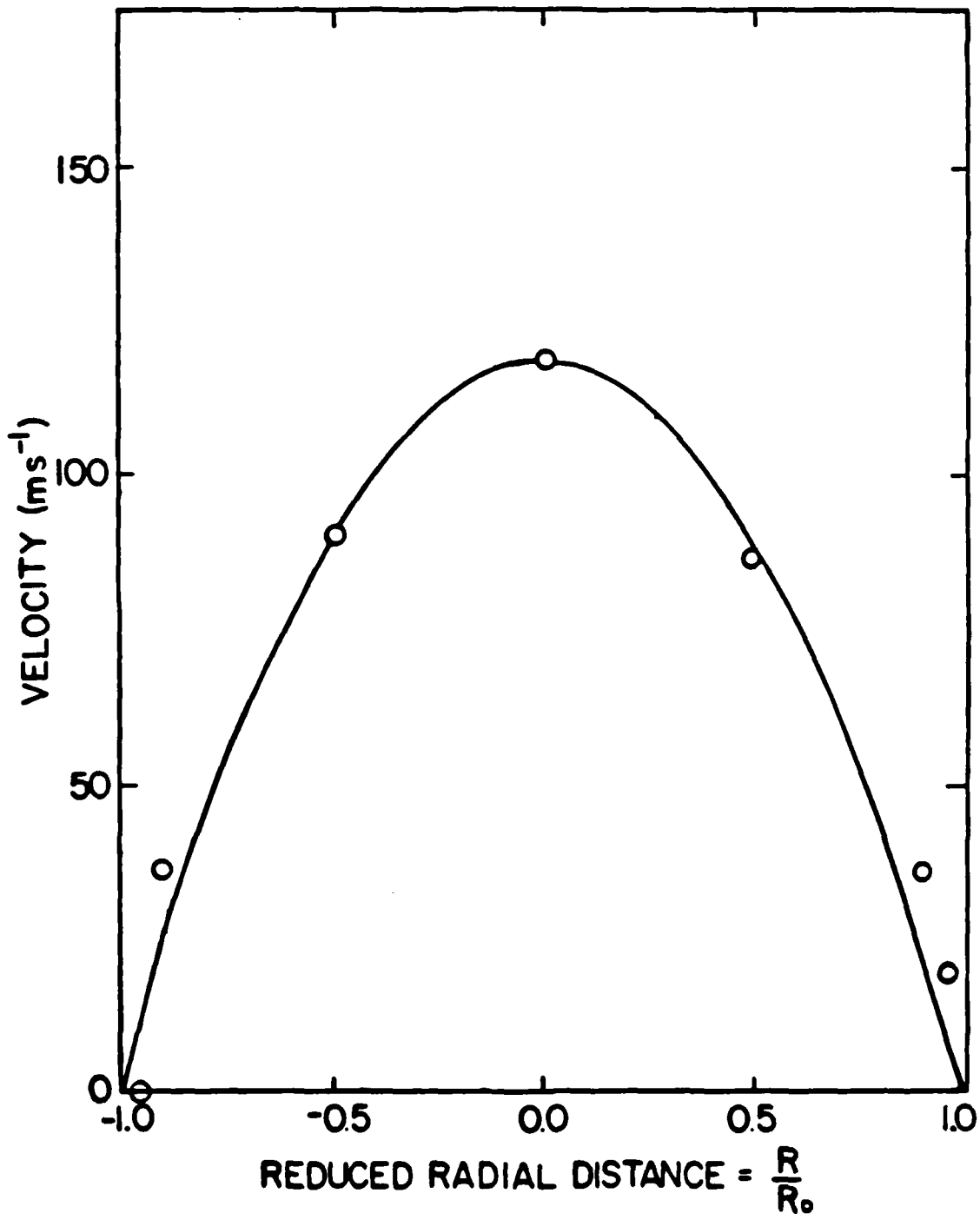
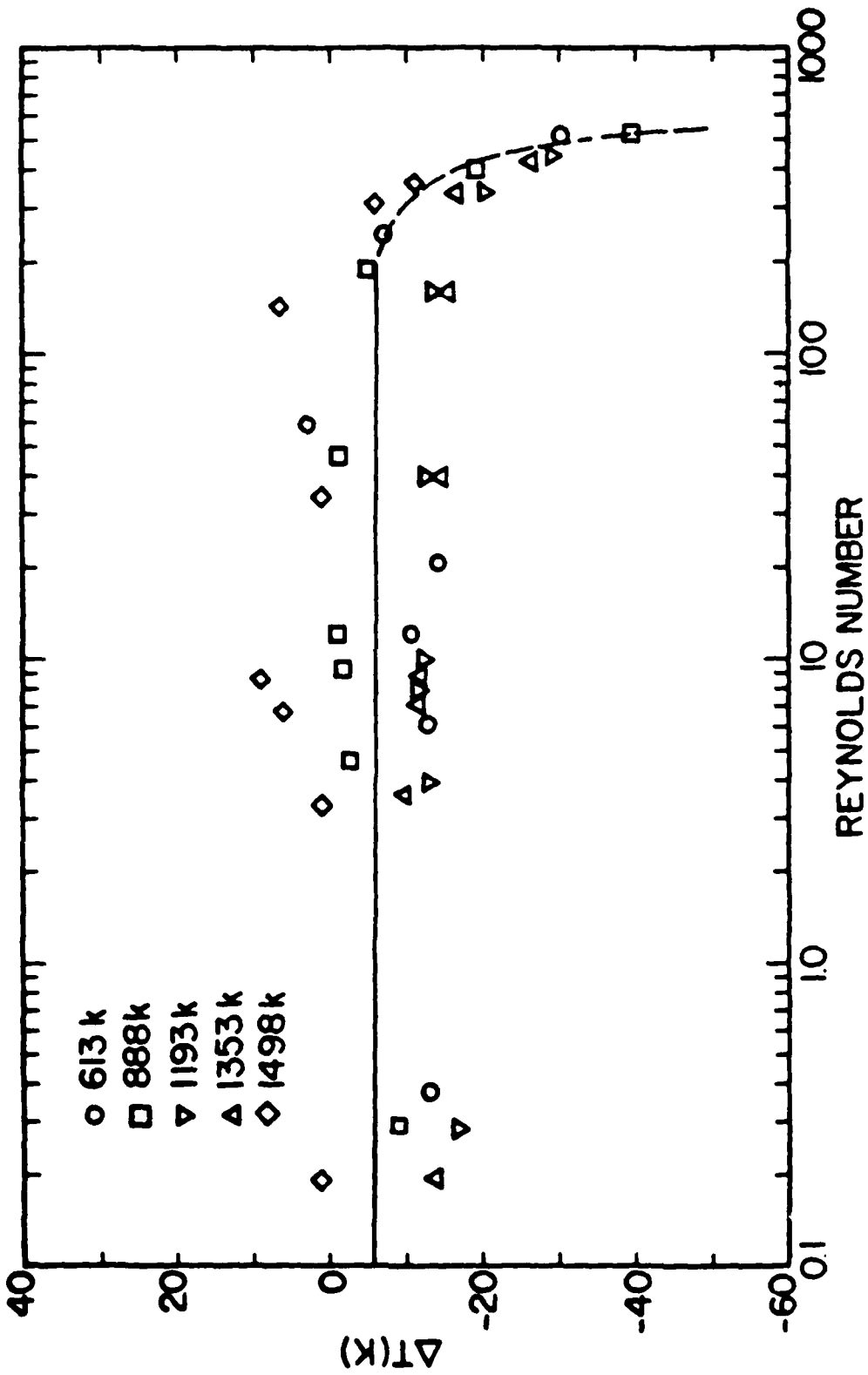


Figure 4.2. Velocity profile



2-35

Figure 5

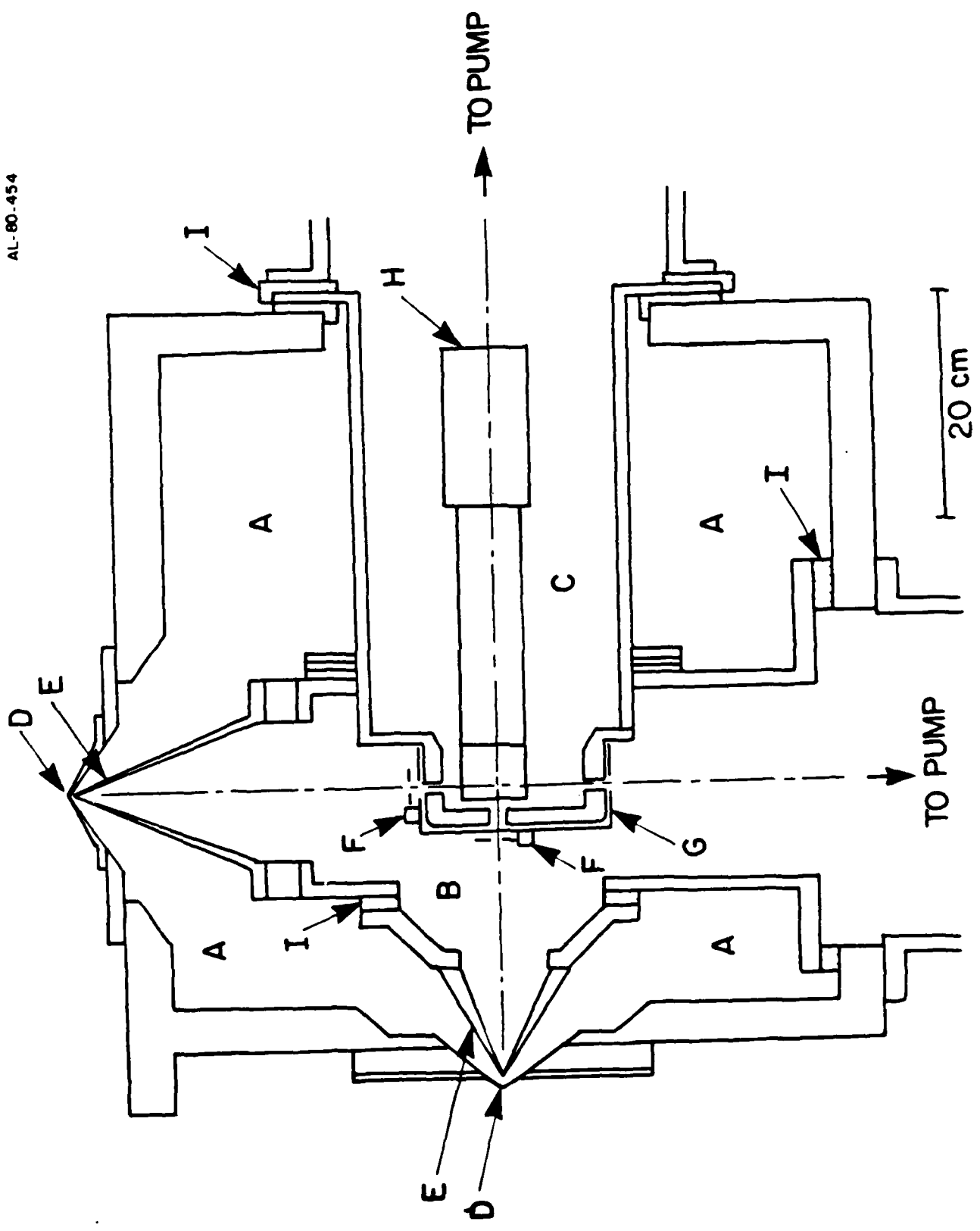


Fig. 6

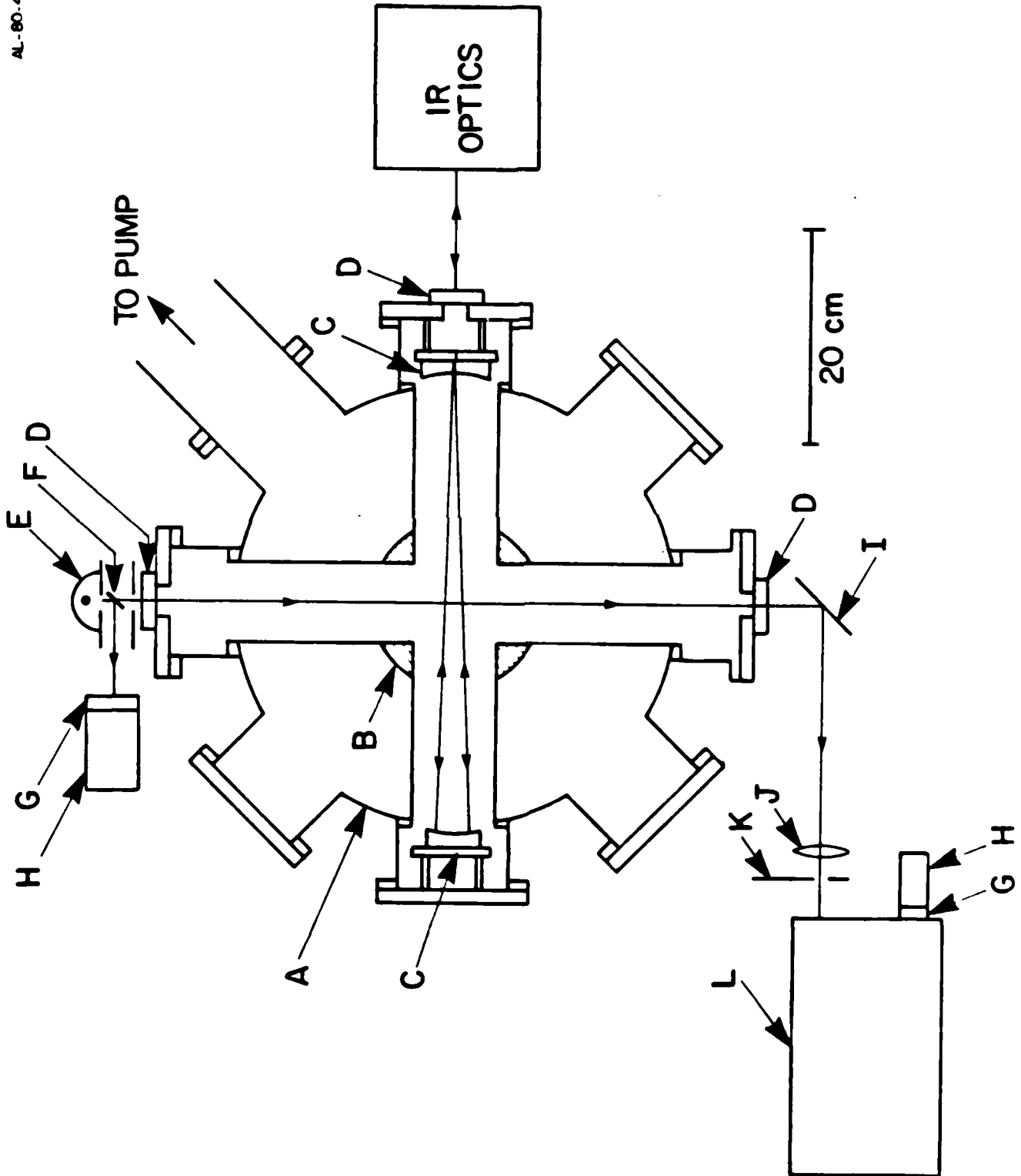


Figure 7

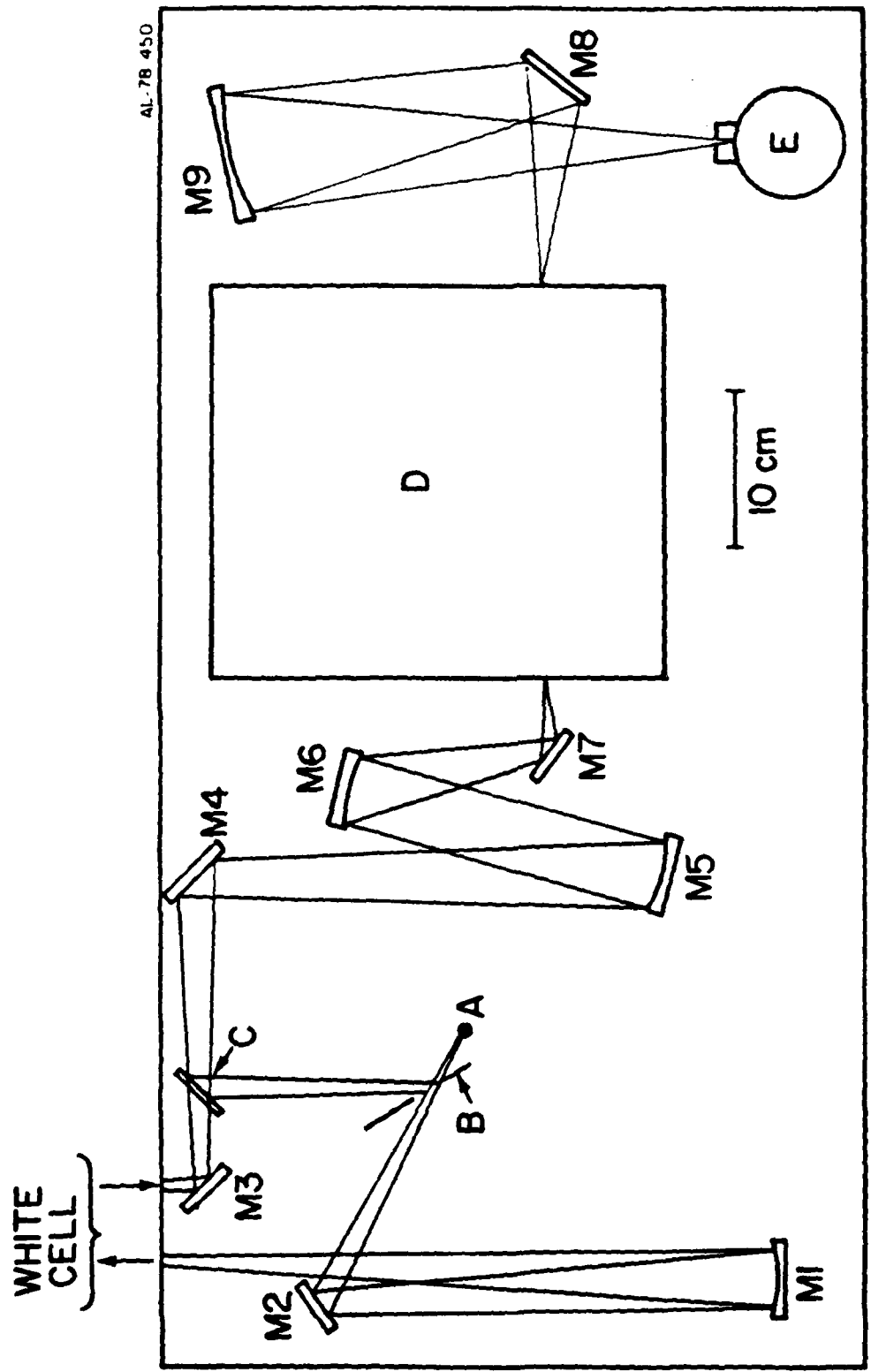


FIG. 8

AL-78-450A

WHITE CELL

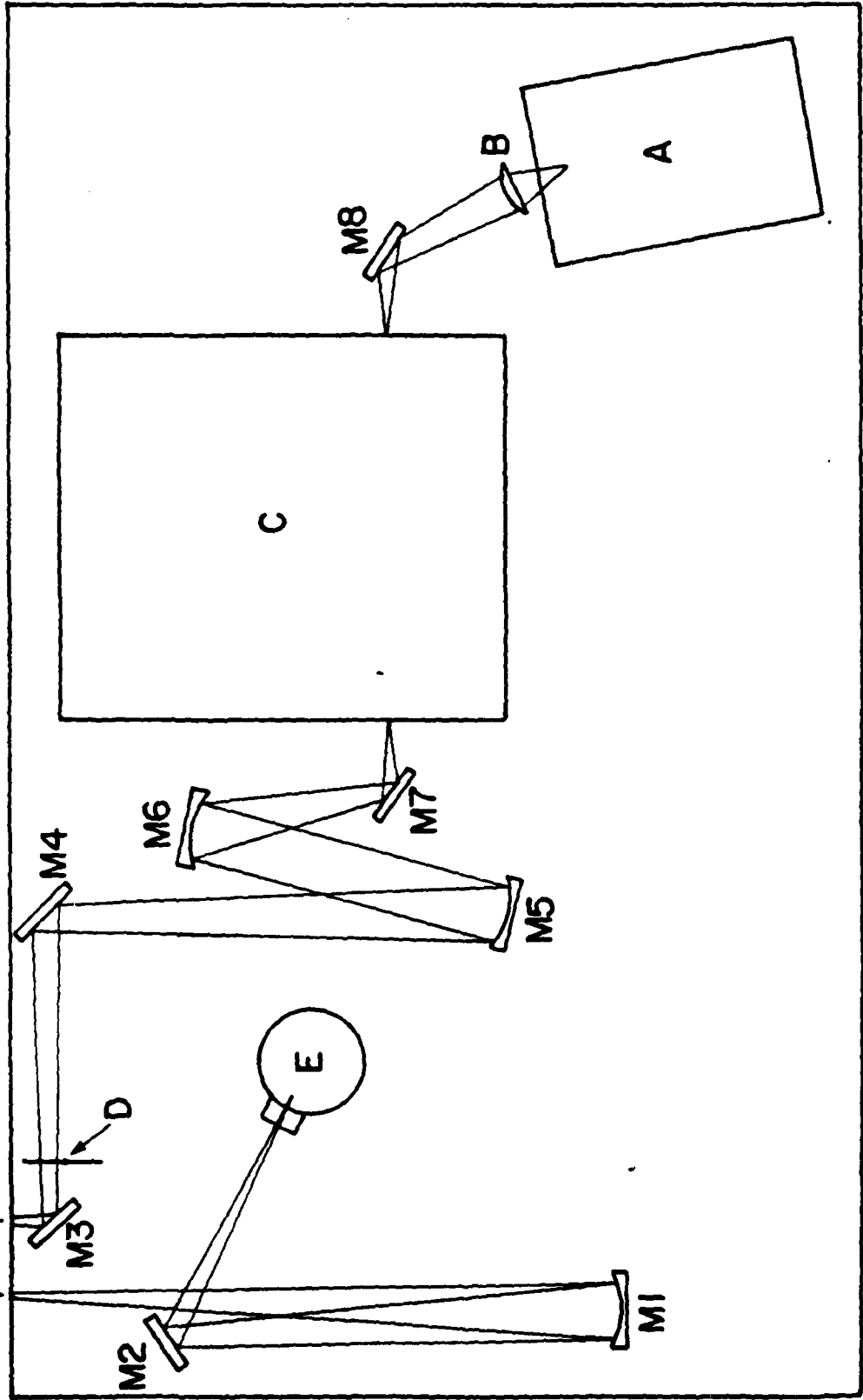


Figure 9

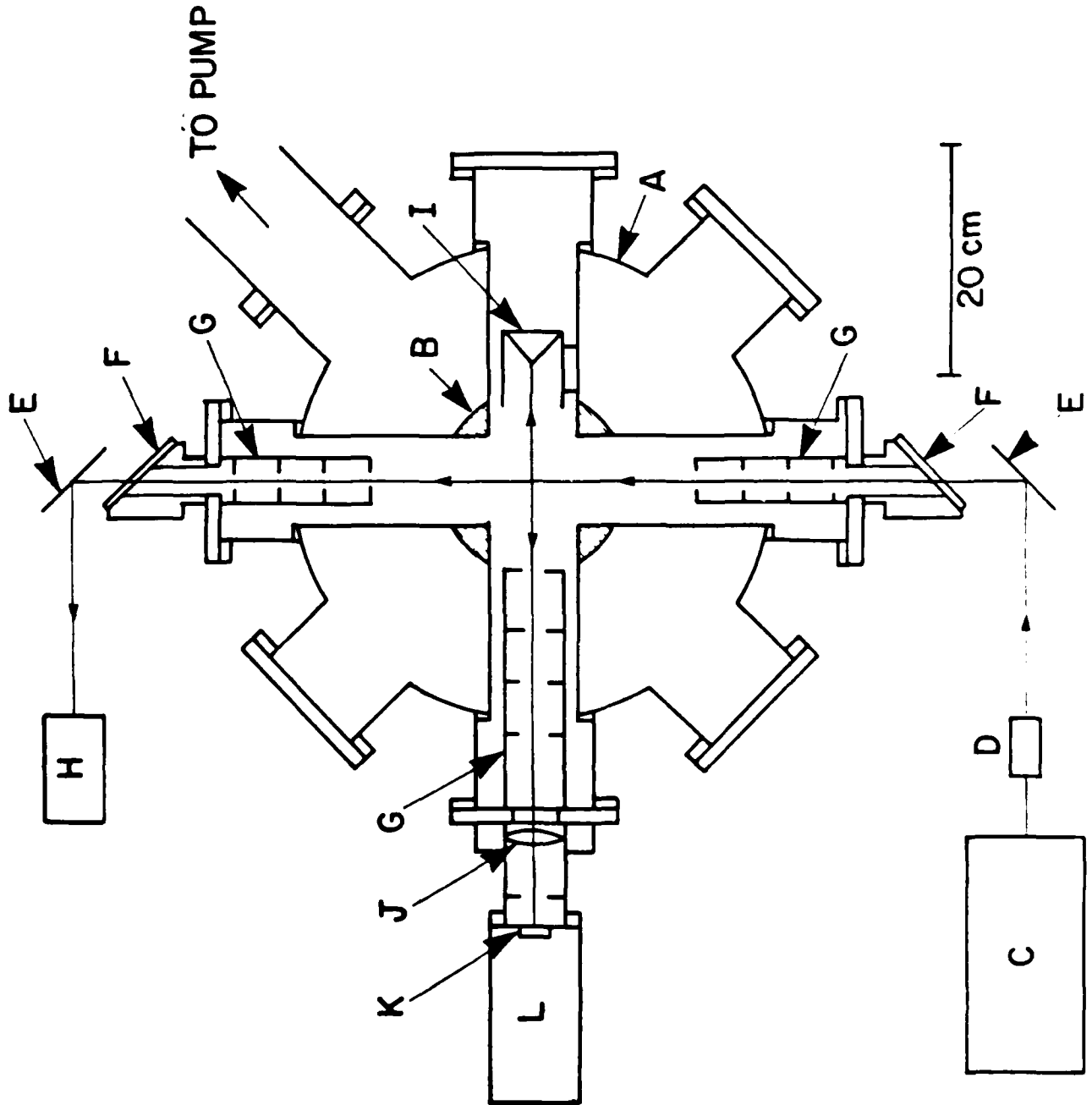


Figure 10

### 3. MEASURED AND PREDICTED BAND MODEL PARAMETERS OF $\text{BF}_3(\nu_3)$ AT HIGH TEMPERATURES

by

Michael E. Gersh and Lawrence S. Bernstein,  
and Lauren M. Peterson

#### ABSTRACT

Two experimental techniques were used to determine the high temperature infrared absorption coefficients of the  $\nu_3$  band of  $\text{BF}_3$ . A high temperature flow tube fitted with a multipass infrared absorption cell was used to determine the  $\text{BF}_3$  absorption coefficients at 298, 585, 870, 1150, and 1440 K.  $\text{BF}_3$  was also used in a flame emission-absorption apparatus to determine the  $\text{BF}_3$  absorption coefficients at 2400 K.

A generalized formulation for predicting the S/d and l/d band model parameters of symmetric top perpendicular bands of  $\text{MX}_3$  molecules is presented. The effect of including nuclear spin statistics in computing the S/d and l/d band model parameters is considered. It is shown that nuclear spin statistics effect only the l/d parameter and are significant only for the case of zero nuclear spin. A number of practical considerations which arise in designing a computer algorithm to calculate the S/d and l/d parameters, are discussed.

Comparisons of the theoretical and experimental  $\text{BF}_3$  absorption coefficients are made. Good agreement between theory and experiment at all temperatures was obtained by adjusting only two vibrational energy coupling constants,  $\chi_{23}$  and  $\chi_{34}$ . Predicted S/d and l/d band model parameters at 300, 600, 900, 1200, 1500, 2000, 2500, and 3000 K are presented.

## I. INTRODUCTION

For diatomic and linear triatomic molecules, theoretical predictions and experimental determinations of high temperature infrared absorption coefficients are in close agreement.<sup>1-13</sup> Our present knowledge of high temperature absorption coefficients for polyatomic molecules is less complete. As a first venture into high temperature polyatomic molecular spectroscopy we have performed a combined theoretical and experimental study of the  $\nu_3$  band of  $\text{BF}_3$ .

The vibrational and rotational constants of the ground and first excited vibrational states of  $\text{BF}_3$  have been experimentally determined by previous efforts.<sup>14-35</sup> In addition, the general theoretical description of fundamental vibrational-rotational band contours for symmetric top molecules is well established<sup>36-41</sup> and has been shown to adequately describe the room temperature infrared spectrum of  $\text{BF}_3$  at both low<sup>24,37</sup> and high spectral resolution.<sup>14,15,18,19,22</sup> This work provides the foundation for the present study.

Two complementary techniques were used for obtaining high temperature infrared absorption coefficients. These are: (1) absorption measurements in a high temperature flow reactor and (2) flame emission-absorption measurements. In the flow reactor, gaseous mixtures are conductively heated to temperatures up to 1500 K, and an aerodynamically confined flow is established which is intersected by a windowless multipass infrared absorption cell. In the flame studies,  $\text{BF}_3$  emission-absorption measurements were performed downstream of the burner exit. A temperature of 2400 K was attained in the flame measurements. The experimental data provide a complete picture of the temperature dependent band shape of the  $\nu_3$  band of  $\text{BF}_3$  from room temperature to 2400 K.

These data were used to validate a generalized band model for symmetric top perpendicular bands of  $MX_3$  molecules, which is applicable to both the planar and pyramidal geometries.

## II. GLOSSARY OF NOTATION

$A$	absorptivity
$A_e$	equilibrium rotational constant
$A_{JK}$	Honl-London intensity factor
$\langle A_v \rangle$	average rotational constant
$A_v$	rotational constant for $v$ 'th vibrational state
$B_e$	equilibrium rotational constant
$B_v$	rotational constant for $v$ 'th vibrational state
$\langle B_v \rangle$	average rotational constant
$c$	speed of light
$C_2$	second radiation constant
$D_J$	} centrifugal distortion constants
$D_{JK}$	
$D_K$	
$d_{\nu}^{P,R}$	line spacing for P, R-branch transitions
$d_{\nu}^Q$	line spacing for Q-branch transitions
$E(v, l, J, K)$	total vibration-rotation energy
$E_{\max}$	maximum allowed vibrational energy for computational convergence

$E'_v$	positive vibrational energy term for computational convergence
$\left. \begin{array}{l} \epsilon_{33} \\ \epsilon_{34} \\ \epsilon_{44} \end{array} \right\}$	vibrational angular momentum energy constants
$g_{vr}$	nuclear statistical weight for $vr$ 'th transition
$h$	Planck's constant
$I$	nuclear spin
$I_0, I$	unattenuated and attenuated photon beams respectively
$J$	rotational quantum number
$K$	rotational quantum number
$k$	Boltzman's constant
$k$	spectral absorption coefficient
$l$	physical absorption path length
$\left. \begin{array}{l} l_3 \\ l_4 \end{array} \right\}$	vibrational angular momentum quantum numbers
$L(\omega)$	spectral radiance
$m$	rotational quantum number
$n$	rotational quantum number
$P$	pressure

$S_0$	total integrated band strength
$S_3$	total integrated band strength for $\nu_3$ mode
$S_V^Q(\omega)$	integrated Q-branch line strength
$S_V^{P,R}(\omega)$	integrated P, R-branch line strength
$S/d(\omega)$	spectral absorption coefficient
$S_{vr}$	line strength of r'th transition
$\langle S/d \rangle$	band averaged absorption coefficient
$T$	temperature
$u$	optical path
$W_{BB}(\omega, T)$	Planck blackbody function
$Z_V$	} vibrational and rotational partition functions
$Z_R$	
$l/d(\omega)$	line density function
$\langle l/d \rangle$	band averaged line density including nuclear spin statistics
$\langle l/d \rangle'$	band averaged line density not including nuclear spin statistics

Greek Symbols

$\left. \begin{array}{l} \alpha_1^A, \alpha_1^B \\ \alpha_2^A, \alpha_2^B \\ \alpha_3^A, \alpha_3^B \\ \alpha_4^A, \alpha_4^B \end{array} \right\}$  vibration-rotation energy coupling terms

$\gamma$  spectral line width

$\left. \begin{array}{l} \xi_3 \\ \xi_4 \end{array} \right\}$  Coriolis coupling terms

$\nu$  with vibrational state

$\left. \begin{array}{l} \nu_1 \\ \nu_2 \\ \nu_3 \\ \nu_4 \end{array} \right\}$  vibrational quantum numbers for four modes of an  $MX_3$  symmetric top

$c$  rotational symmetry number

$\tau$  transmittance

$\left. \begin{array}{l} \lambda_{11}, \lambda_{22}, \\ \lambda_{33}, \lambda_{44}, \\ \lambda_{12}, \lambda_{13}, \\ \lambda_{14}, \lambda_{23}, \\ \lambda_{24}, \lambda_{34} \end{array} \right\}$  constants for quadratic vibrational energy terms

$\left. \begin{array}{l} \lambda_{111}, \lambda_{222}, \\ \lambda_{333}, \lambda_{444} \end{array} \right\}$  constants for cubic vibrational energy terms

$\omega$  wavenumber

$\left. \begin{array}{l} \omega_1, \omega_2, \\ \omega_3, \omega_4 \end{array} \right\}$  harmonic vibrational energy constants

$\omega_r$  P, R-branch transition energy

$\omega_n$  Q-branch transition energy

$\omega_v$  purely vibrational contribution to origin of  $\nu$ 'th band

$\omega_{vJ}$  origin of Q-branch for  $\nu$ 'th band

$\omega'_{vJ}$  modification of  $\omega_{vJ}$

$\omega_{vK}$  origin of P, R-branches for  $\nu$ 'th band

$\omega'_{vK}$  modification of  $\omega_{vK}$

$\Delta_{\nu, \nu'}$  difference of vibrational band center location between  $\nu'$  and  $\nu$ 'th bands

$\Delta\omega$  effective band width

### III. EXPERIMENTAL

The measurements were performed in two different types of apparatus. The first is a high temperature flow reactor into which the  $\text{BF}_3$  was introduced. This was used to measure the absorption spectra at temperatures between 298 K and 1440 K. The second is a radiative transfer apparatus that was used to measure the emission and absorption spectra of  $\text{BF}_3$  in a 2400 K flame.

#### A. High Temperature Flow Reactor

A cross sectional view of the Aerodyne Research, Inc. heated flow reactor is shown in Fig. 1. In general, the infrared active species of interest are produced by reaction in, or introduced into, a variable temperature flow reactor which can attain temperatures of 1500 K. Then, the flow is passed through an analysis region in which a multi-pass absorption cell (White Cell)<sup>42</sup> is mounted perpendicular to the flow direction. Finally, a portion of the flow is sampled by a molecular beam mass spectrometer before being exhausted to a large mechanical vacuum pump. In the present study the  $\text{BF}_3$  number density was obtained from total pressure, temperature and gas flow rates. For reactive species produced in the flow reactor, their number density can be measured in situ by the mass spectrometer or by laser-induced or resonance fluorescence (using mutually perpendicular optics tubes). Thus, one can obtain absolute values for the absorption coefficients without assuming that the reactive species in the flow tube have achieved local thermodynamic equilibrium. The detailed design of the flow reactor is discussed in Ref. 43.

The design of the gas flow system within the variable temperature flow reactor is fairly complicated due to the constraints imposed by the necessity of making infrared absorption measurements. The crucial element of the apparatus design is the configuration of the spectroscopic analysis region. In order for one to be able to perform quantitative absorption (or emission) measurements on the flow tube gases, three criteria must be satisfied: (1) the geometry of the absorbing gas flow must be well defined in the region where it traverses the White cell; (2) the flow in this region must be stable; and (3) the temperature distribution of the absorbing gas flow must be well defined (preferably, the gas should be isothermal). To satisfy these criteria, the flow of infrared active gas should ideally be confined in a cylindrical geometry and be located in a stable position, without any recirculation of absorbing gas into the optics tubes (i.e., the flow should behave as if it were confined by a cylindrical tube). For an ambient temperature flow with single-pass optics, one could simply place optical windows on the flow tube; however, the present and future experiments require high absorbing gas temperatures and a multi-pass absorption cell (for additional sensitivity). This necessitates the use of a wall-less confinement of the absorbing gases as they pass through the analysis region. This can only be accomplished by fluid dynamic confinement of the absorbing gas flow.

The analysis region design shown in Fig. 2 was considered to be most promising. The main flow containing argon carrier gas and  $\text{BF}_3$  is heated as it passes through two 2.5 cm thick mullite "honeycomb" hole arrays, and the outer, coaxial shield gas flow of argon is heated as it passes over the heater

elements. Then, the main and shield gas flows are both passed through concentric subsonic nozzles, after which they join and pass through the analysis region. The area ratio of the main flow nozzle to the shield flow nozzle is 2:1, and the corresponding flow rates are also designed to be in a 2:1 ratio so that the velocities of the two flows will be the same when they meet downstream of the nozzles. In addition, it was estimated that the flow of purge gas into the optics tubes should equal approximately 10 percent of the main flow and should be evenly divided between the four optics tubes.

This flow geometry is considerably more complicated than that used previously for flow reactors,<sup>44, 45</sup> and the design criteria for the confinement of the absorbing gas flow are quite strict. Thus, it was concluded that this crucial element of the flow system design should be tested in a flow simulation experiment.<sup>43</sup> The result of this experiment was that the main flow should be well confined for a Reynolds number of greater than approximately 100 in the main flow tube and with the flow rate ratios given above (main:shield:purge = 10:5:1).

The design of the present external optical system for the infrared absorption measurements is shown in Fig. 3. This double beam optical system has been designed for low spectral resolution measurements. The infrared radiation source is a Perkin-Elmer Corporation "Opperman Source" which is a mixed oxide tube heated by an internal coil of resistance wire. The radiation impinges on a mirror-bladed, 50 percent duty cycle chopping wheel which alternately allows it to pass into the White cell or reflects it, thereby bypassing the White cell. M2, M3, M4, M7 and M9 are flat mirrors; M1 and M8 are spherical mirrors, and M5 and M6 are off-axis paraboloid mirrors. The beam splitter is made of uncoated

zinc selenide, the monochromater is a Spex Minimate, and the detector is a Santa Barbara Research Corporation HgCdTe photoconductive detector, in front of which is placed an order-sorting (long-wavelength pass) filter.

In general, the data are acquired and analyzed in the following manner. At a given wavelength the double beam optical system is used to measure the difference in signal ( $I_0 - I$ ) due to the presence of  $\text{BF}_3$  in the gas flow. Then, the intensity of the single beam passing through the gas flow  $I_0$  is measured in the absence of  $\text{BF}_3$ . The ratio of these measurements is related to the spectral absorption coefficient  $k$  by Eq. (5).

$$(I_0 - I)/I_0 = 1 - \exp(-ku) \quad (1)$$

where  $k$  has the units  $\text{cm}^{-1} \text{ amagat}^{-1}$  and  $u$  is the optical path which is related to the physical absorption path length (cm) by

$$u = l (P/760)(273/T) \quad (2)$$

In this equation  $P(\text{torr})$  is the partial pressure of  $\text{BF}_3$ , and  $T(\text{K})$  is the temperature of the flowing gas. Thus, if  $l$ ,  $P$  and  $T$  are known, one can use the data to calculate the spectral absorption coefficient  $k$ .

The measurements were performed under the following conditions. The spectral scans covered the region from 6 to 8  $\mu\text{m}$ , with a spectral resolution of 0.02  $\mu\text{m}$ . The wavelength scale was calibrated by comparing a water vapor

absorption spectrum with the absorption peaks measured by Oetjen, et. al.<sup>46</sup>  
The temperatures, total pressures, densities of  $\text{BF}_3$ , and main flow Reynolds numbers are given in Table I. The number of White Cell passes was 52, with a nominal pathlength  $l = 4.8$  cm. Finally, the  $\text{BF}_3$  was obtained from Matheson and had a stated purity of 99.5 percent.

TABLE I. Experimental Conditions in Flow Reactor

Temperature (K)	Total Pressure (Torr)	BF <sub>3</sub> Density (Amagat)	Reynolds Number
298 ± 2	10.1	5.26 x 10 <sup>-5</sup>	530
585 ± 15	10.0	2.58 x 10 <sup>-5</sup>	315
870 ± 30	10.1	1.77 x 10 <sup>-5</sup>	238
1150 ± 100	50.5	3.06 x 10 <sup>-5</sup>	394
1440 ± 60	50.5	2.72 x 10 <sup>-5</sup>	339

## B. Flame Emission-Absorption Apparatus

The radiative transfer apparatus used at the Environmental Institute of Michigan to obtain IR flame spectra of  $\text{BF}_3$  is shown schematically in Fig. 4. It is a dual beam, ratio recording instrument utilizing a 0.27 m Perkin-Elmer Model 99G spectrometer. Both emission and absorption measurement can be made, and, since the emission measurements can be calibrated using the known radiance of the 1400 K blackbody source, absolute radiance measurements can be made in order to determine the temperature of the flame. The minimum resolution of the instrument was about  $2 \text{ cm}^{-1}$ , but the slits were usually opened to provide a resolution of about  $5 \text{ cm}^{-1}$ . Using a liquid nitrogen-cooled PbSnTe detector and an integration time of 0.3 sec, a signal-to-noise ratio of about 200 was obtained.

A seven segment 23 cm water-cooled multiple tube diffusion burner was used. Each segment was 3.3 cm long and had independent fuel ports. A segment consisted of a bundle of tubes through which the fuel was introduced to the flame and around which the oxidizer passed, such that the mixing region was formed at the upper surface of the tubes. By introducing  $\text{BF}_3$  into any of the central five segments, isothermal path lengths from 3.3 to 16.5 cm were obtained for the active species ( $\text{BF}_3$ ). It is worth noting that a non-isothermal condition exists between the shielding flame (end segments) and the ambient air, but, since there is no  $\text{BF}_3$  present, this is

of no consequence to the observed spectrum. Also, since the mole fraction of  $\text{BF}_3$  was typically only 0.06 in the active segments and since  $\text{BF}_3$  contributes only minimally in the combustion reaction to generate BOF, isothermal conditions were present at the active/shield flame interface.

The burner position was adjusted so that the beam of blackbody radiation was centered in the flame and was located at a height above the burner face which was above the visible reaction zone, but low enough so that the mixing layer with the ambient air had not penetrated a substantial distance into the burner plume. Heights of about 2 cm were used.

During a given spectral run, five complete spectral scans were performed in the following order:

1. An emission background scan with no active species ( $\text{BF}_3$ ) present in the flame
2. An absorption background scan with no active species.
3. An absorption scan with the active species present in the central segments (1, 3 or 5) of the 7-segment burner.
4. An emission scan with the active species present.
5. An absorption scan using the emission chopper.

The net absorption A was obtained by ratioing the transmissions  $\tau$ :

$$\tau_X = \frac{\tau_{BX}}{\tau_B} \quad (3)$$

$$A_X = 1 - \tau_X$$

where X denotes the species of interest, B denotes background, and BX denotes the combined spectrum due to active species plus background. In order to obtain absolute spectral radiance,  $L(\omega)$  values, the recorded data (voltage values) are compared to the reference radiance provided by the 1400 K blackbody. Flame temperatures were determined by dividing  $L_X(\omega)$  by  $A_X(\omega)$  and calculating the corresponding temperature for an equivalent blackbody,  $W_{BB}(\omega, T)$ .

$$L(\omega)/A_X(\omega) = W_{BB}(\omega, T) \quad (4)$$

As an independent check on the temperature determined by emission/absorption pyrometry,<sup>47</sup> the sodium D line reversal technique<sup>48</sup> was used. Both methods gave essentially identical temperatures for the  $BF_3$  measurements.

In order to quantify the IR emission and absorption measurements, it is necessary to know the density of active species present in the flame. Assuming the flame is in local thermodynamic equilibrium, chemical equilibrium calculations can provide an accurate determination of the quantity of reaction products. Given the flow conditions of the reactants and values for their heats of

formation, the flame temperature and the mole fraction of reaction products present in the flame may be calculated.<sup>49</sup> Unfortunately, this calculated value of the flame temperature is usually less reliable than experimentally determined temperatures, since the calculation is ideal and does not account for any loss mechanisms which may be present in the combustion process. For this reason, the flame temperature determined by emission/absorption pyrometry was used as an input condition to a chemical equilibrium program,<sup>49</sup> and the computed mole fractions of reaction products were used in calculating the absorption coefficients and band strengths for the  $\text{BF}_3$ . Once the temperature and composition of the flame are known quantitatively, the optical depth,  $u$ , may be determined in the same manner as discussed for the flow reactor (see Eq. (2)). The spectral absorption coefficient is determined from  $u$  and the measurement transmission,  $\tau$  (Eq. (3)), by

$$k = - \frac{\ln \tau}{u} \quad (5)$$

The mole fraction of  $\text{BF}_3$  in all the data runs was approximately 0.06. BOF and  $\text{BO}_2$  were also present in the flame, but their concentrations were approximately one and four orders of magnitude lower than that of  $\text{BF}_3$ , respectively. The computed equilibrium mole fractions of BOF and  $\text{BO}_2$  as a function of input  $\text{BF}_3$  mole fraction can be found in Fig. 5. Since BOF is

not expected to have any bands in this spectral region and since  $\text{BO}_2$  is so much more dilute than the  $\text{BF}_3$ , we may ascribe our measurements to be solely due to  $\text{BF}_3$ .

The emission/absorption pyrometry temperature measurements yielded the same temperature throughout the entire spectral band. This indicates a temporally stable and spatially isothermal active flame. Examination of the active flame with  $\text{BF}_3$  present revealed a light green plume over the majority of the active burner segments and a bright green intermediate zone between the active and shielding flame. The bright green flame is caused by  $\text{BO}_2$  emission and is an indication of a decreased amount of the reactant  $\text{BF}_3$  due to the combustion process. It is reasonable to assume that some of the  $\text{BF}_3$  is transported from the active region of the flame into the shield due to mixing at the active/shield flame interface, but the net absorption and emission of the flame should be the same if the active flame is isothermal and the total number density of  $\text{BF}_3$  remains unchanged. As is indicated by the optical temperature determination, the flame is indeed isothermal, but examination of the chemical equilibrium computations as a function of input  $\text{BF}_3$  concentration shows that the total number density of  $\text{BF}_3$  in the flame can change. As the input mole fraction of  $\text{BF}_3$  is decreased (i.e., by transport into the shield), the mole fraction of  $\text{BF}_3$  in the combustion products does not simply decrease in the same amount, but the reaction mixture in the shield/active flame mixing region is modified to drive more of the  $\text{BF}_3$  into the other boron compounds. This process should appear as a nonlinear deviation from Beer's law behavior because the decrease

in  $\text{BF}_3$  optical depth due to mixing is proportional to the concentration of  $\text{BF}_3$  in the active region. This nonlinearity was observed and corrected for by determining a smaller effective length of the active region. Subtracting 1 cm from all active burner lengths gave the desired linearity.

#### IV. THEORETICAL PREDICTIONS OF BAND MODEL PARAMETERS

In this section general equations for the S/d and l/d band model parameters are derived. The derivation (sections IV A-C) is for perpendicular bands of  $MX_3$  symmetric tops and applies to both the planar ( $D_{3h}$ ) and pyramidal ( $C_{3v}$ ) geometries. The effect of nuclear spin statistics on the calculation of the band model parameters is discussed in section IV D. In section IV E approximations to the general expression for the band model parameters are introduced which significantly decrease the computer time required to evaluate these quantities at high temperatures.

##### A. Average Line Spacing

The vibration-rotation energy of an  $MX_3$  symmetric top molecule is approximated by<sup>36</sup>

$$\begin{aligned}
 E(v, l, J, K) = & \omega_1(v_1 + 1/2) + \omega_2(v_2 + 1/2) + \omega_3(v_3 + 1) \\
 & + \omega_4(v_4 + 1) + x_{11}(v_1 + 1/2)^2 + x_{22}(v_2 + 1/2)^2 \\
 & + x_{33}(v_3 + 1)^2 + x_{44}(v_4 + 1)^2 \\
 & + x_{12}(v_1 + 1/2)(v_2 + 1/2) + x_{13}(v_1 + 1/2)(v_3 + 1) \\
 & + x_{14}(v_1 + 1/2)(v_4 + 1) + x_{23}(v_2 + 1/2)(v_3 + 1) \\
 & + x_{24}(v_2 + 1/2)(v_4 + 1) + x_{34}(v_3 + 1)(v_4 + 1) \\
 & + B_{33} l_3^2 + B_{34} l_3 l_4 + B_{44} l_4^2 + B_v J(J + 1) \\
 & + (A_v - B_v)K^2 - 2A_v(\zeta_3 l_3 K + \zeta_4 l_4 K) - D_J J^2(J + 1)^2 \\
 & + D_{JK} J(J + 1)K^2 - D_K K^4.
 \end{aligned} \tag{6}$$

The rotational constants in Eq. (6) are further defined by<sup>36</sup>

$$B_v = B_e - \alpha_1^B(v_1 + 1/2) - \alpha_2^B(v_2 + 1/2) - \alpha_3^B(v_3 + 1) - \alpha_4^B(v_4 + 1) \quad (7)$$

$$A_v = A_e - \alpha_1^A(v_1 + 1/2) - \alpha_2^A(v_2 + 1/2) - \alpha_3^A(v_3 + 1) - \alpha_4^A(v_4 + 1).$$

Absorption frequencies for Q-branch transitions as determined from the energy expression in Eq. (6) and the selection rules,<sup>36</sup>  $\Delta v_3 = 1$ ,  $\Delta J = 0$ ,  $|\Delta K| = \pm 1$ ,  $\Delta l_3 = \Delta K$ , are given by

$$\omega_n = \omega_{vJ} + 2 \left[ A_v(1 - \zeta_3) - B_v - D_{JK} J(J+1) \right] n + (\alpha_3^B - \alpha_3^A)n^2 - 4D_K n^3. \quad (8)$$

The quantities  $\omega_{vJ}$  and  $n$  in Eq. (8) are defined by

$$\omega_{vJ} = \omega_v - \alpha_3^B J(J+1)$$

$$\begin{aligned} \omega_v = & \omega_3 + 2\chi_{33}(v_3 + 3/2) + \chi_{13}(v_1 + 1/2) + \chi_{23}(v_2 + 1/2) \\ & + \chi_{34}(v_4 + 1) + g_{33}(2l_3 + 1) + g_{34}l_4 + A_v(1 - 2\zeta_3) - B_v \\ & - 2A_v [\zeta_3 l_3 + \zeta_4 l_4]. \end{aligned} \quad (9)$$

$$n = \begin{cases} +|K| \text{ for } \Delta|K| = +1 & \text{R-sub Q-branch} \\ -|K| \text{ for } \Delta|K| = -1 & \text{P-sub Q-branch} \end{cases}$$

As discussed previously,<sup>4</sup> Eq. (8) can be inverted so that the quantum label  $n$  can be expressed as a continuous function of the transition frequency,  $\omega$ . The cubic term  $4D_K n^3$  is a small perturbation even for large values of  $n$ . By first ignoring the cubic term, the resultant quadratic equation for  $n$  can be solved to yield

$$n = \frac{\left\{ \left[ A_V(1 - \zeta_3) - B_V - D_{JK} J(J+1) \right] \pm \sqrt{\left[ A_V(1 - \zeta_3) - B_V - D_{JK} J(J+1) \right]^2 - (\alpha_3^A - \alpha_3^B)(\omega - \omega_{vJ})} \right\}}{(\alpha_3^A - \alpha_3^B)}. \quad (10)$$

The cubic term can be introduced as a perturbation to the two roots for  $n$  in Eq. (10). This is accomplished by redefining  $\omega_{vJ}$  by

$$\omega'_{vJ} = \omega_{vJ} - 4D_K n^3 \quad (11)$$

where  $\omega'_{vJ}$  is substituted for  $\omega_{vJ}$  in Eq. (10). This process can be performed iteratively until converged values for the roots of  $n$  are determined. The root which is dropped by approximating Eq. (8) as a quadratic equation corresponds to the returning part of the P-sub Q-branch. Even at the highest temperatures of interest here (~3000 K) this root makes a negligible contribution to the calculated spectral absorption coefficients.

The average spacing of Q-branch transitions about a given transition is given by  $d_{\nu}^0(\omega) = (dn/d\omega)^{-1}$  which for  $n$  as defined in Eqs. (10) and (11) becomes

$$d_{\nu}^0(\omega) = 2 \left| \sqrt{\left[ A_{\nu}(1 - \zeta_3) - B_{\nu} - D_{JK}J(J+1) \right]^2 - (\alpha_3^A - \alpha_3^B)(\omega - \omega'_{\nu J})} \right. \\ \left. \pm 6D_K n^2 \right| \quad (12)$$

where the notation,  $\pm$ , corresponds to the  $\pm$  roots of  $n$  in Eq. (10).

The P, R-branch absorption frequencies as determined by the energy expression in Eq. (6) and the selection rules,<sup>36</sup>  $\Delta v_3 = 1$ ,  $\Delta J = \pm 1$ ,  $|\Delta K| = \pm 1$ ,  $\Delta l_3 = \Delta K$ , are given by

$$\omega_m = \omega_{\nu K} + 2 \left[ B_{\nu} - (\alpha_3^B/2) - D_{JK}n^2 \right] m \quad (13) \\ - (\alpha_3^B + 2D_{JK}n)m^2 - 4D_J m^3$$

where

$$\omega_{vK} = \omega_v + 2 \left[ A_v (1 - \zeta_3) - B_v \right] n + (\alpha_3^B - \alpha_3^A) n^2 - 4D_K n^3$$

$$m = \begin{cases} J + 1 & \text{R-branch} \\ -J & \text{P-branch} \end{cases} \quad (14)$$

When Eq. (13) is inverted to determine  $m$  as a function of  $\omega$  one obtains

$$m = \left\{ \left[ B_v - (\alpha_3^B/2) - D_{JK} n^2 \right] \right. \\ \left. \pm \sqrt{\left[ B_v - (\alpha_3^B/2) - D_{JK} n^2 \right]^2 - (\alpha_3^B + 2D_{JK} n)(\omega - \omega_{vK})} \right\} / \\ (\alpha_3^B + 2D_{JK} n) \quad (15)$$

and the cubic correction term

$$\omega'_{vK} = \omega_{vK} - 4D_J m^3 \quad (16)$$

The average spacing of P, R-branch lines is

$$d_{v}^{P,R}(\omega) = 2 \left| \sqrt{\left[ B_v - (\alpha_3^B/2) - D_{JK} n^2 \right]^2 - (\alpha_3^B + 2D_{JK} n)(\omega - \omega'_{vK})} \right. \\ \left. \pm 6D_J m^2 \right| \quad (17)$$

### B. Average Integrated Line Strength

The average integrated line strength for Q-branch transitions is given by<sup>36-38</sup>

$$S_V^Q(\omega) = S_3 \left[ (\nu_3 + 2)/2 \right] \exp \left[ -C_2 E(\nu, 1, J, K)/T \right] \quad (18)$$

$$\times A_{JK} (2J + 1) \omega \left[ 1 - \exp(-C_2 \omega/T) \right] / (4 \omega_{VJ}^2 Z_V Z_T)$$

In Eq. (18),  $S_V^Q(\omega)$  is expressed as a continuous function of the transition frequency,  $\omega$ , through its dependence on the continuous quantum number,  $n$ , defined in Eqs. (10) and (11). The quantity  $A_{JK}$  in Eq. (18) corresponds to the Honl-London intensity factors,<sup>36</sup> which are

$$A_{JK} = \frac{(J + 2 \pm |K|)(J + 1 \pm |K|)}{(J + 1)(2J + 1)} ; \quad \Delta J = +1 \quad \Delta |K| = \pm 1$$

$$A_{JK} = \frac{(J + 1 \pm |K|)(J \mp |K|)}{J(J + 1)} ; \quad \Delta J = 0 \quad \Delta |K| = \pm 1 \quad (19)$$

$$A_{JK} = \frac{(J - 1 \mp |K|)(J \mp |K|)}{J(2J + 1)} ; \quad \Delta J = -1 \quad \Delta |K| = \pm 1$$

where the  $A_{JK}$  are also continuous functions of  $\omega$  because of the expressions for J and K in Eqs. (15) and (10). The vibrational and rotational partition functions<sup>36, 50</sup> are computed from

$$z_v = \sum_{v_1} \sum_{v_2} \sum_{v_3} \sum_{l_3} \sum_{v_4} \sum_{l_4} \exp \left[ -C_2 E(, 1, 0, 0)/T \right] \quad (20)$$

$$z_r = \exp (C_2 B_v/T) \sqrt{\left(\frac{T}{C_2}\right)^3 \frac{\pi}{B_v^2 A_v}} \left[ 1 + \frac{1}{12} (C_2 B_v/T) (1 - B_v/A_v) \right. \\ \left. + \frac{3}{4} \left( T/(C_2 A_v) \right) \left( [D_J + D_{JK} + D_K] / A_v \right) + \frac{1}{2} \left( T/(C_2 A_v) \right) \left( D_{JK} / B_v \right) \right. \\ \left. + 2 \left( T/(C_2 B_v) \right) \left( D_J / B_v \right) + \left( T/(C_2 A_v) \right) \left( D_J / B_v \right) \right]$$

The expression for the integrated line strength for the P, R-branch lines,  $S_{\nu}^{P,R}$ , is almost identical to the Q-branch line strength formula in Eq. (18) except that  $\omega'_{vJ}$  is replaced by  $\omega'_{vK}$  of Eq. (16).

### C. Average Spectral Absorption Coefficient and Line Density

The average integrated line strength and line spacing determine an average absorption coefficient, which is expressed as<sup>1, 3, 4</sup>

$$\begin{aligned}
s/d(\omega) = \sum_{\nu} \left[ \sum_{J=|K|}^{J_{\max}} \left\{ s_{\nu}^{Q(+)} / d_{\nu}^{Q(+)} + s_{\nu}^{Q(-)} / d_{\nu}^{Q(-)} \right\} \right. \\
\left. + \sum_{K=-J}^J \left\{ \frac{P, R(+)}{S_{\nu}(\omega)} / d_{\nu}^{P, R(+)} + \frac{P, R(-)}{S_{\nu}(\omega)} / d_{\nu}^{P, R(-)} \right\} \right]
\end{aligned}
\tag{21}$$

where the sum over the index  $\nu$  implies the multiple summation over vibrational states in Eq. (20) and the (+) and (-) notation refers to the roots in Eqs. (10) and (15).

The average line density is calculated from the expression<sup>1, 3, 4</sup>

$$1/d(\omega) = \left( s^{1/2}/d(\omega) \right)^2 / (s/d(\omega))
\tag{22}$$

where

$$\begin{aligned}
s^{1/2}/d(\omega) = \sum_{\nu} \left[ \sum_{J=|K|}^{J_{\max}} \left\{ \left( s_{\nu}^{Q(+)} \right)^{1/2} / d_{\nu}^{Q(+)} + \left( s_{\nu}^{Q(-)} \right)^{1/2} / d_{\nu}^{Q(-)} \right\} \right. \\
\left. + \sum_{K=-J}^J \left\{ \left( \frac{P, R(+)}{S_{\nu}(\omega)} \right)^{1/2} / d_{\nu}^{P, R(+)} + \left( \frac{P, R(-)}{S_{\nu}(\omega)} \right)^{1/2} / d_{\nu}^{P, R(-)} \right\} \right].
\end{aligned}
\tag{23}$$

#### D. Effects of Nuclear Spin Statistics on Calculated Band Model Parameters

The theoretical expressions for the band model parameters  $S/d$  and  $1/d$  developed in the preceding sections neglect the effects that nuclear spin statistics can have on these quantities. An exact treatment of nuclear spin statistics would entail determining the overall symmetry species of every vibration-rotation line and then assigning the proper nuclear spin statistical weight to each line. As discussed in the following section, there are far too many allowed transitions for an  $\text{MX}_3$  molecule, like  $\text{BF}_3$ , for a line-by-line approach to be practical. It is possible, however, to estimate the average effects nuclear spin statistics have on calculated band model parameters. A band average value of the absorption coefficient can be determined from

$$\langle S/d \rangle = \frac{1}{\Delta\omega} \sum_{\nu} \sum_{r} \left[ \frac{g_{\nu r} c}{(2I + 1)^n} \right] S_{\nu r} \quad (24)$$

where  $\Delta\omega$  represents an effective width for the entire absorption band,  $\nu$  and  $r$  represent the vibrational and rotational quantum states, respectively,  $g_{\nu r}$  is the nuclear spin statistical weight<sup>36</sup> for the  $\nu, r$ 'th transition,  $c$  is the rotational symmetry number,<sup>36</sup>  $I$  is the nuclear spin<sup>36</sup> of the interchangeable identical atoms,  $n$  is the number of interchangeable identical atoms, and  $S_{\nu r}$  is the line strength for the  $\nu, r$ 'th line. It is important to realize that  $S_{\nu r}$  in Eq. (24) is defined neglecting nuclear spin weights entirely (not the

same as the case of  $I = 0$ ). For a fundamental band and its associated hot bands it is well known both theoretically and experimentally<sup>51</sup> that for harmonic oscillators the total integrated band strength is a constant, independent of temperature, and it can be shown that

$$\sum_v \sum_r S_{vr} = S_0 \quad (25)$$

$$\sum_v \sum_r \left[ \frac{g_{vr} \sigma}{(2I + 1)^n} \right] S_{vr} = S_0.$$

The implication of Eq. (25) is that on average,  $[(g_{vr}) / (2I + 1)^n] = 1$ . Essentially, ignoring nuclear spin has no effect on  $S/d(\omega)$ .

A band average line density can be written as

$$\langle 1/d \rangle = \frac{\sigma}{(2I + 1)^n} \left[ \sum_v \sum_r g_{vr}^{1/2} S_{vr}^{1/2} \right]^2 / (S_0 \Delta\omega). \quad (26)$$

The ratio of the line density including spin effects,  $\langle 1/d \rangle$ , to the density ignoring spin,  $\langle 1/d \rangle'$ , can be approximated by

$$\langle 1/d \rangle / \langle 1/d \rangle' = \frac{\sigma}{(2I + 1)^n} \frac{1}{m^2} \left[ \sum_{i=1}^m g_i^{1/2} \right]^2 \quad (27)$$

where  $m$  is the minimum number of  $\nu r$  states associated with the repeating pattern of nuclear statistical weights. Two simplifying assumptions were made in the derivation of Eq. (27) from Eq. (26). One assumption is that for a fixed vibrational band,  $\nu$ , the line strength is a slowly varying function of the rotational indices,  $r$ . The other assumption is that the majority of  $\nu$ ,  $r$  bands for a given molecule have the same repeating pattern of statistical weights. In general both these approximations are reasonable for polyatomic molecules at room temperature and above.

The effect of including nuclear spin statistics in the line density calculation for a number of common molecular geometries and spin types is shown in Table II. A general conclusion that can be drawn from Eq. (27) and Table II is that only nuclear spin types with  $I = 0$  will have line densities substantially different from the line density computed ignoring the effect of nuclear spin. In  $\text{BF}_3$ , ignoring nuclear spin statistics amounts to only a 3% error in the computed line densities.

#### E. Computational Considerations

A number of practical considerations arise in using a computer to evaluate the expressions for the absorption coefficient, Eq. (21), and the line density, Eq. (24). The major limitation to evaluation of these band model quantities as written involves the number of states that must be considered in the multiple summation over vibrational states and rotational states. For a  $\text{MX}_3$  molecule six vibrational sums are necessary ( $\nu_1, \nu_2, \nu_3,$

TABLE II. Effect of Nuclear Spin Statistics on Line Density for Common Molecular Geometries and Spin Types. (a)

Molecule	Symmetry Number ( $\sigma$ )	Identical Atoms (n)	Nuclear Spin (I)	Repetition Modulus (m)	Statistical Weights ( $g_1$ )	Line Density Ratio $\langle 1/d \rangle / \langle 1/d' \rangle$
$C^{16}O_2$	2	2	0	2	0, 1	1/2
$N_2O$	1	0	-	1	1	1
$H_2O$	2	2	1/2	2	1, 3	0.93
$D_2O$	2	2	1	2	3, 6	0.97
$BF_3$	6	3	1/2	3	1, 1, 2 <sup>(b)</sup>	0.97
$S^{16}O_3$	6	3	0	3	0, 0, 1/2 <sup>(c)</sup>	1/3
$S^{16}O_3$	6	3	0	3	1/4, 1/4, 0 <sup>(d)</sup>	2/3

(a) values for  $\sigma$ , I, and  $g_1$  taken from Ref. (36).

(b) same pattern for nondegenerate and degenerate vibrational states

(c) nondegenerate vibrational states

(d) degenerate vibrational states

$l_3, v_4, l_4$ ) as well as additional sums over the J and K rotational quantum numbers for the Q-branch and P, R-branches respectively. The number of states that must be included to insure convergence of the calculated band model parameters will scale approximately as  $(v_{\max})^6 J_{\max}$ . For  $\text{BF}_3$  at high temperatures (~3000K) we estimate that at least  $\sim 10^8$  quantum states contribute significantly to the band model parameters. An additional multiplicative factor of  $\sim 10^2$  must also be included since the band model parameters are evaluated over a frequency grid,  $\omega$ , with a grid spacing comparable to the spacing between lines in a vibration-rotation band. Thus, approximately  $10^{10}$  separate evaluations of the expressions for  $S_v(\omega)$  (Eq. (18)) and  $d_v(\omega)$  (Eqs. (12) and (17)) are required for  $\text{BF}_3$  at high temperatures. Although it is certainly possible to perform  $10^{10}$  evaluations of  $S_v(\omega)$  and  $d_v(\omega)$  on some of the larger, faster computers we were interested in a computer program which could run quickly on the PRIME 400 minicomputer at Aerodyne Research. A simple approximation was adopted which, for the  $\text{BF}_3$  case, reduced the number of evaluations of  $S_v(\omega)$  and  $d_v(\omega)$  from  $\sim 10^{10}$  to  $\sim 10^4$ . That is, we assumed that all the hot bands in the  $\Delta v_3 = 1$  sequence have the same normalized band shape. Therefore, once the absolute band shape is known for a single band in the sequence, all other band shapes can be calculated by scaling to the appropriate integrated band strength and shifting the band shape to the appropriate band origin. The reference band shape is calculated from vibrationally average rotational constants. These average quantities are determined by

$$\langle A_v \rangle = \sum_v A_v \exp(-C_2 E(v, 0, 0)/T) / Z_v \quad (28)$$

where an analogous expression can be written for  $\langle B_v \rangle$ . The line strength of an arbitrary state,  $S_{v'}(\omega)$ , is related to the reference line strength,  $S_v(\omega)$ , by

$$\begin{aligned} S_{v'}(\omega) = & S_v(\omega - \Delta\omega_{v',v}) \left[ (v_3' + 1) / (v_3 + 1) \right] \left( \exp[-C_2 E(v', 0, 0)/T] / \right. \\ & \left. \exp[-C_2 E(v, 0, 0)/T] \right) \left( \omega / [\omega - \Delta\omega_{v',v}] \right) \\ & \times \left( \omega_v / [\omega_v + \Delta\omega_{v',v}] \right) \left( 1 - \exp[-C_2 \omega/T] \right) / \\ & \left( 1 - \exp[-C_2(\omega - \Delta\omega_{v',v})/T] \right) \end{aligned} \quad (29)$$

where  $\Delta\omega_{v',v} = \omega_{v'} - \omega_v$ . The line spacings are related by

$$d_{v'}(\omega) = d_v(\omega - \omega_{v',v}). \quad (30)$$

In a previous paper<sup>4</sup> on linear triatomic band model parameters several factors affecting convergence were discussed. Essentially, the same comments apply here. That is, the choice of upper limits to the vibrational sums should be subject to the restriction that only vibrational states whose energy,  $E(v_1, v_2, v_3, l_3, v_4, l_4, 0, 0)$ , is less than an energy cutoff,  $E_{\max}$ , should be considered. The choice of  $E_{\max}$  depends on temperature, where the rule of thumb given previously was

$$C_2 E_{\max}/T = 10. \quad (31)$$

Also, additional terms, constrained to be positive, were added to the vibrational energy terms in Eq. (6), and have the form

$$E'_v = \chi_{111}(v_1 + 1/2)^3 + \chi_{222}(v_2 + 1/2)^3 + \chi_{333}(v_3 + 1)^3 \\ + \chi_{444}(v_4 + 1)^3. \quad (32)$$

The values for the  $\chi_{ijk}$ 's are determined such that the first derivative of the vibrational energy with quantum number is always equal or greater than zero for the maximum quantum numbers considered at a given temperature (see Eq. (24) of the earlier paper<sup>4</sup> for a prescription to compute the  $\chi_{ijk}$ 's).

## V. RESULTS AND DISCUSSION

Comparisons of theoretical predictions and experimental determination of the absorption coefficients of the  $\nu_3$  band of  $\text{BF}_3$  at 298, 585, 870, 1150, 1440, and 2400 K are presented in Figs. 6-11. The  $\text{BF}_3$  vibrational and rotational molecular constants used to generate the theoretical predictions are found in Table III. Most of the  $\text{BF}_3$  molecular constants were determined experimentally from high resolution room temperature spectral measurements. Those molecular constants not obtainable from room temperature data have been estimated by Ginn et. al.,<sup>20</sup> who considered the effect of anharmonic potential energy terms in the  $\text{BF}_3$  intramolecular potential energy function in the prediction of these constants. For the  $\nu_3$  vibrational mode the molecular constants which are not determined from low temperature spectral measurements are  $\chi_{13}$ ,  $\chi_{23}$ ,  $\chi_{33}$ ,  $\chi_{34}$ ,  $g_{33}$ , and  $g_{34}$ . At room temperature 85% of the  $\text{BF}_3$  molecules are in the ground vibrational state, and most of the remaining 15% are in the  $\nu_4 = 1$  level. The maximum displacement of the  $\nu_3$  hot bands associated with the doubly degenerate  $\nu_4 = 1$  level is at most  $-7 \text{ cm}^{-1} (\chi_{34} + g_{34})$  which, given the much smaller intensity of this band compared to the  $\nu_3$  fundamental, means that the perturbation this has on the bandshape is relatively small and therefore difficult to measure accurately. In order to more accurately determine these molecular constants it is necessary to perform high temperature spectral measurements where the hot band transitions are sufficiently intense relative to the rotational envelope of the fundamental band. The sensitivity of the predicted  $\nu_3$  band contour at 2400 K to changes in the molecular constants  $\chi_{23}$  and  $\chi_{34}$  is shown in Fig. 11.

TABLE III.  $^{11}\text{BF}_3$  Molecular Constants<sup>20, 22, 36</sup> used in Band Model Calculations.

Molecular Constant <sup>(a)</sup>	Value ( $\text{cm}^{-1}$ )	Molecular Constant	Value ( $\text{cm}^{-1}$ )
$\omega_1$	940.	$A_e$	0.17635
$\omega_2$	699.	$B_e$	0.3527
$\omega_3^{(b)}$	1486.5	$A_{a_1}$	$4 \times 10^{-4}$
$\omega_4$	481.	$A_{a_2}$	$-3 \times 10^{-4}$
$\chi_{11}$	-0.99	$A_{a_3}$	$7.5 \times 10^{-4}$
$\chi_{22}$	1.31	$A_{a_4}$	$1 \times 10^{-4}$
$\chi_{33}$	-12.28	$B_{a_1}$	$8 \times 10^{-4}$
$\chi_{44}$	0.39	$B_{a_2}$	$-1.5 \times 10^{-4}$
$\chi_{12}$	-3.23	$B_{a_3}$	$1.5 \times 10^{-3}$
$\chi_{13}$	-4.10	$B_{a_4}$	$-4.7 \times 10^{-3}$
$\chi_{14}$	-8.12	$\zeta_3$	0.795
$\chi_{23}$	-11.0	$\zeta_4$	-0.811
$\chi_{24}$	0.92	$D_J$	$4.1 \times 10^{-7}$
$\chi_{34}$	2.0	$D_{JK}$	$-6.7 \times 10^{-7}$
$B_{33}$	9.66	$D_K$	$2.7 \times 10^{-7}$
$B_{34}$	4.67		
$B_{44}$	-0.20		

(a) Observed fundamentals corrected for anharmonicity ( $\chi_{ij}$ ) to give harmonic frequencies  $\omega_1$ ,  $\omega_2$ ,  $\omega_3$ , and  $\omega_4$ .

(b) For  $^{10}\text{BF}_3$   $\omega_3 = 1537.5 \text{ cm}^{-1}$ . The  $^{11}\text{B}/^{10}\text{B}$  isotope ratio used in the calculations was 4.10.

Initial estimates of  $\chi_{23} = -2.11$  and  $\chi_{34} = 3.8 \text{ cm}^{-1}$  were used (see curve "A" of Fig. 11) which were the values predicted by Ginn et. al.,<sup>20</sup> who included the effect of anharmonicity in the  $\text{BF}_3$  intramolecular potential energy surface on the prediction of vibrational and rotational molecular constants. By adjusting these constants to  $\chi_{23} = -11$  and  $\chi_{34} = 2 \text{ cm}^{-1}$ , a good fit to the flame spectra at 2400 K was attained. Since it is clear that the high temperature data can be fit well with only two parameters,  $\chi_{23}$ , and  $\chi_{34}$ , it is not possible to simultaneously determine  $\chi_{13}$ ,  $\chi_{33}$ ,  $\epsilon_{33}$ , and  $\epsilon_{34}$ . The assumed values of  $\chi_{13}$ ,  $\chi_{33}$ ,  $\epsilon_{33}$ ,  $\epsilon_{34}$ , were those predicted by Ginn et. al.<sup>20</sup> One expects that  $\chi_{23}$  and  $\chi_{34}$  will have the greatest influence on the high temperature bandshape because  $\nu_4$  and  $\nu_2$  are the lowest energy modes in  $\text{BF}_3$ . At temperatures below 1500 K (flow tube data) the predicted contours were much less sensitive to variations in  $\chi_{23}$  and  $\chi_{34}$ ; although the set of constants determined by fitting the 2400 K data did produce a significantly better fit than the initial estimates.

There are two areas of disagreement between the data and the theoretical predictions for the temperatures below 2400K. The first of these is the fact that the data in the center of the band is generally higher than the predictions and the experimental widths of the band are slightly narrower than the predictions at 585, 870, 1150, and 1440K. In addition, for all of the flow reactor data it was not possible to obtain a consistent value for the band strength. The band strengths derived from the data ranged from 3100 to 5900  $\text{cm}^{-2} \text{ amagat}^{-1}$ . At a given temperature, the band strength measured on different days showed a similar variability. However, the measured band shapes, normalized to a common band strength, were repeatable. Both of these disagreements apparently arise from the same problem - the recirculation of infrared active species in the

White cell optics tubes. The observed effects could be caused by relatively little recirculation since the optical path through the recirculating gases is much longer than that through the main flow and due to the relatively long residence time of species in a recirculating flow.

It can be seen from Table I that the flow reactor was always operated at Reynolds numbers which should be high enough, as indicated by the flow simulation experiment, to preclude recirculation of infrared active species in the optics tubes. In addition, a check experiment was conducted at 870K in which the Reynolds number was doubled, with no resulting significant change in the measured absorption. This seems to indicate that the recirculation is not due to operation of the flow reactor at a "marginal" Reynolds number. However, in the flow simulation experiment the shield flow was observed to recirculate.<sup>43</sup> Thus, it is likely that the recirculation may be due to diffusion of infrared active species into the shield flow. This phenomenon was not observed in the flow simulation experiment because the residence time of a volume of fluid in the analysis region scales linearly with the Reynolds number, but the diffusion length scales as the square root of the residence time. Therefore, for a given Reynolds number the diffusion length in the gas will be greater than the diffusion length in the flow simulation experiment.

For future experiments the nozzle on the end of the main flow tube will have its inside diameter reduced from 4.9 cm to 4.2 cm. This will reduce the ratio of main nozzle area to (concentric) shield nozzle area from 2:1 to

approximately 1:1 (with a concurrent increase in the shield flow). This increase in the width of the shield flow in the analysis region should eliminate the recirculation of infrared active species from the main flow in the optics tubes.

The integrated band strength of the  $\nu_3$  band of  $\text{BF}_3$  has been previously determined by McKean<sup>23</sup> at room temperature to be  $3290 \pm 300 \text{ cm}^{-2} \text{ amagat}^{-1}$ . This can be compared to the 2400K value determined by the flame measurements of  $2800 \pm 230 \text{ cm}^{-2} \text{ amagat}^{-1}$ . It has been shown by Breeze et. al.,<sup>51</sup> that in the harmonic oscillator approximation the integrated band strength is independent of temperature. However, Crawford, and Dinsmore<sup>52</sup> have demonstrated that when the effects of mechanical and electrical anharmonicity are considered, the bandstrength is no longer temperature independent. The band model formulation used in the theoretical predictions of the  $\text{BF}_3$  band contours partially includes the effect of mechanical anharmonicity by using the vibrational anharmonic molecular constants in the evaluation of the vibrational partition function and excited state populations. Using an input value of  $3290 \text{ cm}^{-2} \text{ amagat}^{-1}$  for the room temperature bandstrength the model predicts bandstrengths of  $3170 \text{ cm}^{-2} \text{ amagat}^{-1}$  at 1500 K and  $2940 \text{ cm}^{-2} \text{ amagat}^{-1}$  at 2500 K. This suggests that the difference in the experimental bandstrength determinations may be real and can be explained by the effects of mechanical and electrical anharmonicity on the temperature dependence of integrated bandstrengths.

A complete set of theoretical predictions for the S/d and l/d band model parameters at 300, 600, 900, 1500, 2000, 2500, and 3000 K can be found in

Figs. 12-17. The extremely large line densities above 600 K preclude the experimental determination of the  $l/d$  parameter because  $\gamma(l/d) \gg 1$ , where  $\gamma$  is the linewidth of a single transition, even when  $\gamma$  is Doppler limited. At room temperature and below,  $l/d$  is measureable at low pressure (Doppler limit). An attempt to measure  $l/d$  at room temperature was made; however, the results were inconclusive due to the recirculation problem discussed above.

#### ACKNOWLEDGEMENTS

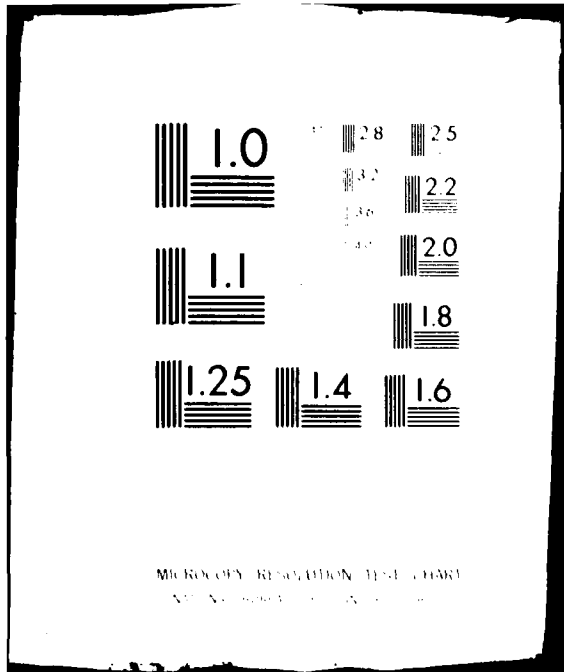
We wish to thank R. Brown for his major role in the construction of the flow reactor and in his assistance in obtaining the data and J. Moore for his dedicated work in obtaining the burner spectra. We also wish to acknowledge valuable discussions with C. Kolb, M. Camac, F. Kaufman, H. Wolfhard, S. Zakanycz, F. Simmons, G. Lindquist, and C. Arnold.

The work at ARI was supported by the Air Force Office of Scientific Research under Contract F49620-77-C-0075. The work at ERIM was sponsored by the Defense Advanced Research Projects Agency and monitored by MICON.

#### REFERENCES

1. C.B. Ludwig, W. Malkmus, J.E. Reardon, and J.A.L. Thomson, "Handbook of Infrared Radiation from Combustion Gases," NASA SP-3080, (Scientific and Technical Information Office, Washington, D.C., 1973).
2. S.S. Penner, R.C. Sepucha, and J.E. Lowder, J. Quant. Spectrosc. Radiat. Trans. 10, 1001 (1970).
3. W. Malkmus, J. Opt. Soc. Am. 53, 951 (1963).
4. L.S. Bernstein, J. Quant. Spectrosc. Radiat. Trans. 23, 157 (1980).
5. L.S. Bernstein, D.C. Robertson, and J.A. Conant, J. Quant. Spectrosc. Radiat. Trans. 23, 169 (1980).
6. W.M. Elsasser, Phys. Rev. 54, 126 (1938).
7. G.N. Plass, J. Opt. Soc. Am. 48, 690 (1958).
8. C.C. Ferisso, C.B. Ludwig, and L. Acton, J. Opt. Soc. Am. 56, 171 (1966).
9. Y. Ben-Aryeh, Appl. Opt. 6, 1049 (1967).
10. W.O. Davies, J. Opt. Soc. Am. 54, 467 (1964).
11. U.P. Openheim and Y. Ben-Aryeh, J. Opt. Soc. Am. 53, 344 (1963).
12. T. Kunitomo and M. Osumi, J. Quant. Spectrosc. Radiat. Trans. 15, 345 (1975).
13. L.D. Gray, Appl. Opt. 4, 1494 (1965).
14. S.G.W. Ginn, J.K. Kenney, and J. Overend, J. Chem. Phys. 48, 1571 (1968).
15. S.G.W. Ginn, C.W. Brown, J.K. Kenney, and J. Overend, J. Mol. Spectry. 28, 509 (1968).
16. C.W. Brown and J. Overend, Can. J. Phys. 46, 977 (1968).
- 17.. C.W. Brown and J. Overend, Spectrochim. Acta 25A, 1535 (1969).
18. S.N. Dreska and K.N. Rao, J. Mol. Spectry. 18, 404 (1965).
19. S.G.W. Ginn, D. Johansen, and J. Overend, J. Mol. Spectry. 36, 448 (1970).
20. S.G.W. Ginn, S. Reichman, and J. Overend, Spectrochim. Acta 26A 291 (1970).
21. J.L. Duncan, J. Mol. Spectry. 13, 338 (1964).





22. J.L. Duncan, J. Mol. Spectry. 22, 247 (1967).
23. D.C. McKean, J. Chem. Phys. 24, 1002 (1956).
24. I.W. Levin and S. Abramowitz, J. Chem. Phys. 43, 4213 (1965).
25. D.T. Hawkins, L.S. Bernstein, W.E. Falconer, and W. Klemperer, "Binary Fluorides: Free Molecular Structures and Force Fields, A Bibliography (1957 - 1975)." (Plenum Pub. Corp., New York, N.Y., 1976).
26. C.R. Bailey, J.B. Hale, and J.W. Thompson, J. Chem. Phys. 5, 274 (1937).
27. C.R. Bailey, J.B. Hale, and J.W. Thompson, Proc. Roy. Soc. A 161, 107 (1937).
28. P.A. Freedman and W.J. Jones, J. Mol. Spectrosc. 54, 182 (1975).
29. D.M. Gage and E.F. Barker, J. Chem. Phys. 7, 455 (1939).
30. S. Konaka, Y. Murata, K. Kuchitsu, and Y. Morino, Bull. Chem. Soc. Jap. 39, 1134 (1966).
31. K. Kuchitsu and S. Kinaka, J. Chem. Phys. 45, 4342 (1966).
32. F.N. Masri, J. Mol. Spectrosc. 43, 168 (1972).
33. G.M. Sheldrick, J. Mol. Spectrosc. 20, 295 (1966).
34. J. Vanderryn, J. Chem. Phys. 30, 331 (1959).
35. D.M. Yost, D. Devault, T.F. Anderson, and E.N. Lassette, J. Chem. Phys. 6, 424 (1938).
36. G. Herzberg, "Infrared and Raman Spectra," (Van Nostrand Reinhold, New York, 1945).
37. W.F. Edgell and R.E. Moynihan, J. Chem. Phys. 45, 1205 (1966).
38. S.L. Gerhard and D.M. Dennison, Phys. Rev. 43, 197 (1933).
39. R.M. Badger and L.R. Zumwalt, J. Chem. Phys. 6, 711 (1938).
40. D.M. Dennison, Phys. Rev. 28, 318 (1926).
41. G. Placzek and E. Teller, Z. Physik 81, 209 (1933).

42. T.H. Edwards, J. Opt. Soc. Am. 51, 98 (1961).
43. M.E. Gersh and C.E. Kolb, In "Characterization of High Temperature Vapors and Gases" (Edited by J.W. Hastie), NBS Special Publication 561 (1979). p. 679.
44. A. Fontijn, S.C. Kurzius, J.J. Houghton, and J.A. Emerson, Rev. Sci. Instr. 43, 726 (1972).
45. E.E. Ferguson, F.C. Fehsenfeld, and A. Schmeltekopf, Adv. At. Mol. Phys. 5, 1 (1969).
46. R.A. Oetjen, C. Kao, and H.M. Randall, Rev. Sci. Instr. 13, 515 (1942).
47. F.S. Simmons, "Spectroscopic Pyrometry of Gases, Flames and Plasmas," ISA Transactions, 2, (1963), p. 168.
48. A.G. Gaydon and H.G. Wolfhard, "Flames, Their Structure, Radiation and Temperature," (Chapman and Hall, Ltd., London, 1969), 2nd Edition.
49. S. Gordon and B.J. McBride, Report No. NASA-SP-273 (National Aeronautics and Space Administration, Washington, D.C., 1971).
50. The terms involving the centrifugal distortion constants were derived using the formulation in N. Davidson, "Statistical Mechanics" (McGraw-Hill Co., New York, 1962), p. 172.
51. J.C. Breeze, C.C. Ferriso, C.B. Ludwig, and W. Malkmus, J. Quant. Spectrosc. Radiat. Trans. 402 (1965).
52. B.L. Crawford and H.L. Dinsmore, J. Chem. Phys. 18, 983 (1950).

## Figure Captions

1. Cross-sectional view of the Aerodyne Research, Inc., heated flow reactor. Shield gas flow (A), main gas flow (B), 7.3 cm alumina flow tube (C), water cooled vacuum jacket (D), refractory insulation (E), six-arm cross to support flow tubes (F), entry and exit points of infrared radiation (G), gas flow to pumps (H), mass spectrometer sampling orifice (I), exhaust port to pump (J), white cell mirror (1 of 2) (K), optics tube purging gas flow (1 of 4) (L), Kanthal heating elements (M), and multihole mullite heater array (N).
2. Cross-sectional view of flow reactor analysis region. Main flow (A), purge flow (B), mass spectrometer sampling orifice (C), six-arm support cross (D), and refractory insulation (E).
3. External optics of flow reactor. Flat mirrors (M2, M3, M4, M7, M9), spherical mirrors (M1, M8), off-axis paraboloid mirrors (M5, M6), HgCdTe detector, and Spex Minimate monochromator.
4. Optical schematic of Environmental Research Institute of Michigan double beam emission-absorption spectrometer. Shutters (B1 - B4), choppers (C1, C2), blackbody (BB), spectrometer (SP), detector (D), CaF<sub>2</sub> windows (W), and grating (G).
5. Equilibrium calculations of boron species combustion products for BF<sub>3</sub> flame measurements at 2400 K.
6. Comparison of theoretical and experimental (flow tube) determinations of the BF<sub>3</sub>  $\nu_3$  band absorption coefficients at 298K.
7. Comparison of theoretical and experimental (flow tube) determinations of the BF<sub>3</sub>  $\nu_3$  band absorption coefficients at 585K.
8. Comparison of theoretical and experimental (flow tube) determinations of the BF<sub>3</sub>  $\nu_3$  band absorption coefficients at 870K.
9. Comparison of theoretical and experimental (flow tube) determinations of the BF<sub>3</sub>  $\nu_3$  band absorption coefficients at 1150K.
10. Comparison of theoretical and experimental (flow tube) determinations of the BF<sub>3</sub>  $\nu_3$  band absorption coefficients at 1440K.
11. Comparison of theoretical and experimental (flame) determinations of the BF<sub>3</sub>  $\nu_3$  band absorption coefficients at 2400K. Initial estimates<sup>20</sup> of  $\chi_{23} = -2.11$  and  $\chi_{34} = 3.8 \text{ cm}^{-1}$  (A) and adjusted values of  $\chi_{23} = -11$  and  $\chi_{34} = 2. \text{ cm}^{-1}$  (B).

12. Theoretical prediction of the  $\text{BF}_3 \nu_3$  band absorption coefficients at 300 and 600K.
13. Theoretical prediction of the  $\text{BF}_3 \nu_3$  band absorption coefficients at 900, 1200, and 1500K.
14. Theoretical prediction of the  $\text{BF}_3 \nu_3$  band absorption coefficients at 2000, 2500, and 3000K.
15. Theoretical prediction of the  $\text{BF}_3 \nu_3$  band line density parameter,  $1/d$ , at 300 and 600K.
16. Theoretical prediction of the  $\text{BF}_3 \nu_3$  band line density parameter,  $1/d$ , at 900, 1200, and 1500K.
17. Theoretical prediction of the  $\text{BF}_3 \nu_3$  band line density parameter,  $1/d$ , at 2000, 2500, and 3000K.

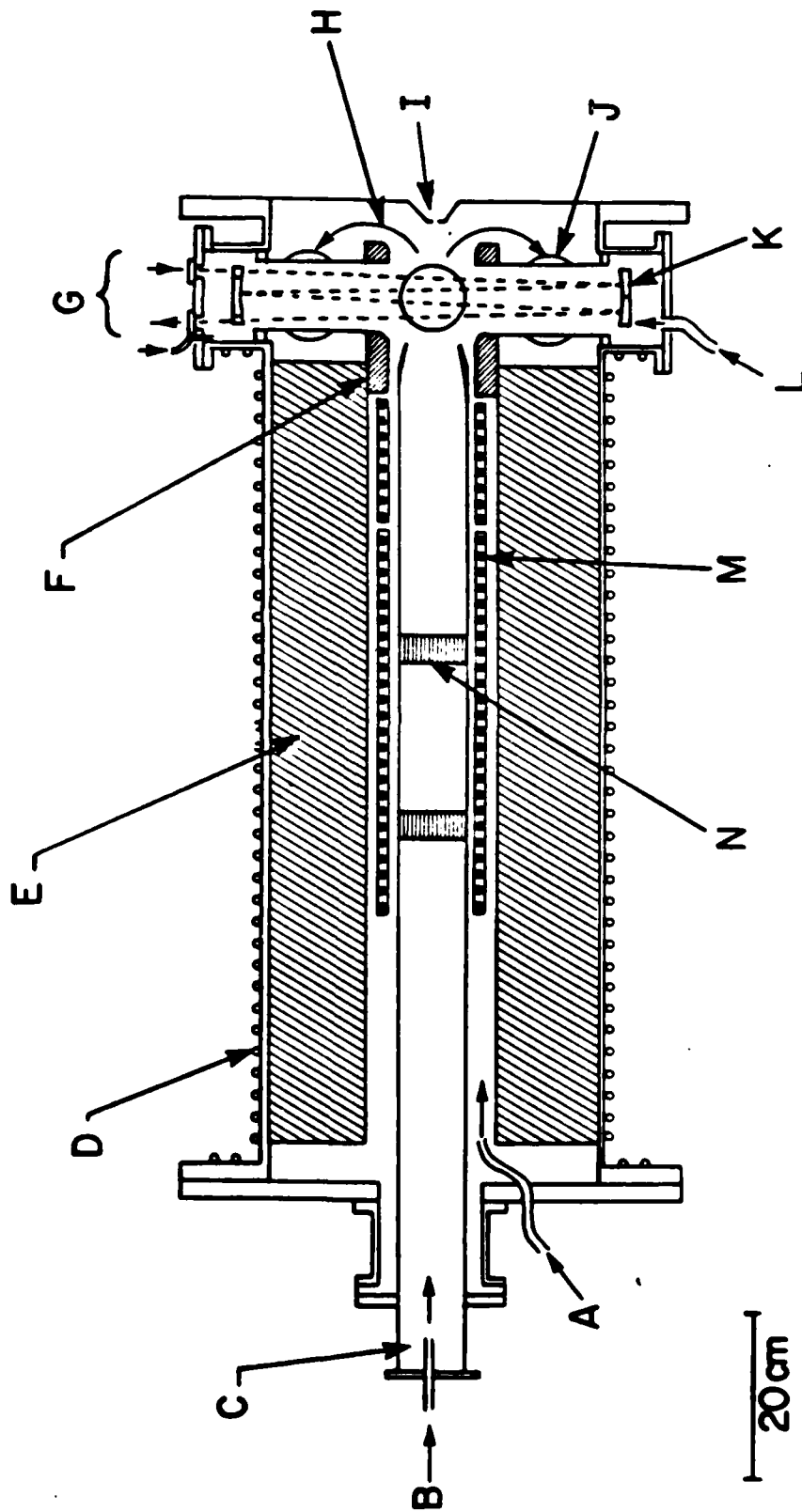


Figure 1

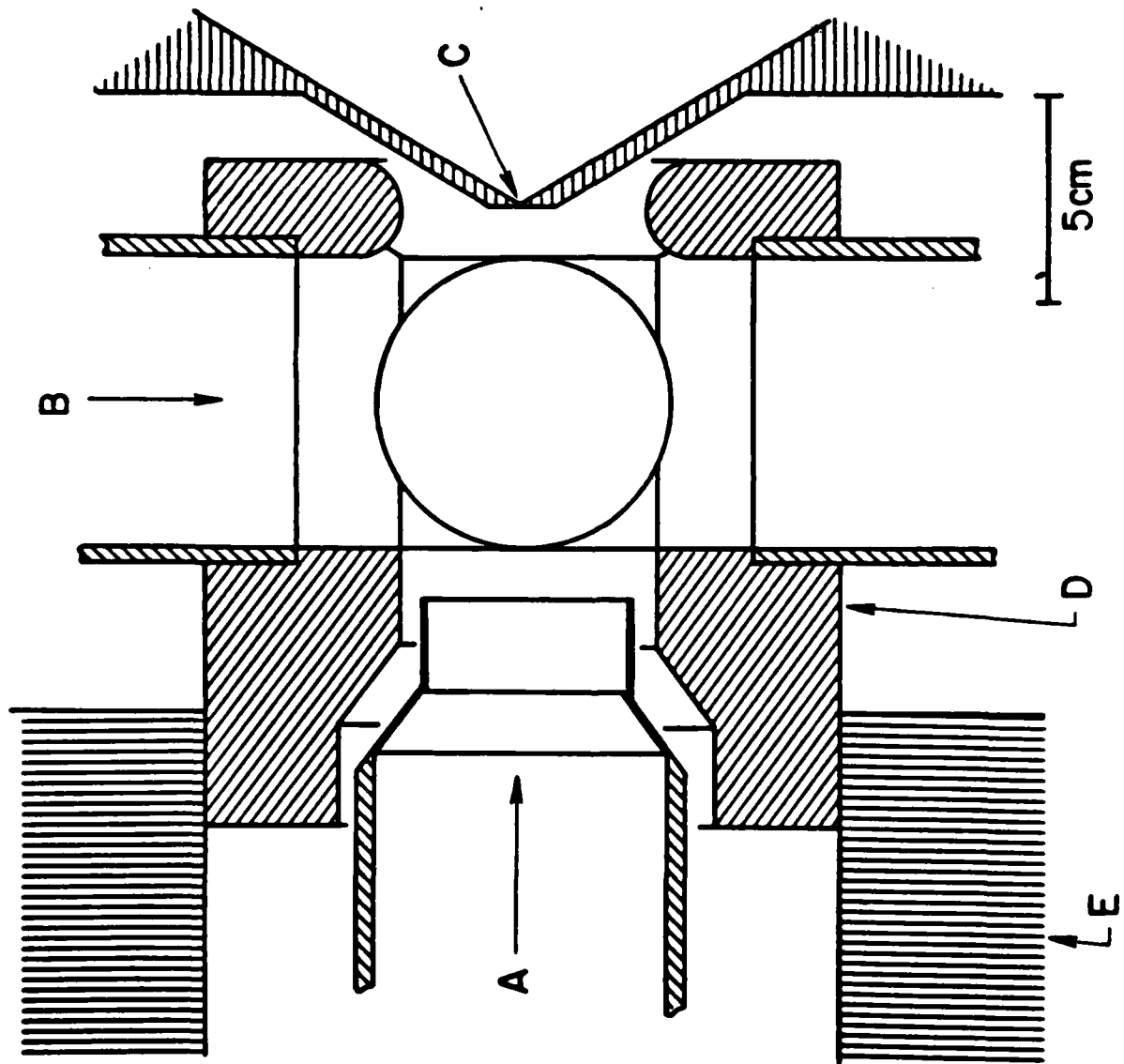


Figure 2

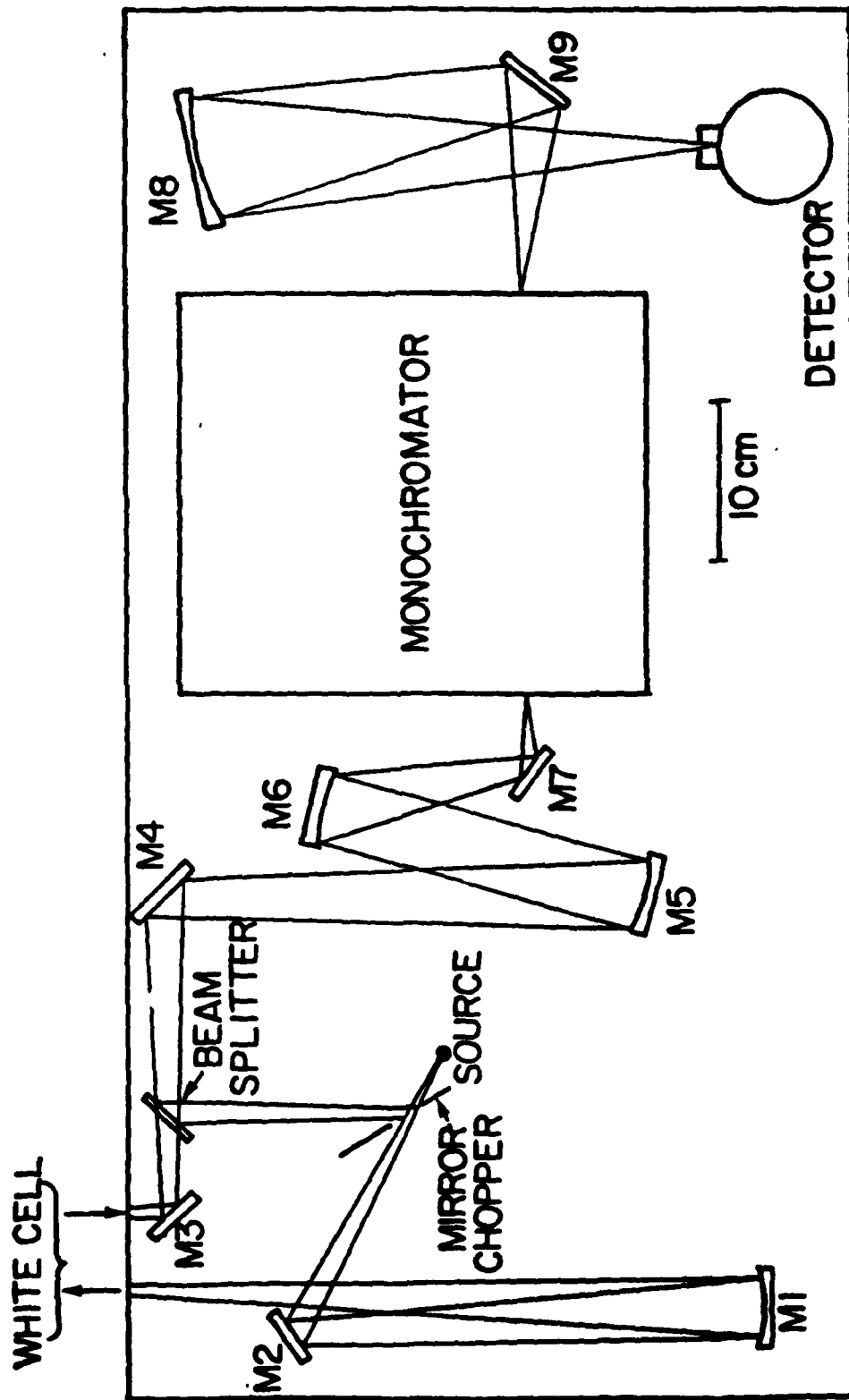


Figure 3

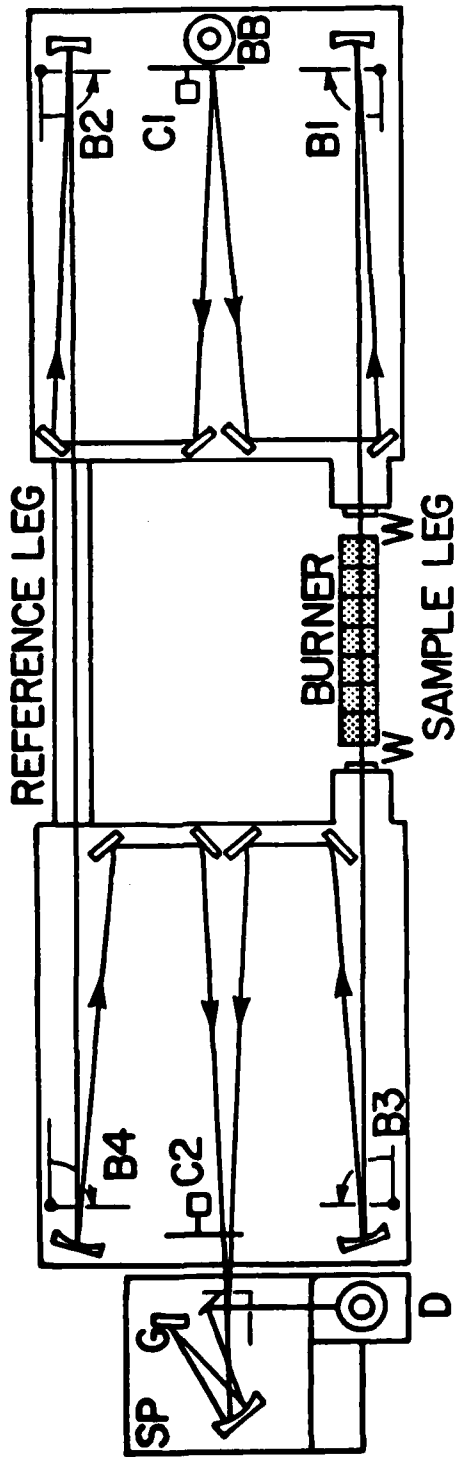


Figure 4

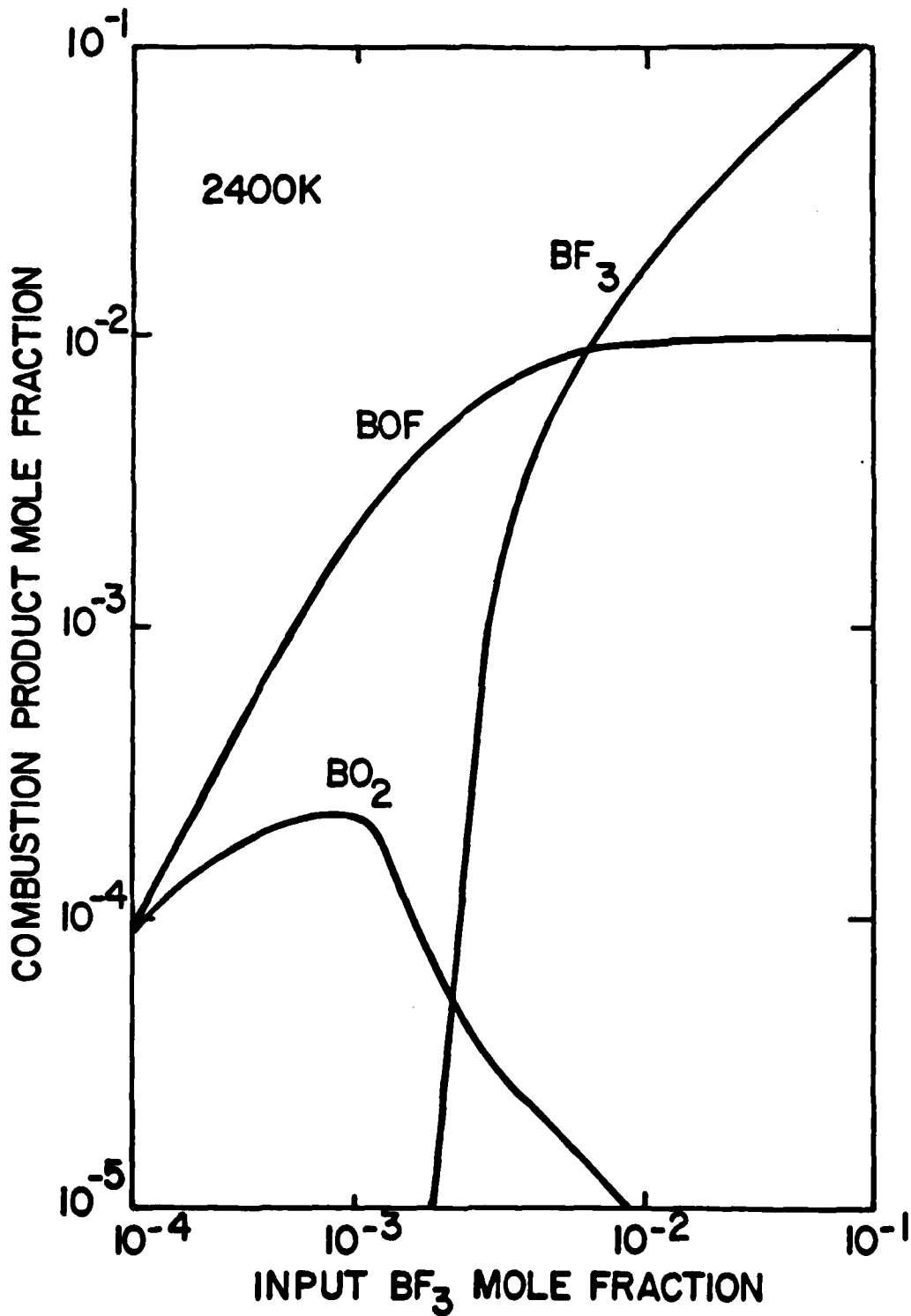


Figure 5

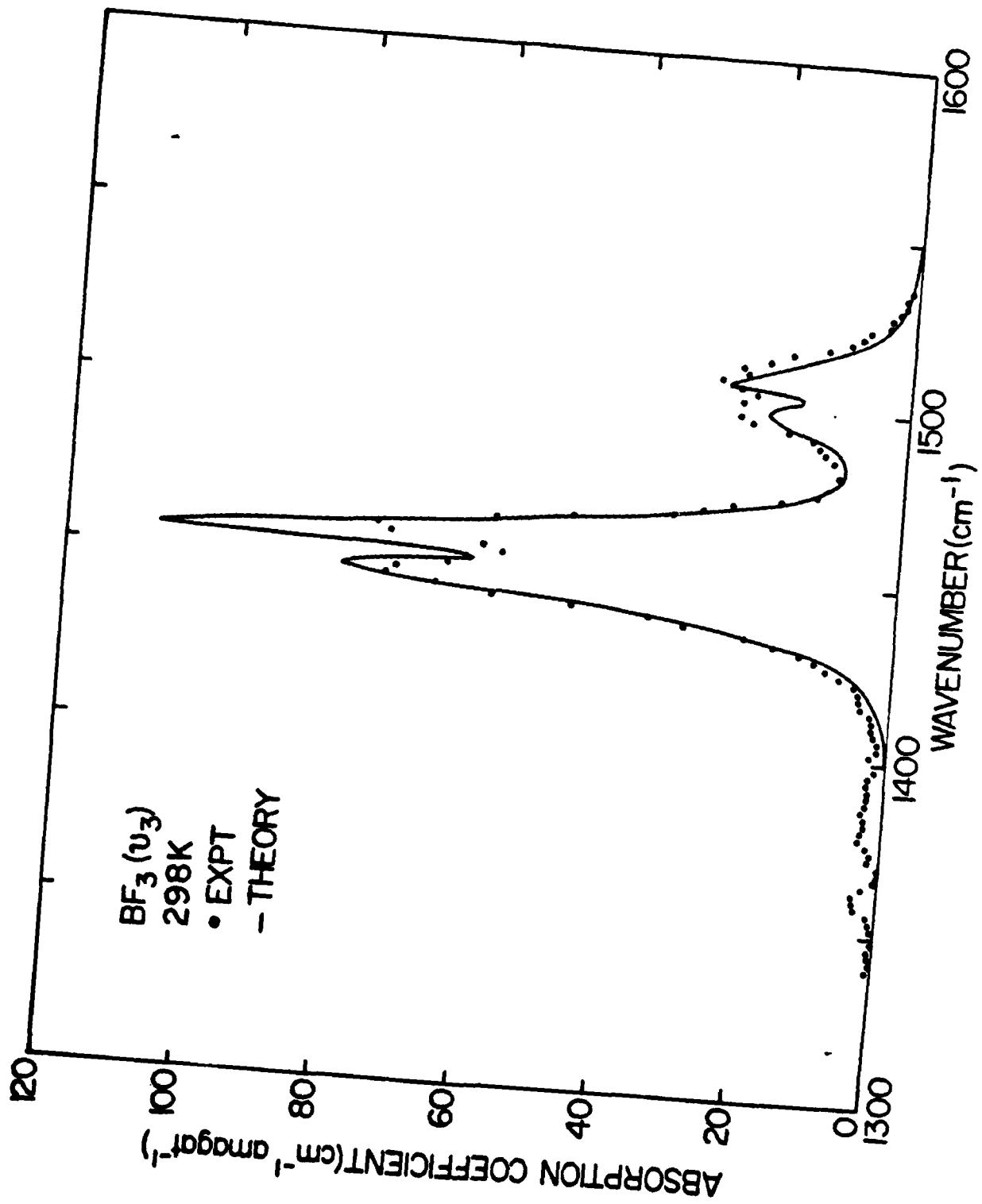


Figure 6

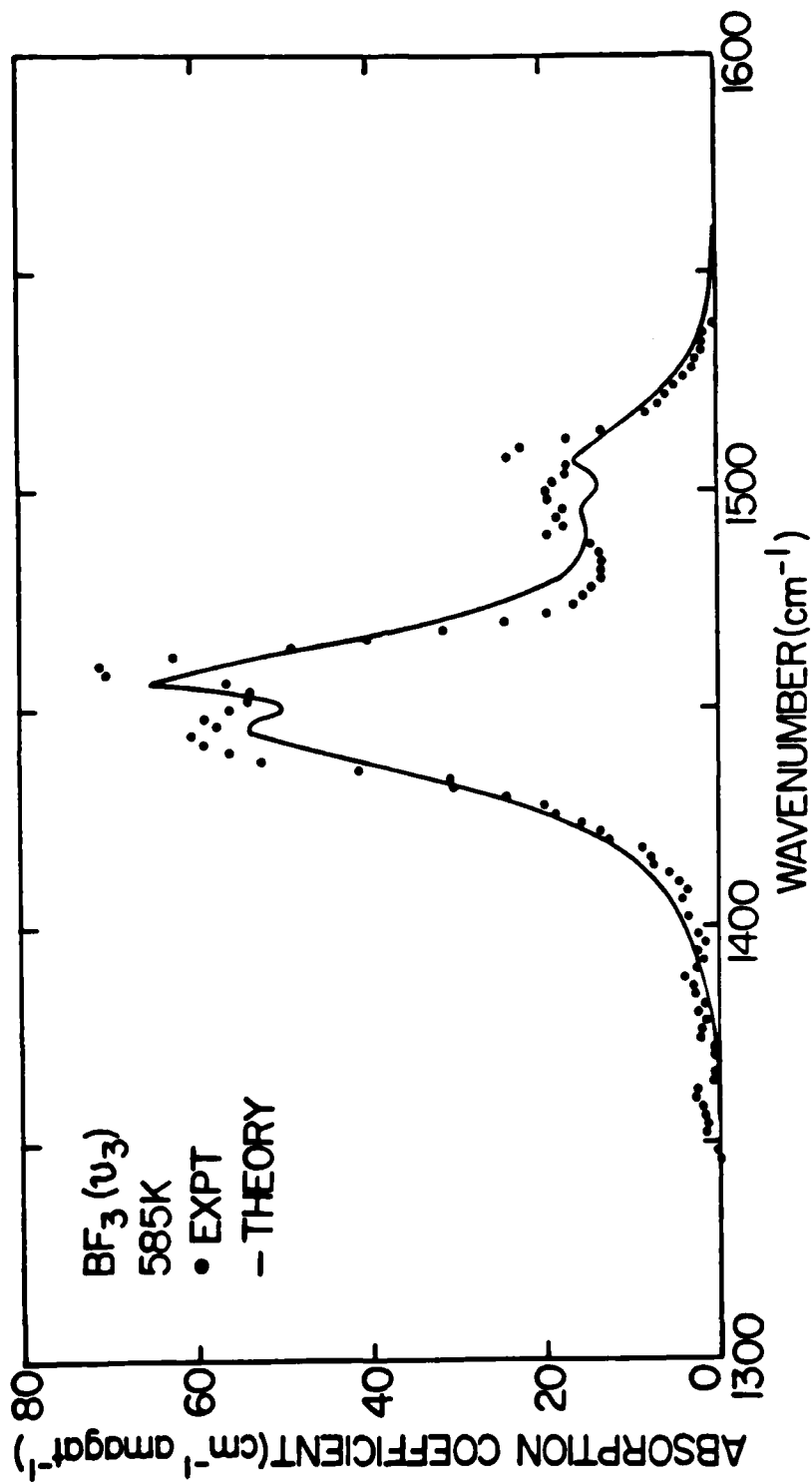


Figure 7

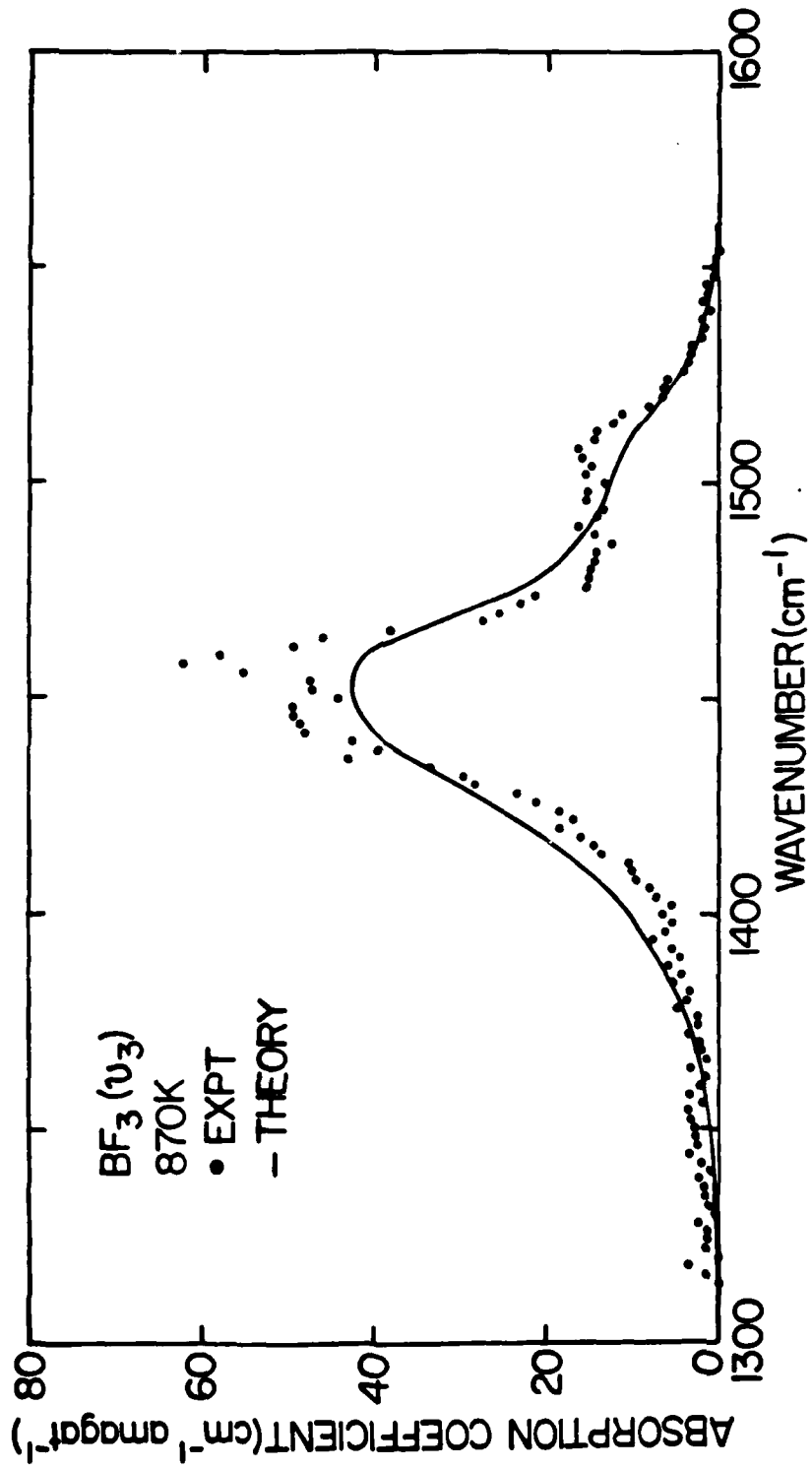


Figure 8

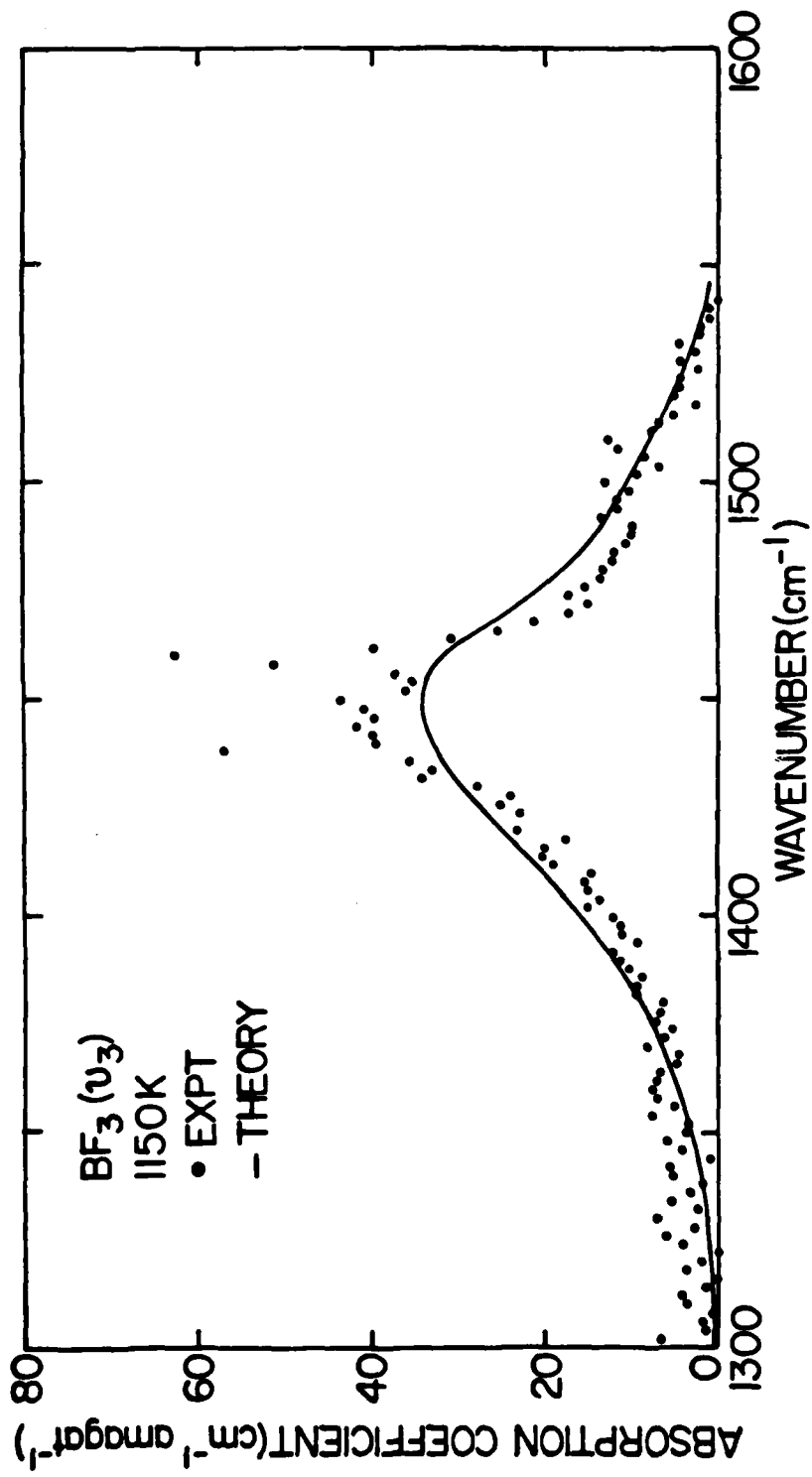


Figure 9

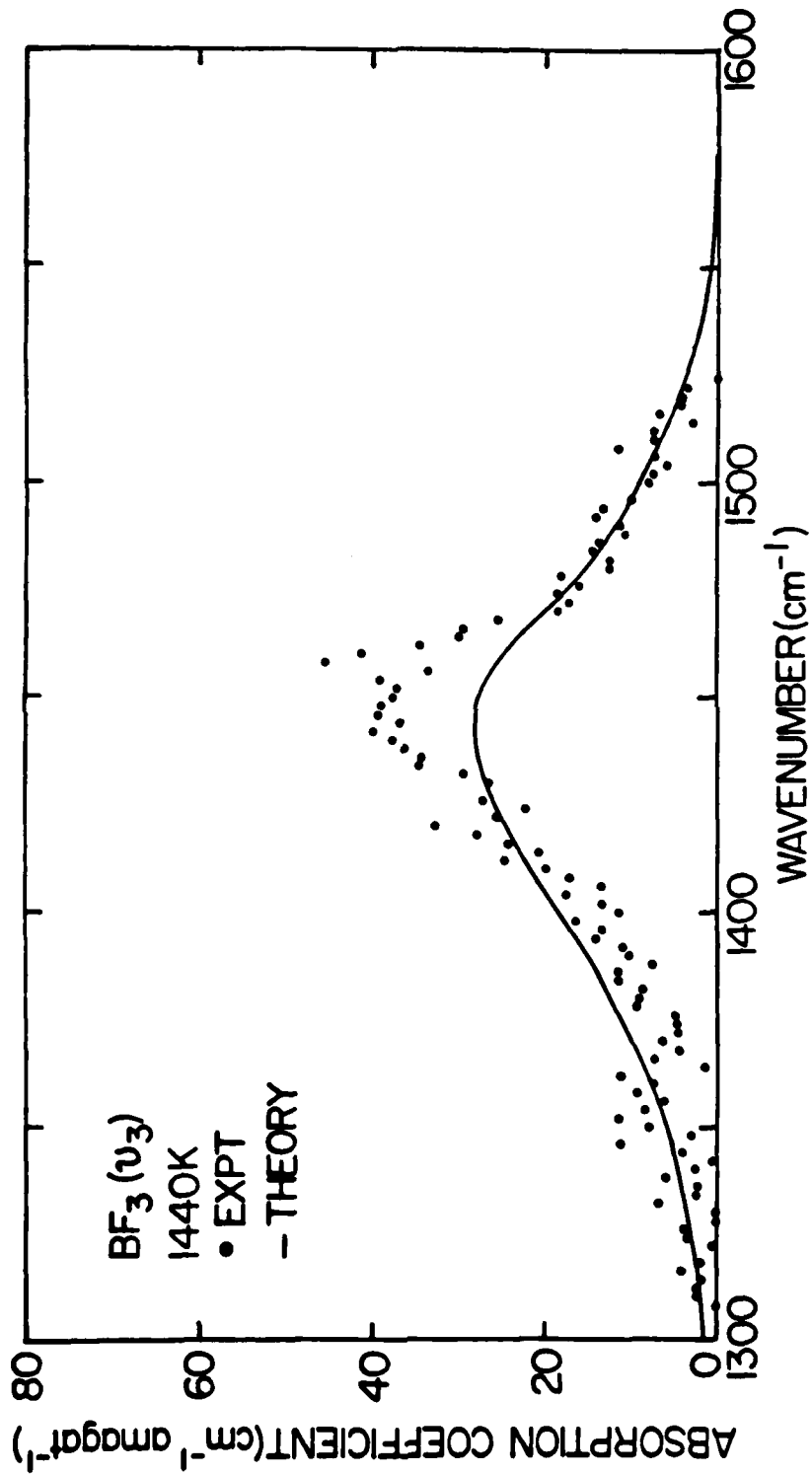


Figure 10

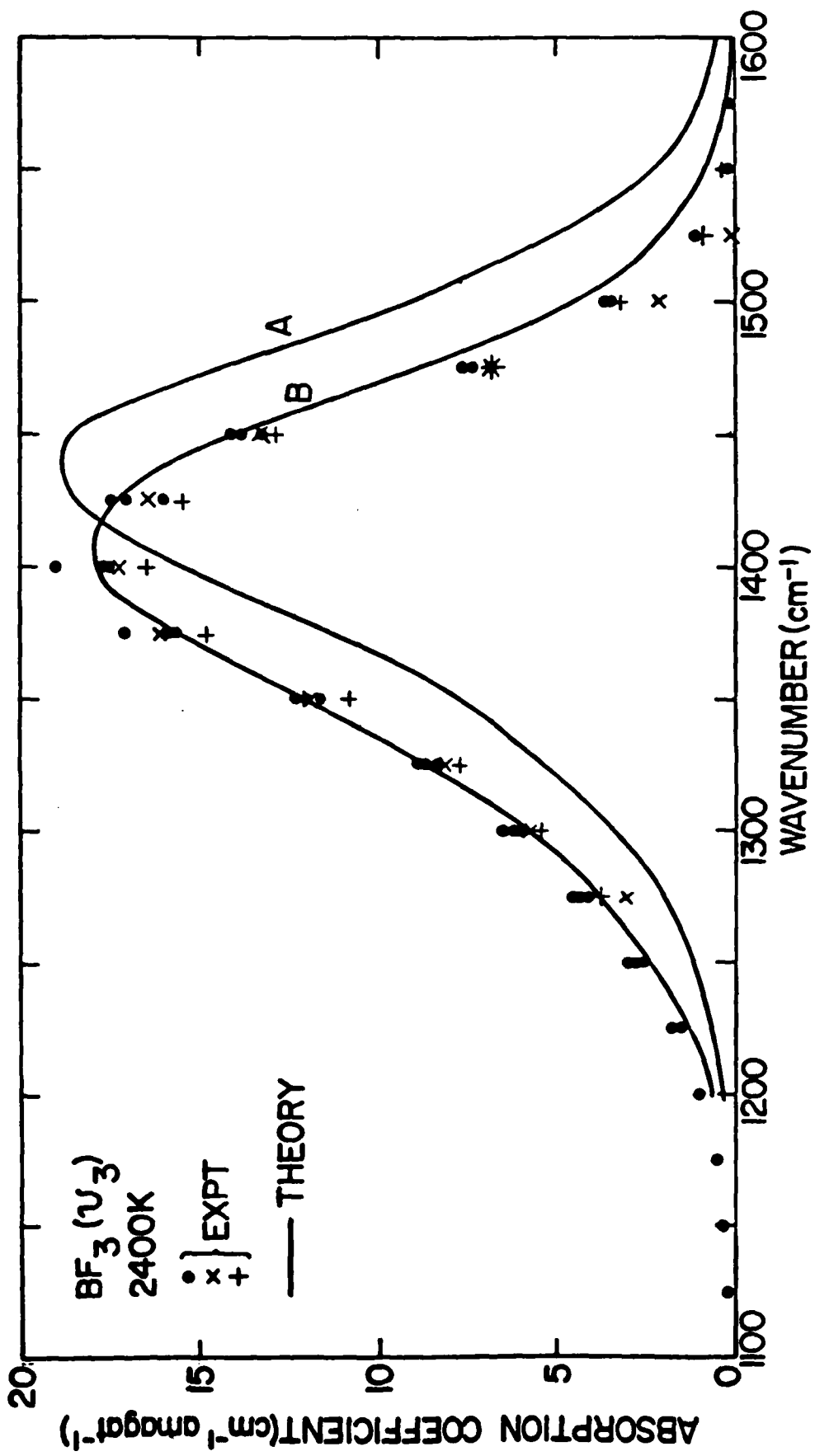


Figure 11

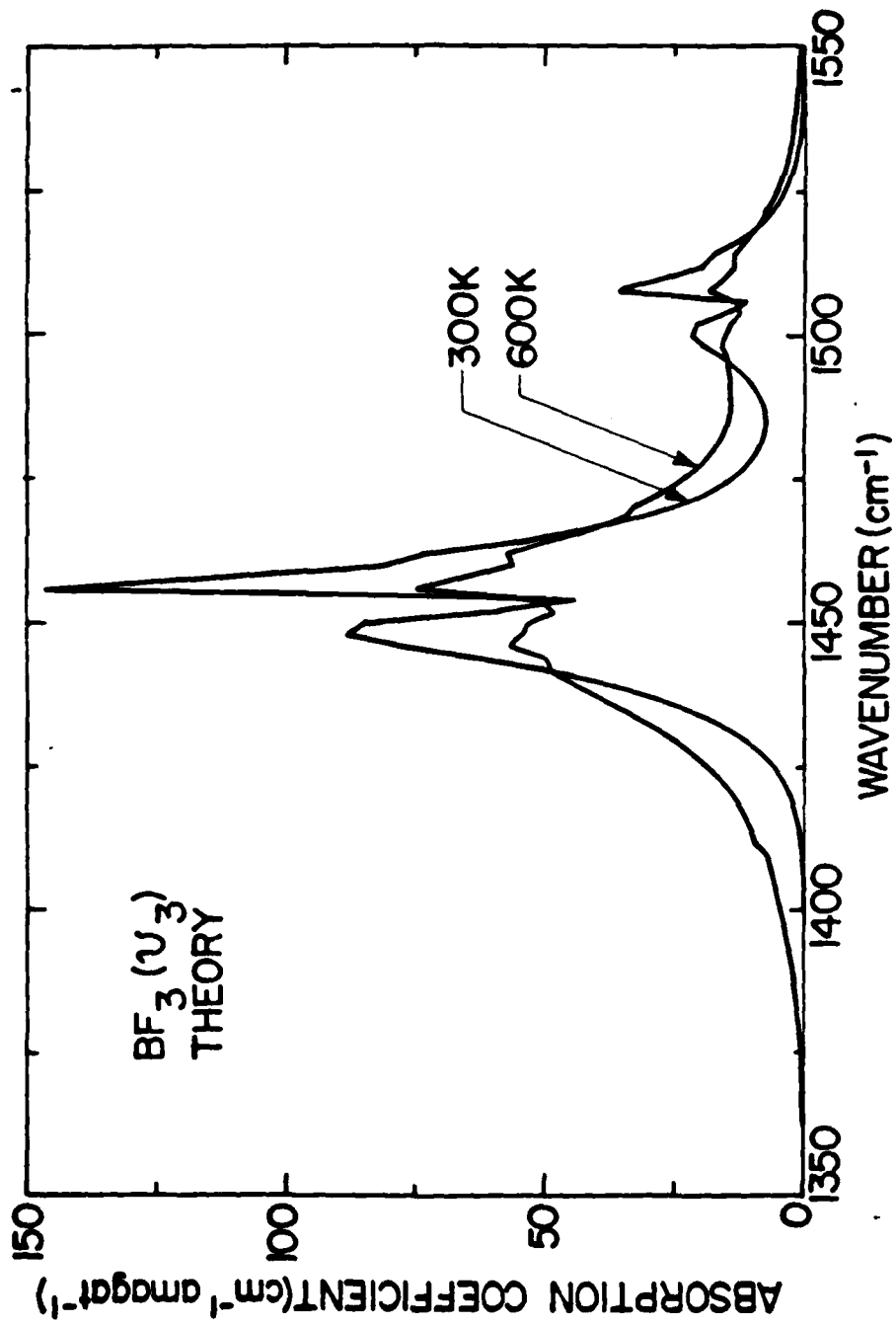


Figure 12

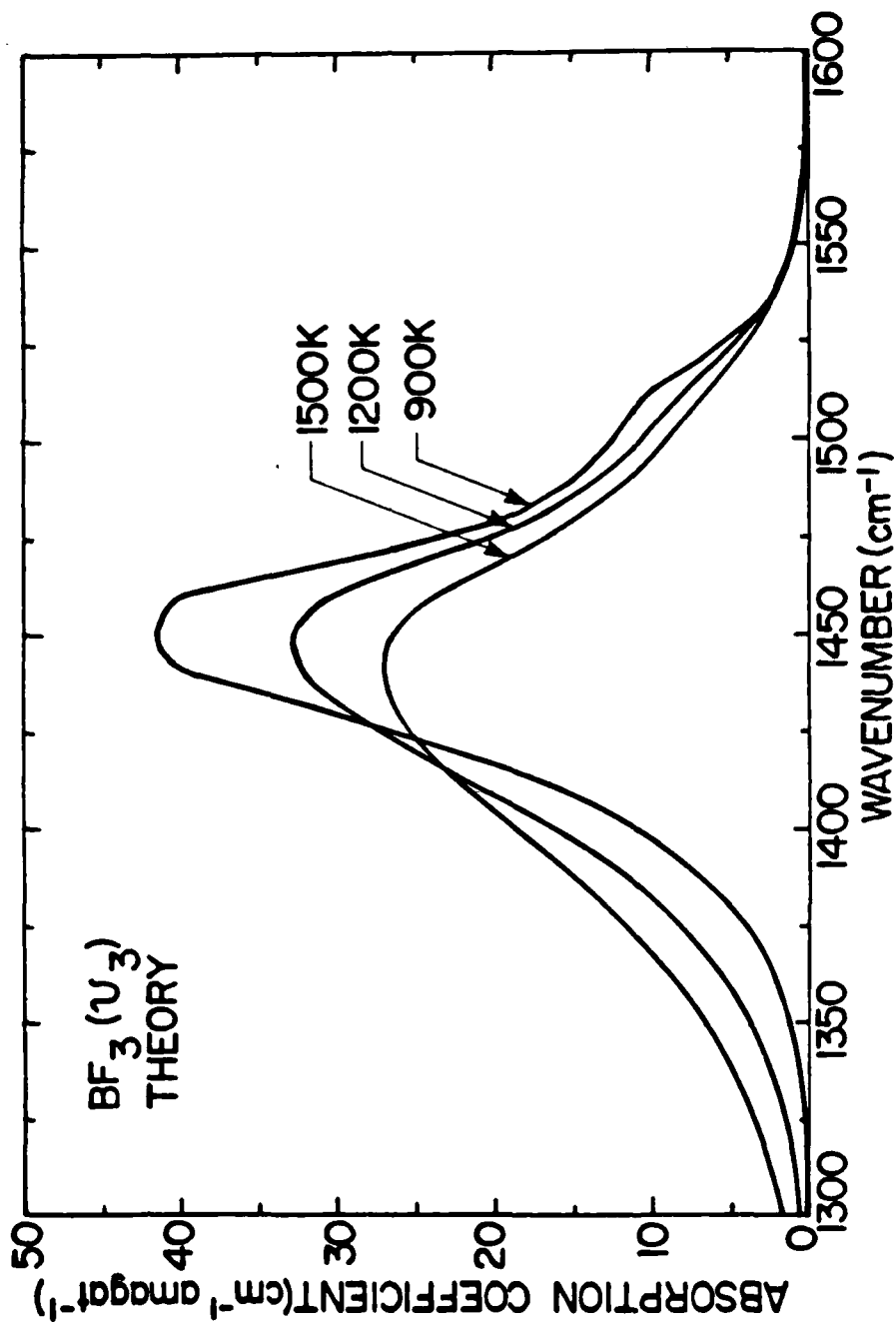


Figure 13

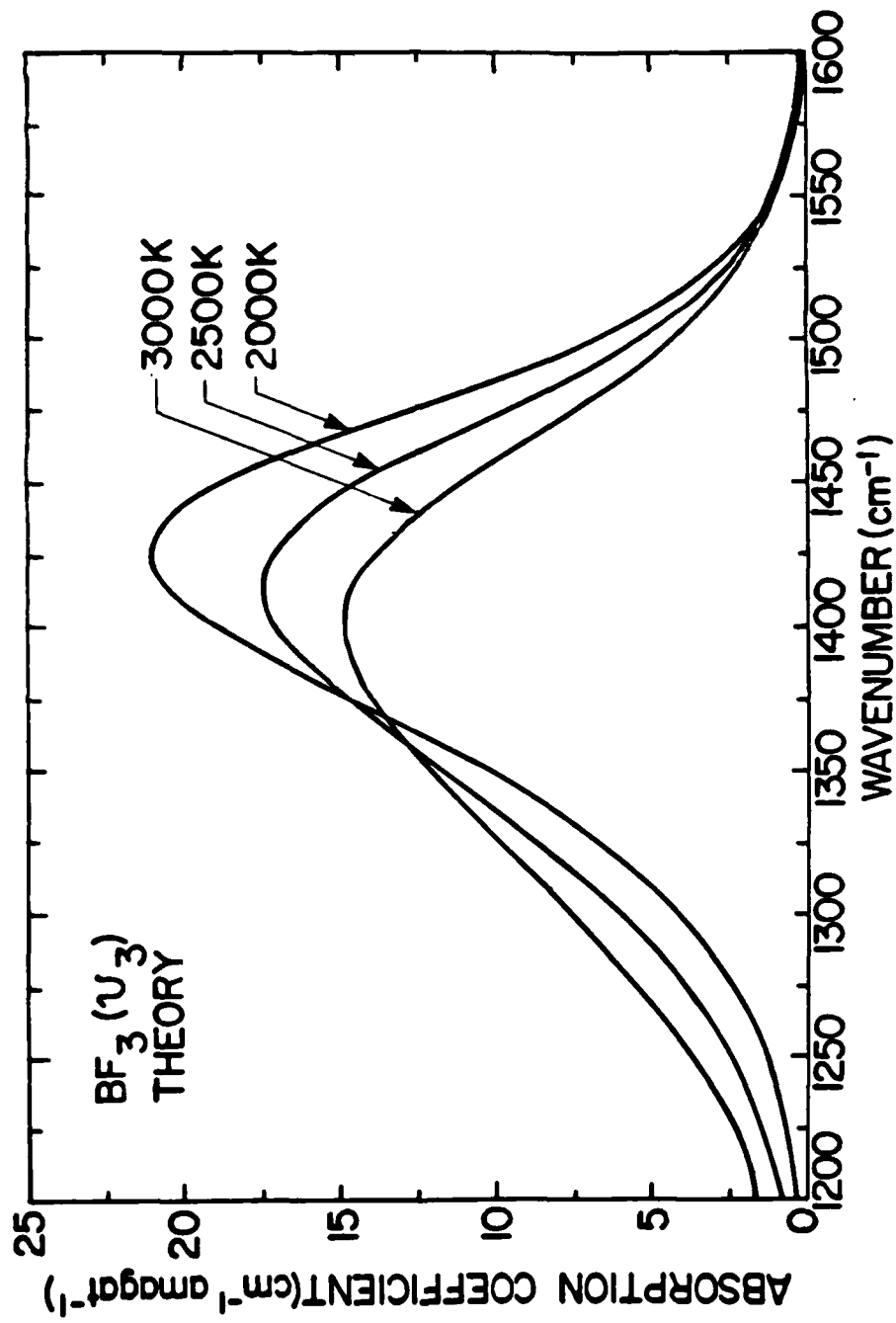


Figure 14

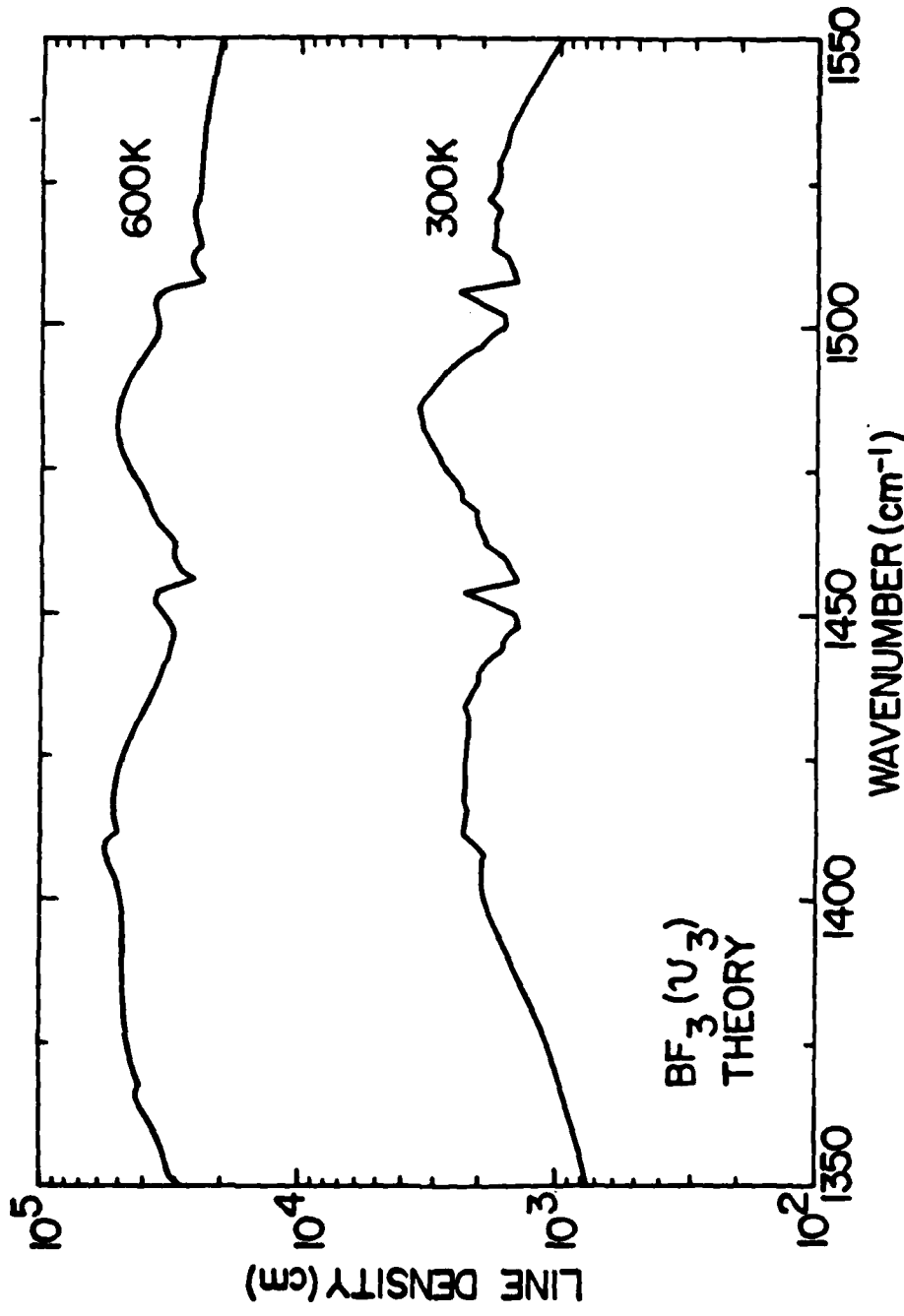


Figure 15

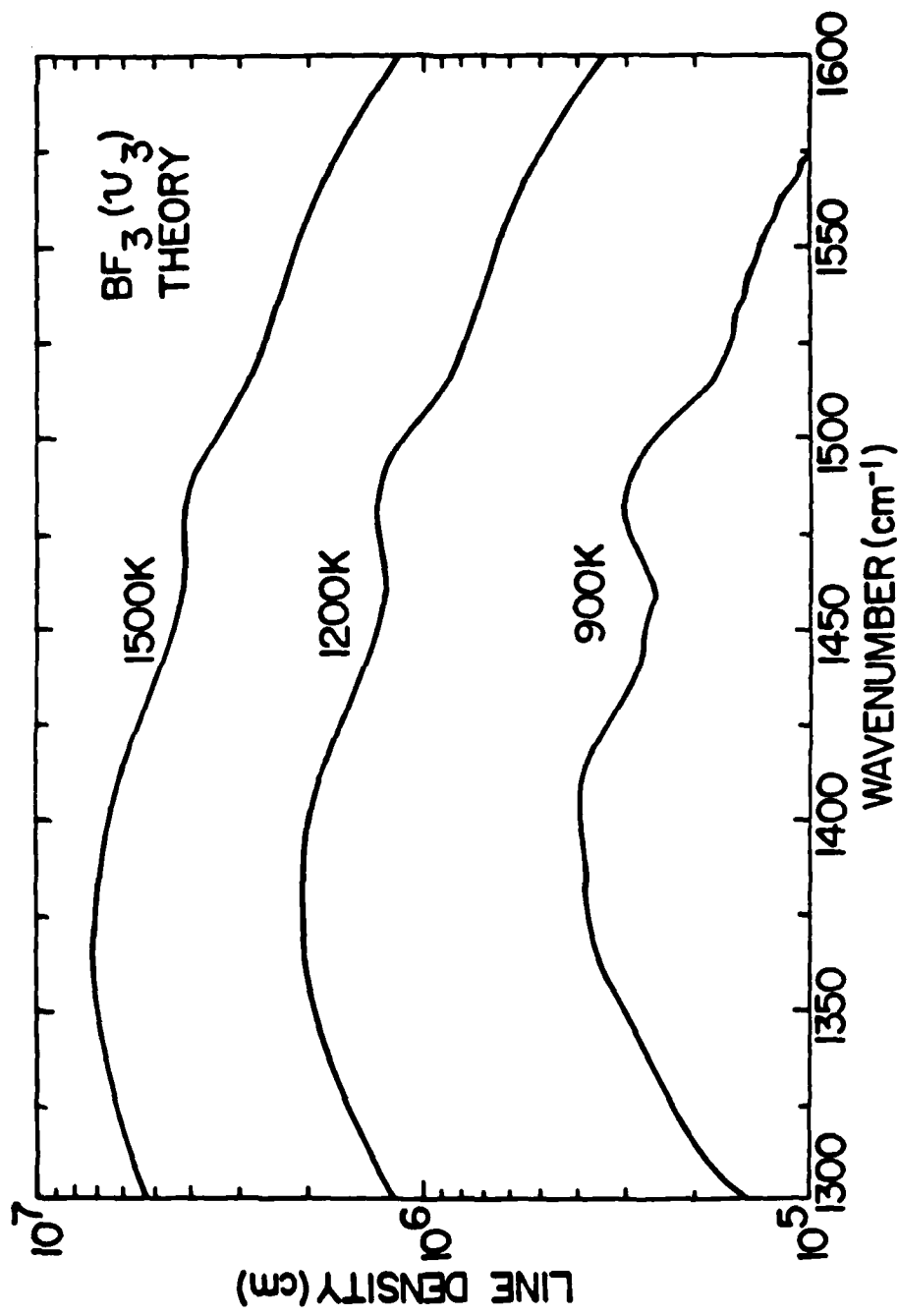


Figure 16

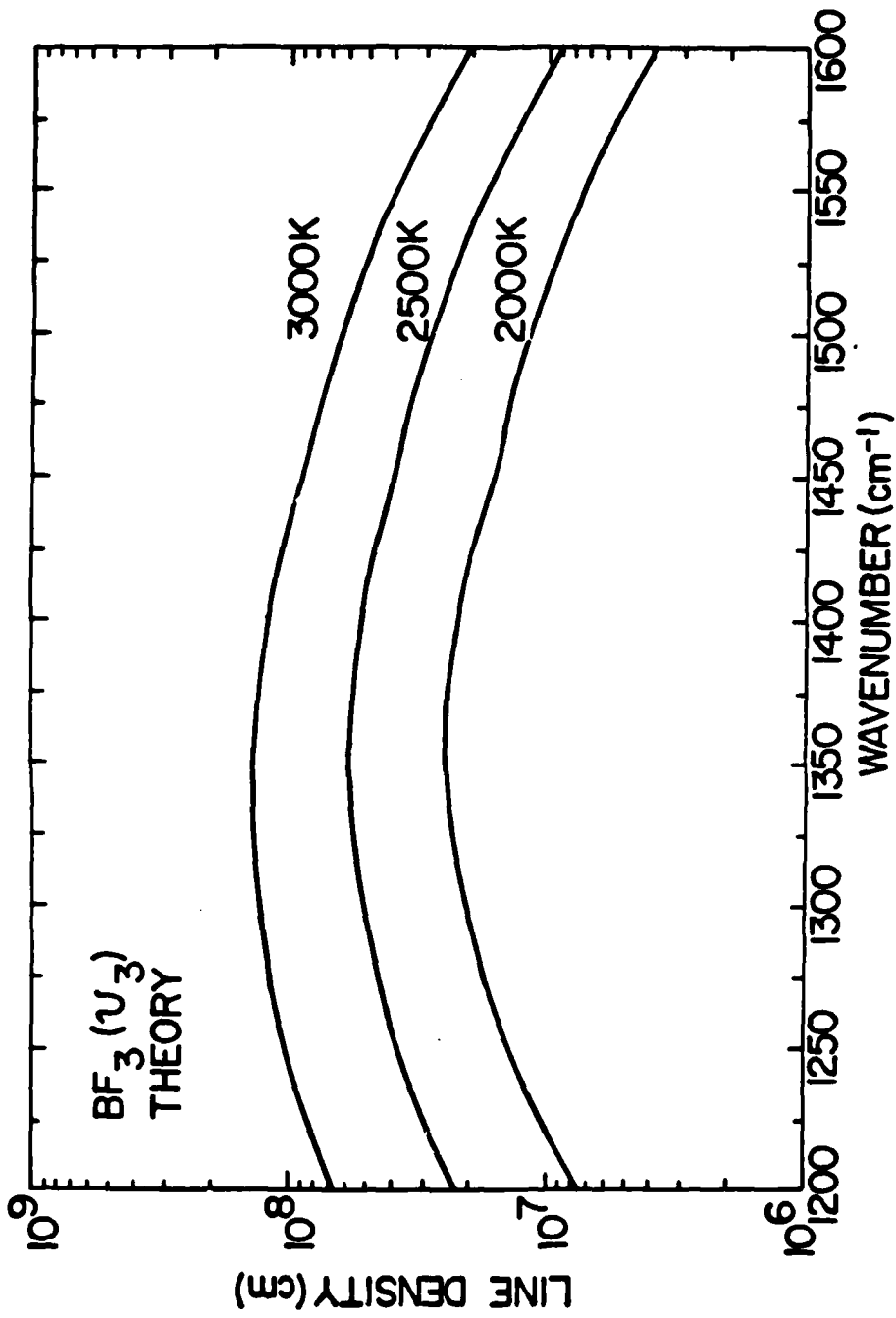


Figure 17

#### 4. MEASUREMENT OF THE VIBRATIONAL BAND STRENGTH OF $^{11}\text{BF}$ USING A TUNABLE DIODE LASER

by

Mark S. Zahniser and Michael E. Gersh

##### ABSTRACT

The infrared band strength for  $^{11}\text{BF}$  is measured by line absorption from the P(11) transition at  $1343.5\text{ cm}^{-1}$  using a tunable diode laser and multi-pass absorption cell coupled to a discharge-flow apparatus. The BF number density is simultaneously determined by ultraviolet absorption in the unresolved band head of the A  $^1\Pi + X$   $^1\Sigma$  transition at 196 nm. The resulting value for the band strength is  $650 \pm 200\text{ cm}^{-2}\text{ (STP atm)}^{-1}$  which is in good agreement with existing theoretical calculations.

## I. INTRODUCTION

The electronic spectrum of boron monofluoride has been extensively studied in the ultraviolet in both emission<sup>1,2</sup> and absorption<sup>2</sup> and its pure rotational spectrum has been observed by microwave spectroscopy.<sup>3</sup> There have been, however, no observations in the infrared of its vibrational-rotational spectrum. This is often the case for transient species due to the difficulties of producing them in sufficient quantity for detection by conventional infrared techniques.

There are even fewer IR vibrational band strength measurements, which require an independent determination of absolute concentration, for short-lived species. Such measurements, however, have been recently obtained for the C<sub>2</sub>O radical<sup>4,5</sup> and the NO<sup>+</sup> ion<sup>6</sup> using tunable diode lasers.

In this work we report the direct observation of BF using a diode laser at 7.3  $\mu\text{m}$  to measure the integrated absorption of a single vibrational-rotational line. The line strength is determined by measuring the BF concentration simultaneously by UV absorption using the band head of the A <sup>1</sup> $\Pi$   $\leftarrow$  X <sup>1</sup> $\Sigma$  (0,0) transition at 196 nm. The results of this study provide a method of monitoring BF concentrations as required for laboratory kinetic studies. They are also of interest for comparison with ab initio calculations of molecular properties of simple diatomic molecules, particularly the dipole moment derivative with respect to internuclear distances.<sup>7</sup> Finally, the measured band strength and the known spectroscopic constants may be used to produce an accurate IR radiation band model.<sup>8</sup>

## II. EXPERIMENTAL

Measurement of the IR absorption coefficient for transient species requires: (1) a stable source of the molecule, (2) a sensitive detection system, and (3) a well defined optical path which must be long enough (several meters) to provide sufficient optical depth at low concentrations and yet must be traversed by the active species in a time short enough (several milliseconds) so that the concentration remains constant over the path. Ideally, the path should not be bounded by surfaces such as windows or mirrors on which the active species may recombine and thereby create a concentration gradient along the optical path.

These requirements are met in the apparatus shown in Figs. 1 and 2 which combines a discharge flow system with a multipass absorption "White" cell<sup>9</sup> aligned so that the optical path is perpendicular to the direction of flow. The alumina flow tube is 7.3 cm id and 1 m long, but is reduced in diameter to 4 cm where it joins the detection region. At this point a concentric flow of argon is added to the main flow and adjusted so that the velocities of the two flows are equal. This results in an aerodynamic confinement of the flow tube gases in the central portion of the detection region and has the advantages of: (1) maximizing the column density of IR active species within the absorption path, (2) minimizing their traversal time across the folded path, and (3) preventing labile species from coming into contact with the White cell mirrors or other surfaces in the detection region. A more detailed description of the apparatus and of the conditions for which the flow is effectively confined is given elsewhere.<sup>10</sup>

BF is produced in a microwave discharge (2450 MHz, 100 W) of BF<sub>3</sub> (Matheson, 99.5% pure) and helium in a 1.0 cm id alumina tube which is connected to the main flow tube by a 1.4 cm id, 60 cm long, alumina tube. Maximum BF concentrations are obtained with relatively large flow rates of helium, 150 STP cm<sup>3</sup> s<sup>-1</sup>, and much smaller flow rates of BF<sub>3</sub>, 1 STP cm<sup>3</sup> s<sup>-1</sup>. BF<sub>3</sub> is observed by IR absorption at 7.3 μm and found to be less than 1% dissociated by the discharge. Argon, 100 STP cm<sup>3</sup> s<sup>-1</sup>, is added to the main flow tube to give a total pressure of 2 torr and a linear velocity of 2500 cm s<sup>-1</sup>. BF concentrations as high as 2 x 10<sup>12</sup> molecules cm<sup>-3</sup> are obtainable under these conditions. All experiments in this study are done at 300K.

#### A. UV Absorption Measurements

BF concentrations are determined by UV absorption in the unresolved band head of the A <sup>1</sup>Π + X <sup>1</sup>Σ transition at 196 nm. The light source is a high pressure xenon arc lamp (Varian Model VIX-500UV) which has a total continuum output of ~2 mW nm<sup>-1</sup> from 195 to 200 nm. The light is collimated by an internal parabolic reflector, and baffles on both ends of the absorption cell define a 0.5 cm diameter beam which passes through the center of the flow field and the IR absorption axis and is perpendicular to both. The beam is focused by a quartz lens onto the entrance slit of a 1 m monochromator (McPherson Model 2051). The grating (1200 lines/mm, 300 nm blaze) is driven by a digital stepping motor and is used in second order with 10 μm slits which give a resolution of 0.007 nm. A 200 nm interference filter with 20 nm bandpass (Acton Research) transmits less than 0.01% of the first order radiation at 400 nm. The phototube (Hamamatsu R763P) is operated in analog mode. Signal noise due to lamp intensity fluctuations is reduced by splitting the beam before it enters the absorption cell, monitoring

it with a second photomultiplier through a 200 nm interference filter, and comparing the two signals using a differential amplifier.

The fractional UV absorption is measured by turning the microwave discharge on and off while the monochromator wavelength is at a fixed position within the R-branch band head of the  $A^1\Pi + X^1\Sigma$  transition. The data analysis requires the relative monochromator transmission at each spectral line position within the band-pass, which depends on the slit function,  $G_\lambda$ , and the absolute wavelength setting of the monochromator. The slit function is determined by scanning through the Hg lines from a low pressure pen lamp (Oriel, Model 6037) at 194.1 nm in second order and 312.56 nm in first order and by calibrating the scan rate using the latter line and the adjacent 313.15 nm doublet. The spectral area under the slit is determined by integrating over the transmitted line shape with a polar planimeter which gives  $\int G_\lambda d\lambda = 0.0091 \pm 0.0002$  nm in second order. The slit function is empirically approximated in a functional form by a Gaussian core with Lorentzian tails for the purpose of calculating the relative transmission for each BF spectral line. Line positions for  $^{11}\text{BF}$  are calculated from the molecular constants given by Caton and Douglas.<sup>2</sup> Line positions for the  $^{10}\text{BF}$  isotope are shifted  $0.7 \text{ cm}^{-1}$  to the red and are calculated according to Herzberg.<sup>11</sup> The spectral slit encompasses 14 lines, R(8) through R(21), for each isotope. The band head is shaded towards the red and lies between the atmospheric absorption lines of the 3,0 Schumann Runge band of  $\text{O}_2$ . Although the monochromator is purged with  $\text{N}_2$ , there is still sufficient  $\text{O}_2$  in the optical path to provide a reference for determining the absolute monochromator setting by scanning from the R(19) and P(17)  $\text{O}_2$  lines at  $51129.49 \text{ cm}^{-1}$  and  $51121.74 \text{ cm}^{-1}$ , respectively,<sup>12</sup> through the BF band head at  $51111.26 \text{ cm}^{-1}$ . The spectrum is recorded with a strip chart recorder, and the scan is stopped at  $51110.0 \text{ cm}^{-1}$  which is slightly to the red

of the absorption maximum. The uncertainty in the resulting monochromator setting is  $\pm 0.4 \text{ cm}^{-1}$  which corresponds to an uncertainty of  $\pm 5\%$  in determining  $[\text{BF}]$  from the convolution of the slit function with the absorption lines.

The fractional absorption from a continuum source which has a constant intensity over the monochromator bandpass is

$$\frac{\Delta I}{I} = \frac{\int G_\nu \left( 1 - \exp \left[ - \sum_{I,J} N_{I,J} \sigma_o(J) e^{-\omega_{I,J}^2 \ell} \right] \right) d\nu}{\int G_\nu d\nu} \quad (1)$$

where  $N_{I,J}$  is the number density of the isotope, I, in a rotational state, J;  $\ell$  is the pathlength;  $\sigma_o(J) = 2S_J/\Delta\nu_D \sqrt{\pi/\ln 2}$  is the absorption cross section at line center,  $\nu_o$ , for the Doppler-broadened rotational line;  $\omega = 2\sqrt{\ln 2} (\nu - \nu_o)/\Delta\nu_D$  is the reduced frequency in terms of the Doppler width,  $\Delta\nu_D = 0.116 \text{ cm}^{-1}$ ; and  $G_\nu$  is the monochromator slit transmission function. The integrated absorption cross section,  $S_J$ , is calculated from the radiative lifetime,  $\tau$ , of the  $A \ ^1\Pi$  electronic state,

$$S_J = \frac{1}{8\pi c \nu_o^2} \frac{g'}{g''} \frac{1}{\tau} q_{00} \frac{d_J}{2J+1} \quad (2)$$

where  $\nu_o$  is the transition frequency in  $\text{cm}^{-1}$ ,  $g' = 2$  and  $g'' = 1$  are the electronic degeneracies of  $^1\Pi$  and  $^1\Sigma$  states, respectively,  $q_{00}$  is the Franck-Condon factor for the 0,0 vibronic band, and  $d_J = (J+2)/2$  is the Honl-London factor<sup>11</sup> for the R-branch transitions from the  $^1\Sigma$  ground state which has been normalized

so that  $\sum_{J'} S_J = 2J + 1$ , where  $J$  and  $J'$  refer to the lower and upper states, respectively. The lifetime,  $\tau = 2.8 \pm 0.3$  ns has been measured by Hesser<sup>13</sup> using the electron excitation-phase shift technique. Franck-Condon factors have been calculated by Wentink and Spindler<sup>14</sup> and by Mishra and Khanna<sup>15</sup> who obtain  $q_{00} = 0.79$  and  $0.78$ , respectively. The dependence of the electronic transition probability on the variation in the  $r$ -centroid is small enough<sup>15</sup> to be neglected in determining  $S_J$ . The fractional population in a rotational level for a given isotope is

$$\frac{N_{I,J}}{N_I} = \frac{hc}{kT} B_0 2(J+1) \exp \left[ -B_0 J(J+1) hc/kT \right] \quad (3)$$

where the rotational constant is  $B_0 = 1.507 \text{ cm}^{-1}$ .<sup>3</sup> The fractional isotopic abundances for  $^{11}\text{BF}$  and  $^{10}\text{BF}$  are  $0.802$  and  $0.198$ , respectively.<sup>16</sup>

The total BF number density is determined from a plot of fractional absorption versus  $[\text{BF}]$  obtained by numerically integrating Eq. (1). The maximum concentration used in these experiments is  $[\text{BF}] = 1.7 \times 10^{12} \text{ molecules cm}^{-3}$  which corresponds to a fractional absorption of  $7.3\%$  and a maximum optical depth at any frequency of  $\sum N_{IJ} \sigma_0 \ell \sim 0.3$  with the path length  $\ell = 4.3 \text{ cm}$ . The detection limit of  $2 \times 10^{11} \text{ molecules cm}^{-3}$  is determined by instabilities in the arc lamp which limits the minimum detectable change in  $\Delta I/I_0$  to  $-1\%$  with a signal/noise ratio of unity and a  $10 \text{ s}$  integration time constant.

## B. IR Absorption Measurements

The infrared detection system uses a Pb-salt diode laser (Laser Analytics) contained in a closed cycle helium refrigeration unit with temperature regulation. A KRS-5 lens focuses the radiation onto the entrance slit of a 0.25 m monochromator (Spex Minimate). A 150 line/mm grating with 250  $\mu\text{m}$  slits provides sufficient resolution,  $1\text{ cm}^{-1}$ , to separate laser frequency modes and gives a coarse wavelength calibration. Precise wavelength calibration is obtained by comparison with known methane absorption lines<sup>17,18</sup> from a gas reference cell placed in the beam. The beam is mechanically chopped at 800 Hz for direct absorption experiments, and brought to a focus at the plane of the front mirror of the White cell. The White cell mirrors have a 43 cm radius of curvature and are adjusted for 40 passes as a compromise between increased path length and decreased beam intensity due to reflectance losses. The number of passes is determined by counting the number of spots on the front mirror, which are formed by a helium-neon laser which is co-aligned with the IR beam.

The IR beam is focused onto a liquid nitrogen cooled, HgCdTe detector (Santa Barbara Industries) whose output signal goes to a phase sensitive amplifier referenced to the mechanical chopper. Absorption spectra are displayed using an XY recorder where the X-axis is driven by the diode current which is proportional to the laser frequency. The frequency tuning rate of  $9.1 \pm 0.3\text{ cm}^{-1}/\text{A}$  is determined by scanning through the  $\text{CH}_4$  reference lines and is independently confirmed by the fringe spacing from an accidental 86 cm etalon formed by a slight misalignment of the back mirrors of the White cell which results in multiple reflections of one edge of the expanded beam.

The particular laser mode used in these experiments has a continuous tuning range from  $1341.5 \text{ cm}^{-1}$  to  $1344.1 \text{ cm}^{-1}$ . Modes in the spectral regions on either side of this range are continuous over a much smaller range before mode hopping occurs, and therefore, the P(11) line of the fundamental band of  $^{11}\text{BF}$  at  $1343.5 \text{ cm}^{-1}$  was chosen for this study. The laser is operated at a temperature of 60K and a current of 1.3 A; conditions which often result in multimodes too closely spaced to be separated by the monochromator. The mode used in this study, however, was shown to be singular by adding enough  $\text{CH}_4$  to the absorption cell to completely attenuate the laser intensity in the region of the BF line.

Absorption measurements are made by alternately scanning the laser through the absorption line with the microwave discharge on and then off as shown in Fig. 3. The spectra are then overlaid and the difference is traced with a planimeter to obtain the integrated absorption intensity. This procedure is preferred to taking absorption measurements only at line center since it minimizes the uncertainty due to accidental etalon fringes which are superimposed on the baseline, and it eliminates the need to assume lineshape functions for both the absorber and the laser source at these optical depths. The latter is an important consideration since rather wide variability has been reported,<sup>19</sup> with laser line widths as large as  $1.4 \times 10^{-3} \text{ cm}^{-1}$ , when using closed cycle cryostats rather than liquid helium dewars for cooling. The measured temperature tuning rate of the diode in the present study is  $0.8 \text{ cm}^{-1} \text{ K}^{-1}$  which, combined with the manufacturer's specification for cryostat temperature stability of  $\pm 1 \times 10^{-3} \text{ K}$ , gives an expected line width on the order of  $10^{-3} \text{ cm}^{-1}$  compared to

the Doppler width for BF of  $3 \times 10^{-3} \text{ cm}^{-1}$ . Measurements are taken under optically thin conditions so the maximum fractional absorption in these experiments is less than 4% at line center. The laser source is sufficiently stable to detect fractional absorptions as low as  $10^{-3}$  directly with a 1s time constant, which corresponds to a detection limit for BF of  $4 \times 10^{10}$  molecules  $\text{cm}^{-3}$ . Although greater sensitivity is possible by modulating the source and using second derivative detection,<sup>20</sup> the direct absorption method is better suited for line strength determinations. The problem of a sloping baseline which is usually characteristic when frequency tuning diode lasers is minimized here by adjusting the monochromator setting so that the change in intensity due to current tuning the laser is offset by the change in the transmission function of the monochromator.

### C. Optical Path Length Determinations

Since the UV and IR absorptions are measured simultaneously on the same volume element, only the path length ratio  $\ell_{\text{IR}}/\ell_{\text{UV}}$  is needed to interpret the results. This ratio is just the integral number of passes of the IR beam in the White cell provided that both UV and IR beams are small compared to the flow dimensions and pass through the center of a uniform flowfield. To confirm these conditions the ratio is independently verified by making absorption measurements on stable gases, NO in the UV and  $\text{CH}_4$  in the IR, using the identical flow conditions and geometry as in the BF experiments. The effective path length is obtained by comparing the observed absorption for a measured mixing ratio of absorber in the carrier gas under dynamic conditions to the absorption observed with static conditions when the flow tube is isolated from the pumping system and filled with a measured partial pressure of the stable absorber. The path lengths in the static case are the directly measureable distances between the

outer windows in the UV, 56 cm, and between the White cell mirrors, 40 x 43 cm, in the IR.

The R(6)E1 line in the  $\nu_4$  fundamental of  $^{12}\text{CH}_4$  at  $1342.94 \text{ cm}^{-1}$ <sup>17,18</sup> is used for the IR measurements. The  $\ln \frac{I_0}{I}$  for intensities at line center is plotted versus  $[\text{CH}_4]$  for both the static and dynamic conditions and for fractional absorptions from 10 to 60%. The effective IR path length for the dynamic case is calculated as the ratio of the slopes of these plots times the static path length and is  $\ell_{\text{IR}} = 173 \pm 5 \text{ cm}$ , or 4.3 cm for a single pass. Although the path length determination using this ratio method does not depend on the absolute value of the  $\text{CH}_4$  line absorption coefficient, the corresponding value for the integrated line strength from this experiment, assuming a Doppler line shape, is  $S = 2.8 \times 10^{-20} \text{ cm}^{-1}/\text{molecule} \cdot \text{cm}^{-2}$ . This is in good agreement with the value of  $S = 2.7 \times 10^{-20}$  derived using the line parameters of Chedin et al.<sup>21</sup> and line absorption measurements of Restelli et al.<sup>22</sup> on other  $\nu_4$  lines, and it is within the range of  $\nu_4$  band strength measurements by several other authors.<sup>23,24</sup>

The UV path length measurement uses line absorption by the R<sub>12</sub>(10.5) and Q<sub>22</sub>(10.5) degenerate lines of the 0,0 vibronic band of the A  $^2\Sigma \leftarrow X^2\Pi$  transition in NO at  $44,135 \text{ cm}^{-1}$ <sup>25</sup> which is fully resolved by the 1 m monochromator in second order with 10  $\mu\text{m}$  slits. The path length is calculated from the fractional absorption according to the relationship

$$\frac{\Delta I}{I} = [\text{NO}] \ell \frac{N_J}{N} S_J \frac{F(N_J \sigma_o \ell)}{\int G_\nu d\nu} \quad (4)$$

where  $N_J/N$  is the fractional population in the lower rotational state and the term  $F(N_J \sigma_o \ell) = \sum_{n=0}^{\infty} (-N_J \sigma_o \ell)^n / (n+1)! \sqrt{n+1}$  accounts for the finite optical depth at line center.<sup>26</sup> The maximum optical depth in these experiments is 1.3

which corresponds to a fractional absorption of 7%. The ratio of absorption measurements under static and dynamic conditions gives a value of  $l_{UV} = 3.8 \pm 0.8$  cm where the larger uncertainty compared to the IR measurement is due to the greater uncertainty in the fractional absorption measurement. The UV path length may also be calculated directly from Eq. (4) using the integrated line absorption coefficient of  $(N_j/N)S_j = 4.0 \times 10^{-18} \text{ cm}^2 \text{ molecule}^{-1} \text{ cm}^{-1}$  obtained from the 0,0 band oscillator strength.<sup>27</sup> This results in a value of  $l_{UV} = 4.4 \pm 0.8$  cm from absorption measurements taken with the dynamic conditions only.

The combined UV and IR static versus dynamic ratio measurements give a value  $l_{IR}/l_{UV} = 45 \pm 9$  and confirm the integral path length ratio of 40, which is used in the BF data analysis, within experimental uncertainty. These measurements also confirm the effectiveness of the aerodynamic confinement of the flow tube gases to the center of the detection region and imply that there is negligible recirculation of the absorbing species in the side arms. This is further confirmed by visual observation in the detection region of an afterglow produced by passing air through the microwave discharge with the same flow conditions that were used for the BF absorption measurements. The afterglow was seen to be well confined, with no apparent recirculation.

### III. RESULTS AND DISCUSSION

The BF line frequency,  $1343.47 \pm 0.02 \text{ cm}^{-1}$ , is determined by interpolation between two sets of methane lines as shown in Fig. 3. The relative  $\text{CH}_4$  line positions are in good agreement with those of Blatherwick et al.<sup>18</sup> which have an absolute accuracy of  $\pm 0.005 \text{ cm}^{-1}$ . The line position calculated<sup>11</sup> for the  $^{11}\text{BF}$  P(11) line is  $1343.38 \text{ cm}^{-1}$  using the molecular constants obtained from the electronic spectra<sup>1,2</sup> and microwave spectra<sup>3</sup> which are tabulated by Huber and Herzberg.<sup>28</sup> The rotational constants obtained from the UV spectra by Caton and Douglas<sup>2</sup> are in excellent agreement with those obtained from the microwave spectra,<sup>3</sup> and the  $0.1 \text{ cm}^{-1}$  discrepancy between the calculated and observed line position is most probably associated with the uncertainty in the vibrational constraints,  $\omega_e$  and  $\omega_e x_e$ , which are obtained from the band origins in the UV spectra.<sup>1</sup> The observed line position corresponds to a value of  $\nu_0 = 1378.73$  for 1,0 vibrational band.

In addition to the close agreement between expected and observed line position, further evidence that the line is unambiguously due to  $^{11}\text{BF}$  is provided by the observation that no other absorption lines due to the microwave discharge are apparent in the  $2.5 \text{ cm}^{-1}$  region covered by the laser mode. The spacing between adjacent  $^{11}\text{BF}$  lines is  $2B_0 = 3.0 \text{ cm}^{-1}$  and neither the P(10) and P(12) lines could be located with this diode due to frequency gaps in the tuning range. The  $^{10}\text{BF}$  P(21) line is separated from the  $^{11}\text{BF}$  P(11) by only  $0.3 \text{ cm}^{-1}$ , but it is an order of magnitude less intense due to the higher J value and is not observed. Line positions for the 2,1 vibrational band are

also in this region and would be observed if there were a significant unrelaxed non-Boltzmann distribution of vibrational levels formed in the microwave discharge. The other possible species,  $\text{BF}_2$ , may be eliminated on line strength and line spacing arguments since the larger partition function for the triatomic species greatly decreases the intensity for a single rotational transition compared to a diatomic species with the same band strength, and more than one line would be apparent in a  $2.5 \text{ cm}^{-1}$  interval due to the larger moment of inertia. There is also thermodynamic evidence against the existence of large quantities of  $\text{BF}_2$  in this system.<sup>29</sup>

The line width in Fig. 3 is 30% greater than the Doppler width at 300 K of  $3.0 \times 10^{-3} \text{ cm}^{-1}$ . Several other effects may contribute to the linewidth including: (1) pressure (Lorentz) broadening, (2) unresolved hyperfine splitting, and (3) instrumental broadening due to the laser linewidth. Pressure broadening coefficients are typically on the order of  $0.05 - 0.1 \text{ cm}^{-1} \text{ atm}^{-1}$  (half-width at half maximum), for  $\text{N}_2$  and  $\text{O}_2$  as third bodies and are expected to be less with Ar as the collision partner as in this case. The experimental lineshape may be fitted with a Voigt profile, but this requires a broadening coefficient of  $0.2 \text{ cm}^{-1} \text{ atm}^{-1}$  which is unrealistically large for Ar. Although it is possible that the broadening coefficient for  $\text{BF}_3$  collisions could be significantly greater, the maximum  $\text{BF}_3$  concentration is  $<10^{15} \text{ molecules cm}^{-3}$  which is too low to account for this effect. The magnitude of the hyperfine interaction contribution to the linewidth may be estimated from the value for eq Q = -4.5 MHz

for  $^{11}\text{B}^{19}\text{F}$  from microwave spectra<sup>3</sup> and is negligible compared to the Doppler width. The most probable cause of the larger than Doppler linewidth is, therefore, instrumental broadening. Although we have no direct measurement of the laser linewidth, a value on the order of  $1 \times 10^{-3} \text{ cm}^{-1}$  is not unreasonable, as mentioned previously, and could account for the difference. This is further supported by observations of the  $\text{CH}_4$  line profiles which also are also larger than Doppler. It is, of course, quite possible that both Lorentz broadening and instrumental broadening contribute to the observed lineshape. However, for low optical depths and integrated absorption measurements it is not necessary to know the exact line profile to determine the line strength.

The line strength is calculated from the absorption data given in Table I using the relationship

$$S_J(^{11}\text{BF}) = \frac{\int \frac{\Delta I}{I_0} dv}{0.802 \left\{ [\text{BF}] \ell_{\text{UV}} \right\} \left[ \frac{\ell_{\text{UV}}}{\ell_{\text{IR}}} \right]} \quad (5)$$

where the integrated absorption intensity is calculated from the fractional absorption at line center times the ratio of area, A, to height, h, of the absorption profile,  $\int (\Delta I/I_0) dv \sim (\Delta I_{\text{MAX}}/I_0) A/h$ ; the product  $\left\{ [\text{BF}] \ell_{\text{UV}} \right\}$  is the total BF column density from the UV absorption measurements; the factor 0.802 is the fractional isotopic abundance of  $^{11}\text{BF}$ ; and  $\ell_{\text{UV}}/\ell_{\text{IR}} = 1/40$  is the path length ratio. The above is exact only in the limit of low optical depth. The approximations introduced by not integrating over the exact lineshapes for both laser intensity and absorption coefficient contribute no more

than 2% to the overall uncertainty in these experiments, where the maximum optical depth is 0.05 assuming a doppler lineshape and a laser linewidth of  $10^{-3} \text{ cm}^{-1}$ . The average value for five absorption measurements at each of two different BF concentrations is  $S_{P(11)} = (7.2 \pm 2) \times 10^{-19} \text{ cm}^2 \text{ molecule}^{-1} \text{ cm}^{-1}$ , at 300 K, which corresponds to a fundamental band strength of  $S_{\text{BAND}} = 650 \pm 200 \text{ cm}^{-2} (\text{STP atm})^{-1}$ . The error limits represent the overall uncertainty,  $2\sigma$ , where the major contributions are: the random errors associated with the UV absorption measurements,  $\pm 20\%$ ; the combined accuracy of the UV lifetime measurement and the Franck-Condon factors used to determine the UV absorption coefficient,  $\pm 15\%$ ; the measured, integrated IR line profile,  $\pm 10\%$ ; and the slit function convolution for the UV band head absorption,  $\pm 5\%$ .

The band strength of a diatomic molecule is directly related to the dipole moment derivative with respect to internuclear distance by

$$S = \frac{N_0 \pi}{3 c^2 m_r} \left[ \frac{d\mu}{dr} \right]^2 \quad (6)$$

where  $N_0$  is Loschmidt's number and  $m_r$  is the reduced mass. For  $d\mu/dr$  in units of Debye/ $\text{\AA}$ , and the reduced mass in amu, this gives  $S = 188 \left[ \frac{d\mu}{dr} \right]^2 / m_r \text{ cm}^{-2} (\text{STP atm})^{-1}$ . The results of several theoretical calculations of  $d\mu/dr$  are compared with the experimental value of  $4.9 \pm 0.8 \text{ Debye}/\text{\AA}$  in Table II. The recent configuration interaction calculations (CI) of Kurtz and Jordan represent the most sophisticated treatment and are in good agreement with the experimental value. The agreement is also within the experimental error for both the SCF calculations of Nesbet<sup>30</sup> and of Huo<sup>31</sup>. The semiempirical CNDO calculations

which were performed with a program supplied by the Quantum Chemistry Program Exchange<sup>32</sup> give a result which is larger than either the experimental value or the ab initio calculation; however, the agreement is reasonably good, as is typical of CNDO calculations of dipole moment derivatives.<sup>33,34</sup>

The large band strength for BF makes it feasible to use infrared absorption as a diagnostic in reaction kinetic studies. Fractional absorptions as small as  $10^{-5}$  are readily detectable with tunable diode laser sources using derivative techniques which corresponds to a detection limit of  $<10^9$  molecules  $\text{cm}^{-3}$  using the experimental configuration in this work. This sensitivity is comparable to UV resonance fluorescence<sup>35</sup> which has been previously used in BF kinetic studies,<sup>36</sup> and has the additional advantage compared to the resonance fluorescence technique of providing absolute concentration measurements without further calibration.

TABLE I. BF Absorption Data

UV (51110 $\text{cm}^{-1}$ )		IR (1343.47 $\text{cm}^{-1}$ )		
$\frac{\Delta I}{I_0}$	$[\text{BF}]^{\text{UV}}$ (molecule $\text{cm}^{-2}$ )	$\frac{\Delta I_{\text{MAX}}}{I_0}$	$\frac{A}{h}$ ( $\text{cm}^{-1}$ )	$S_{\text{P}(11)}, 300 \text{ K}$ ( $\text{cm}^2 \text{ molecule}^{-1} \text{ cm}^{-1}$ )
$0.073 \pm .01^{\text{a}}$	$7.5 \times 10^{12}$	$0.039 \pm .002^{\text{b}}$	$(4.3 \pm 0.5) \times 10^{-3}$	$7.0 \times 10^{-19}$
$0.045 \pm .01$	$4.4 \times 10^{12}$	$0.025 \pm .002$	$(4.2 \pm 0.3) \times 10^{-3}$	$7.4 \times 10^{-19}$

<sup>a</sup>Error bounds represent random fluctuations in  $I_0$  ( $2\sigma$ ).

<sup>b</sup>Standard deviation ( $2\sigma$ ) of 5 measurements.

TABLE II. Comparison of Theoretical Calculations of Dipole Moment Derivative for  $^1\text{BF}$  with Present Experimental Results

Reference	Method	$r_e$ (Å)	$d\mu/dr$ (Debye/Å)
Nesbet (1965) <sup>30</sup>	SCF	1.272	4.88
Huo (1965) <sup>31</sup>	SCF	1.245	5.56
This work	CNDO <sup>32</sup>	1.263 <sup>a</sup>	6.4
Kurtz and Jordan (1980) <sup>7</sup>	CI	1.263 <sup>a</sup>	5.21
This work	Experimental	—	4.9 ± 0.8

<sup>a</sup> Experimental value from Ref. 3.

#### ACKNOWLEDGMENTS

The authors wish to acknowledge several helpful discussions with M. Camac, F. Bien, W. Cheng, A. Stanton, F. Kaufman, J. Silver, J. Duff, L. Bernstein, and C. Kolb during the course of this work. We also wish to thank R. Brown for his dedicated assistance in developing the apparatus and performing the measurements. This work was supported by the Air Force Office of Scientific Research (AFSC) under Contract No. F49620-77-C-0075.

#### REFERENCES

1. R. Onaka, J. Chem. Phys. 27, 374 (1957).
2. R.B. Caton and A.E. Douglas, Can. J. Phys. 48, 432 (1970).
3. F.J. Lovas and D.R. Johnson, J. Chem. Phys. 55, 41 (1971).
4. J.S. Margolis, R.T. Menzies, and E.D. Hinkley, Appl. Opt. 17, 1680 (1978).
5. R.S. Rogowski, C.H. Blair, W.R. Wade, J.M. Hoell, and G.E. Copeland, Appl. Opt. 17, 1301 (1978).
6. F. Bien, J. Chem. Phys. 69, 2631 (1978).
7. H.A. Kurtz and K.D. Jordan, J. Chem. Phys., to be submitted.
8. C.B. Ludwig, W. Malkmus, J.E. Reardon, and J.A.L. Thompson, "Handbook of Infrared Radiation from Combustion Gases," NASA SP-3080, (Scientific and Technical Information Office, Washington, DC, 1973).
9. J.U. White, J. Opt. Soc. Am. 32, 285 (1942); T.H. Edwards, J. Opt. Soc. Am. 51, 98 (1961).
10. M.E. Gersh, J.A. Silver, M.S. Zahniser, C.E. Kolb, R.G. Brown, C.M. Gozewski, S. Kallelis, and J.C. Wormhoudt, "A Versatile High Temperature Flow Reactor for Kinetic and Spectroscopic Studies," Rev. Sci. Inst., submitted for publication.
11. G. Herzberg, "Molecular Spectra and Molecular Structure; I. Spectra of Diatomic Molecules, (Van Nostrand, New York 1950) pp. 141-145, 174,208.
12. M. Ackerman and F. Biaume, J. Mol. Spec. 35, 73 (1970).
13. J.E. Hesser, J. Chem. Phys. 48, 2518 (1968).
14. T. Wentink, Jr., and R.J. Spindler, Jr., J. Quant. Spectrosc. Radiat. Transfer 10, 609 (1970).
15. R.K. Mishra and B.N. Khanna, J. Quant. Spectrosc. Radiat. Transfer 10, 703 (1970).

16. R.C. Weast, ed., "Handbook of Chemistry and Physics," (Chemical Rubber Co., Cleveland, OH 1973) p. B-248.
17. R.A. McClatchey, W.S. Benedict, S.A. Clough, D.E. Burch, R.F. Calfee, K. Fox, L.S. Rothman, and J.S. Garing, "AFCRL Atmospheric Absorption Line Parameters Compilation," AFCRL-TR-73-0096 (1973); L.S. Rothman, Appl. Opt. 17, 3517 (1978).
18. R.D. Blatherwick, A. Goldman, B.L. Lutz, P.M. Silvaggio, and R.W. Boese, Appl. Opt. 18, 3798 (1979).
19. J. Reid and A.R.W. McKellar, Phys. Rev. A18, 224 (1978).
20. J. Reid, J. Shewchun, B.K. Garside and E.A. Ballik, Appl. Opt. 17, 300 (1978).
21. A. Chedin, N. Husson, N.A. Scott, and D. Gautier, J. Mol. Spectrosc. 71, 343 (1978).
22. G. Restelli, F. Cappellani and G. Melandrone, Chem. Phys. Letters 66, 454 (1979).
23. K. Fox, M.J. Reisfeld and R.S. McDowell, J. Chem. Phys. 71, 1058 (1979).
24. J.H.G. Bode and W.M.A. Smit, J. Phys. Chem. 84, 198 (1980).
25. R. Schmid, Z. Phys. 49, 428 (1928).
26. A.C.G. Mitchell and M.W. Zemansky, "Resonance Radiation and Excited Atoms," (Cambridge University Press, London, 1971) p. 324.
27. W.K. McGregor, J.D. Few, D.R. Keefer, H.S. Lowry and M.G. Davis, J. Quant. Spectrosc. Radiat. Transfer 23, 527 (1980).
28. K.P. Huber and G. Herzberg, "Molecular Spectra and Molecular Structure IV. Constants of Diatomic Molecules" (Van Nostrand, New York, 1979) pp. 86.
29. K.H. Lau and D.L. Hildenbrand, J. Chem. Phys. 72, 4928 (1980).
30. R.K. Nesbet, J. Chem. Phys. 43, 4403 (1965).
31. W.M. Huo, J. Chem. Phys. 43, 624 (1965).
32. CNDO calculations were performed using CNINDO/74: P. Dobosh and N.S. Ostlund, QCPE 11, 281 (1975).

33. G.A. Segal and M.L. Klein, J. Chem. Phys. 47, 4236 (1967).
34. R. Bruns and W.B. Person, J. Chem. Phys. 55, 5401 (1971).
35. M.B. Moeller and S.J. Silvers, Chem. Phys. Letters 19, 78 (1973).
36. G.C. Light, R.R. Herm and J.H. Matsumoto, Chem. Phys. Letters 70, 366 (1980).

### Figure Captions

1. Top view of flow tube with detail of analysis region showing confinement of optically active gases by the shield flow. Flow tube length is not to scale. White cell (A), microwave discharge cavity (B).
2. Cross sectional view of analysis region with infrared absorption and ultraviolet absorption diagnostics. Elements external to vacuum jacket not shown to scale. Vacuum jacket (A), six arm cross piece (B), white cell mirrors (C), windows (D), arc lamp (E), beam splitter (F), interference filters (G), photomultipliers (H), mirrors (I), quartz lens (J), choppers (K), monochromators (L), KRS5 lens (M), diode laser (N), HgCdTe detector (O). IR path within White cell shows maximum divergence of laser beam. The central dashed circle indicates the boundary of the optically active flow tube gases.
3. Diode laser scan through P(11) Line of  $^{11}\text{BF}$  with  $\text{CH}_4$  reference lines. Insert is expanded 10 x in intensity and shows scans with and without the microwave discharge. The dashed line is with discharge off superimposed on the trace with discharge on. BF concentration is  $1.0 \times 10^{12}$  molecules  $\text{cm}^{-3}$  and path length is 172 cm. The  $\text{CH}_4$  reference line positions from Ref. 18 are shown as arrows above the frequency scale.  $\text{CH}_4$  is added to the flow tube at the beginning of the scan, turned off at label A, and on again at label B. The lower frequency triplet are 100 x more intense than the higher frequency triplet and are completely absorbed at line center which indicates the singularity of the laser mode. The fringes in the baseline are due to the White cell mirrors which produce an etalon effect with free spectral range of  $0.0058 \text{ cm}^{-1}$ .

AL-80-537

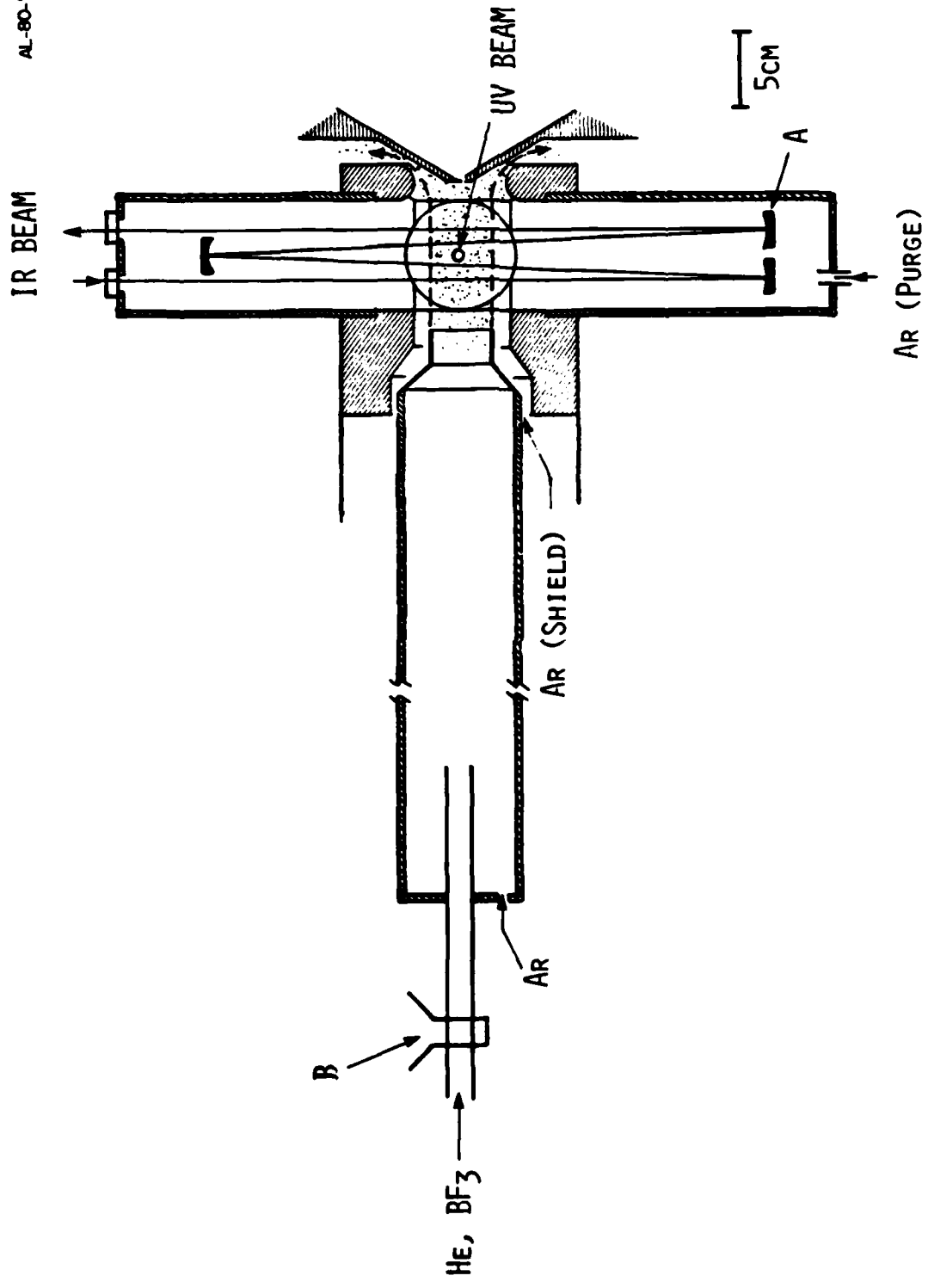


Figure 1

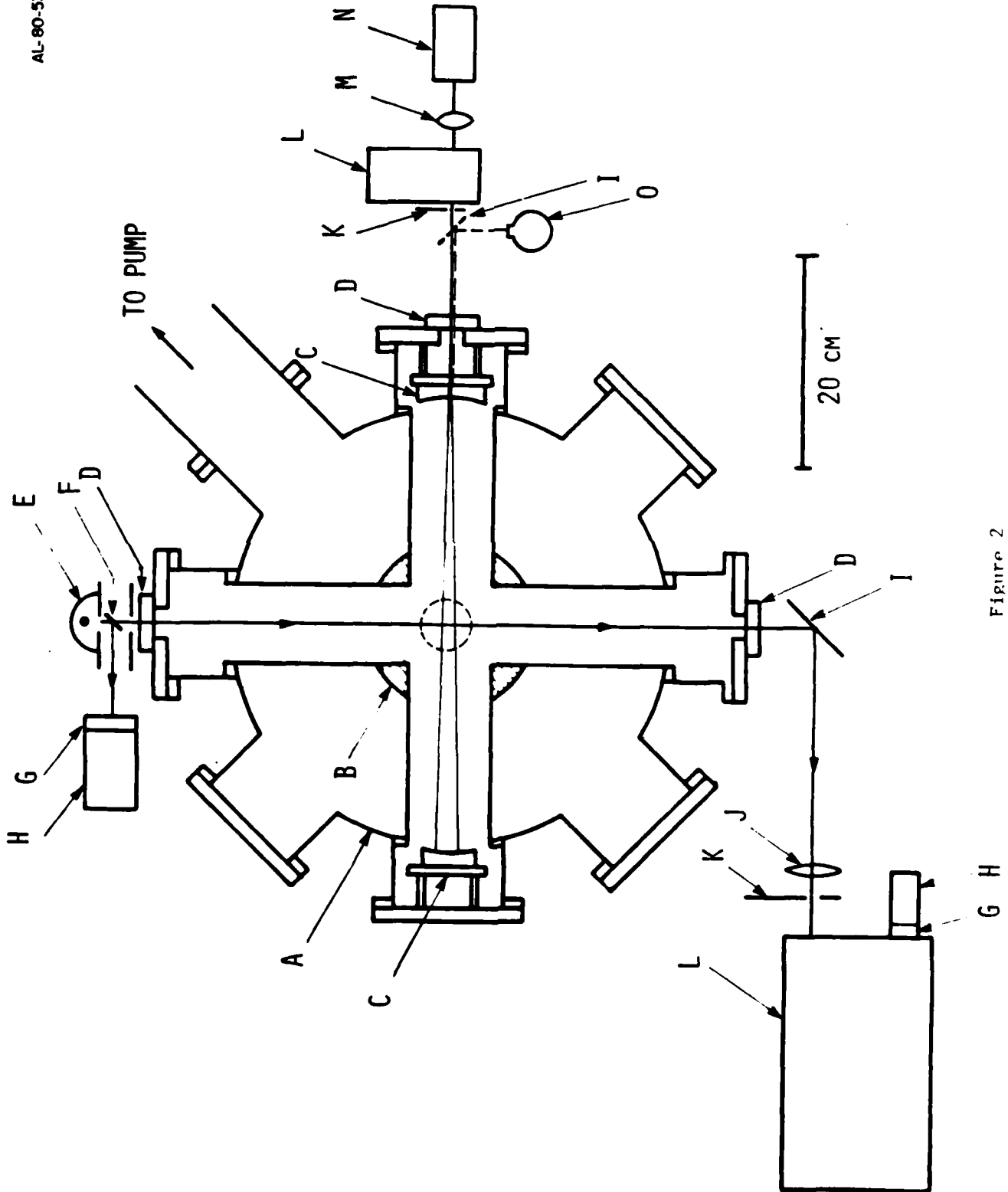


Figure 2

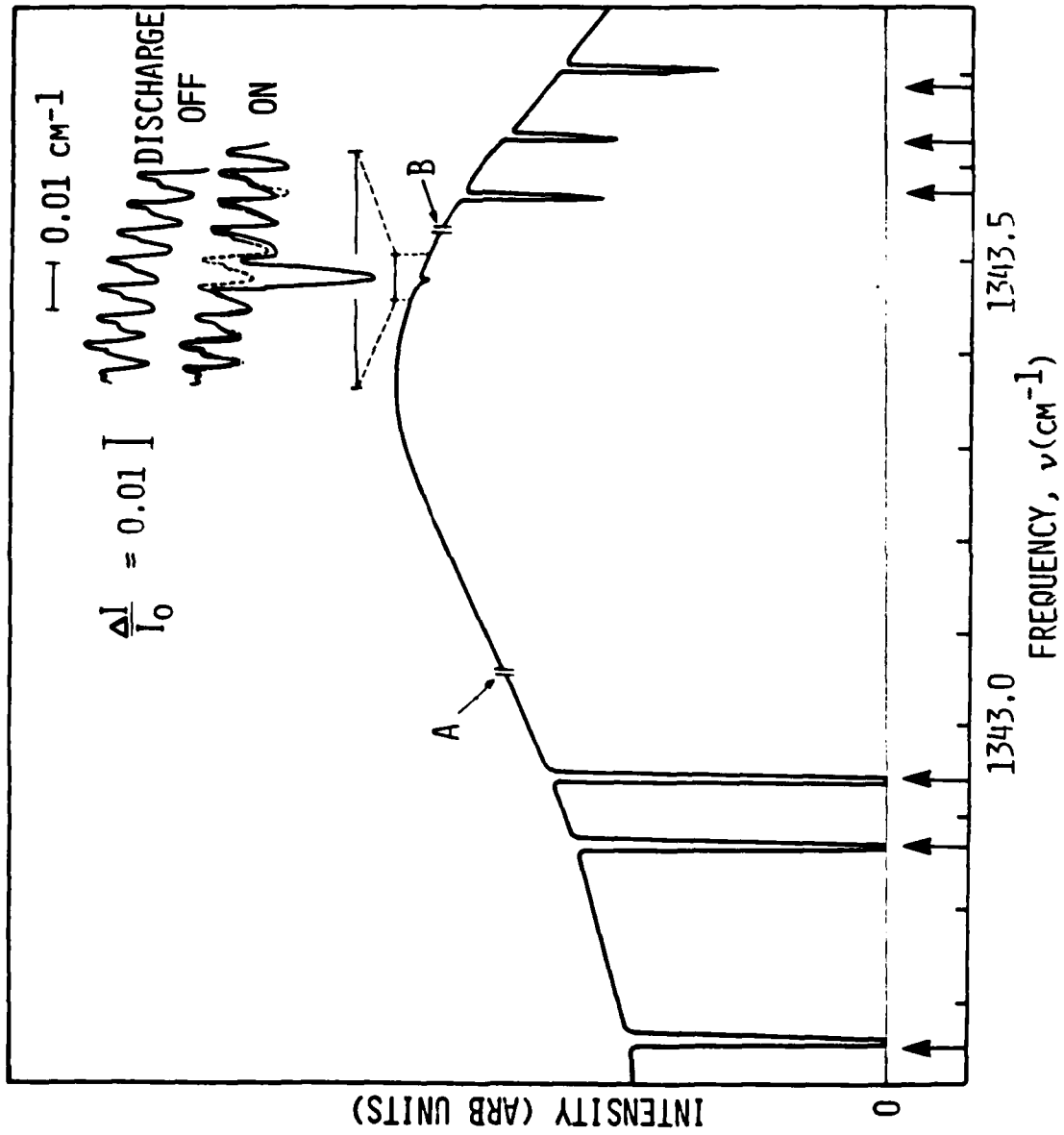


Figure 3

(This Page Intentionally Left Blank)

## 5. PUBLICATIONS AND PRESENTATIONS

### PUBLICATIONS

"Infrared Spectral Measurements of Species in a High Temperature Flow Tube," M.E. Gersh and C.E. Kolb, in PROCEEDINGS OF THE 10<sup>th</sup> MATERIALS RESEARCH SYMPOSIUM ON CHARACTERIZATION OF HIGH TEMPERATURE VAPORS AND GASES, J. Hastie, ed., National Bureau of Standards Special Publication 561 (1979), pp. 679-693.

"Measured and Predicted Band Model Parameters of  $\text{BF}_3(\nu_3)$  at High Temperatures," M.E. Gersh, L.S. Bernstein, and L.M. Peterson, submitted to J. Chem. Phys.

"A Versatile High Temperature Flow Reactor for Kinetic and Spectroscopic Studies," M.E. Gersh, J.A. Silver, M.S. Zahniser, C.E. Kolb, R.G. Brown, C.M. Gozewski, S. Kallelis, and J.C. Wormhoudt, submitted to Rev. Sci. Instr.

"Measurement of the Vibrational Band Strength of  $^{11}\text{BF}$  Using a Tunable Diode Laser," M.S. Zahniser and M.E. Gersh, submitted to J. Chem. Phys.

### PRESENTATIONS

"Design of a Flow Facility for Quantitative Spectroscopic and Kinetic Studies of High Temperature Species," M.E. Gersh and C.E. Kolb, presented at AFOSR Chemical Dynamics Meeting, Hanscom AFB, MA (October 1977).

"Infrared Spectral Measurements of Species in a High Temperature Flow Tube," M.E. Gersh and C.E. Kolb, presented at 10<sup>th</sup> Materials Research Symposium on Characterization of High Temperature Vapors and Gases, Gaithersburg, MD (September 1978).

"Infrared Spectral Measurements of Boron Oxides and Fluorides," M.E. Gersh, L.S. Bernstein, and C.E. Kolb, presented at AFOSR Molecular Dynamics Conference, Colorado Springs, CO (October 1979).